博士論文

論文題目　High-resolution spectroscopy of the allenyloxy radical and Si-bearing carbon chain radicals

（アレニロキシラジカル及び含 Si 炭素鎖ラジカルの高分解能分光）

氏　　名　梅木　博也

CONTENTS

Chapter 1
General Introduction

1.1 Free radicals

Full controls of chemical reactions are one of the most important and challenging tasks for chemists. In order to achieve them, we must understand mechanisms of the reactions completely in molecular scale. Let us consider the following reaction, for example,

$$H_2 + Br_2 \rightarrow 2HBr. \quad (1.1)$$

Although this reaction seems to be quite simple, in reality it is composed of several steps producing $Br^{\bullet}$ and $H^{\bullet}$ as reaction intermediates. Such species produced during the course of the chemical reactions are often referred to as free radicals in a broad sense.[1] Free radicals are generally reactive due to existences of unpaired electrons, and play important roles in the chemical reactions. To unravel the reaction processes, it is indispensable to detect and identify such reactive species despite their difficulties. Advances of spectroscopic techniques in the mid-20th century, however, enabled us to detect various transient species efficiently. The remarkable developments have facilitated experimental studies on radical species, and consequently structures and properties of various radicals have been clarified. Especially, developments of high-resolution spectroscopic methods, such as microwave spectroscopy and laser-induced fluorescence (LIF) spectroscopy, have made it possible to investigate energy level structures complicated by electron spin- and orbital-angular momenta of an unpaired electron. Extensive studies on free radicals associated with the developments of the experimental techniques have provided valuable information about reaction pathways in combustion and atmospheric reactions.

Free radicals have attracted attention in interstellar chemistry. More than 190 molecules have been identified in interstellar space. Although most of the interstellar molecules are neutral species, not a few of transient species such as free radicals and molecular ions have also been detected. Because of sparseness of matter and extremely low temperatures in interstellar space, the radicals and ionic species, which are generally unstable in the terrestrial atmosphere, are able to survive for long periods. According to the past researches on chemical reactions in interstellar space, the radicals are considered to contribute to neutral-neutral reactions.[2] The CN radical, for example, reacts with acetylene efficiently at low temperatures, producing a well-known interstellar molecule, cyanoacetylene:

$$CN + C_2H_2 \rightarrow HCCCN + H. \tag{1.2}$$

1.2 Oxidation products of unsaturated hydrocarbons

Intermediates of oxidation reactions of simple unsaturated hydrocarbons such as ethylene (C_2H_4), propylene (C_3H_6), and allene (C_3H_4) play important roles in combustion processes of hydrocarbon fuels. Oxides of unsaturated hydrocarbons, thus, have been received attention in combustion chemistry, atmospheric chemistry, and reaction dynamics. A large number of oxidation intermediates have been investigated by crossed molecular beam methods, and microwave and optical spectroscopic studies.

One of the simplest molecules is the vinoxy radical, CH_2CHO, which is the intermediate in the combustion process of ethylene. In 1965, CH_2CHO was first detected by absorption spectroscopy in the region from 300−350 nm ($\tilde{B}\,^2A'' \leftarrow \tilde{X}\,^2A''$).[3] About 15 years later, by crossed molecular beam experiments,[4,5] it was revealed that CH_2CHO is a major product in the reaction between O (^{3}P) and ethylene. Y. T. Lee and co-workers have estimated the relative branching ratio of the following reaction,

$$C_2H_4 + O(^3P) \rightarrow H + CH_2CHO, \tag{1.3}$$

to be about 30% by a crossed molecular beam experiment.[6] Molecular constants of this radical have been determined accurately by microwave spectroscopy, in which the molecular geometry and the electron spin distribution were discussed based on the determined molecular constants.[7,8] Furthermore, CH_2CHO have been extensively studied by various optical spectroscopic methods.[9] It is known that the electronically excited states, $\tilde{A}\,^2A''$ and $\tilde{B}\,^2A''$, lie at ~8000 and ~28750 cm^{-1} above the $\tilde{X}\,^2A''$ state, respectively.

Other molecules relevant to the vinoxy radical have been investigated by various spectroscopic methods. For example, the halogen derivatives CHClCHO[10] and CHXCFO (X = H,[11,12] F,[13] and Cl[13]), the sulfer analogue CH_2CHS[14] and its methyl derivative CH_3CHCHS,[15] and CH_3CHCHO.[16] These radicals, as well as the vinoxy radical, are of importance from the point of view of combustion chemistry. The halogen derivatives, for example, are thought to be oxidation intermediates in combustion processes of ethylene halides. Electronic spectra have been observed for all the radicals by LIF spectroscopy, clarifying that they all have the $\tilde{B}\,{}^2A'' - \tilde{X}\,{}^2A''$ band systems around 30000 cm^{-1}, as is the case for CH_2CHO. For CH_2CFO[11] and CH_2CHS,[14] pure rotational spectra have also been measured, and the planarity of the molecular geometry and the electron spin distribution were interpreted based on the determined molecular constants.

The vinoxy radical and its derivatives have been characterized by their conjugated π systems. In general, their electronic structures are described by two canonical forms: formylmethyl ($\dot{C}H_2{-}CH{=}O$) and vinoxy ($CH_2{=}CH{-}\dot{O}$) forms for CH_2CHO, for example. The contribution of each canonical structure can be determined experimentally from dipole-dipole interaction tensors of nuclei with a non-zero nuclear-spin angular momentum, because signs of the principal axis values of the tensors reflect the spatial distribution of the unpaired electron. In CH_2CHO, the experimentally determined dipole-dipole interaction tensors suggests that the contribution of the formylmethyl ($\dot{C}H_2{-}CH{=}O$) form is dominant by about 80%.[7]

Despite the importance in combustion processes of unsaturated hydrocarbons and studies of the conjugated π systems, spectroscopic studies are limited to the vinoxy radical and its halides. For a more comprehensive understanding, it is indispensable to extend the spectroscopic studies for oxides of longer unsaturated hydrocarbons such as propylene (C_3H_6) and allene (C_3H_4).

1.3 Silicon-bearing molecules in Astrochemistry

Silicon is one of the most abundant elements both on the Earth and in interstellar media. Table 1.1 shows the cosmic abundance of elements.[17] As shown in Table 1.1, silicon is the

Table 1.1. Cosmic abundance of elements.

Z	Element	Abundance ($Si = 10^6$)
1	Hydrogen	2.8×10^{10}
2	Helium	2.7×10^{9}
8	Oxygen	2.4×10^{7}
6	Carbon	1.0×10^{7}
10	Neon	3.4×10^{6}
7	Nitrogen	3.1×10^{6}
12	Magnesium	1.1×10^{6}
14	Silicon	1.0×10^{6}
26	Iron	9.0×10^{5}
16	Sulfer	5.2×10^{5}

eighth most abundant element cosmically, and plays important roles in the interstellar media. On the Earth, silicon is a highly non-volatile element and almost all silicon species are distributed in the crust as silicates. In the interstellar media also, many silicon species are considered to exist as silicates in dust grains. Several silicon-bearing molecules, however, have been detected in the gas phase, making remarkable contrast to the case on the Earth. Especially, the circumstellar envelope of the carbon-rich asymptotic giant branch (AGB) star, IRC+10216, exhibits rich gas phase chemistry of silicon. Silicon-bearing molecules identified in the interstellar media are shown in Table 1.2. A total of 11 silicon-bearing molecules including radical species, SiCN and SiNC, have been identified, and this number is not small when the fact that the total of ~190 interstellar molecules have been detected is taken into account. All the silicon-bearing molecules except SiO and SiS have been detected only in the circumstellar envelopes of carbon-rich AGB stars such as IRC+10216. SiO and SiS have been identified also in molecular clouds.[18,19,21] Owing to the richness of the silicon-bearing molecules, IRC+10216 have been subjected to theoretical studies for com-

Table 1.2. Silicon-bearing molecules identified in interstellar media.

Species	First detection year (Object)	Reference
SiO	1971 (IRC+10216, *etc*.)	18, 19, 20
SiS	1975 (IRC+10216, *etc*.)	20, 21
SiH_4	1984 (IRC+10216)[a]	22
c-SiC_2	1984 (IRC+10216)	23
SiC	1989 (IRC+10216)	24
l-SiC_4	1989 (IRC+10216)	25
SiN	1992 (IRC+10216)	26
c-SiC_3	1999 (IRC+10216)	27
l-SiCN	2000 (IRC+10216)	28
l-SiNC	2004 (IRC+10216)	29
SiH_3CN	2014 (IRC+10216)	30

[a]Infrared obvervation.

prehensive understanding of the gas phase chemistry of silicon. Here, brief descriptions of the gas phase chemistry of silicon in IRC+10216 are introduced.

Silicon chemistry in IRC+10216

AGB stars occur at the late stage of stellar evolution and thus they are sometimes called the evolved stars. The AGB phase is a brief phase (~10^6 yr) of stellar evolution. IRC+10216 is the most studied AGB star, and more than a half of interstellar molecules have been identified in this object.[31] In the late stage of stellar evolution, all hydrogen in the stellar core has been converted to helium, and the core starts to contract due to its increased density. This contraction ignites the hydrogen shell surrounding the core, and the star enters the red giant branch. Subsequently, the helium core begins to ignite, producing ^{12}C in the core. In addition, captures of alpha particles by ^{12}C produce ^{16}O. Finally, the central

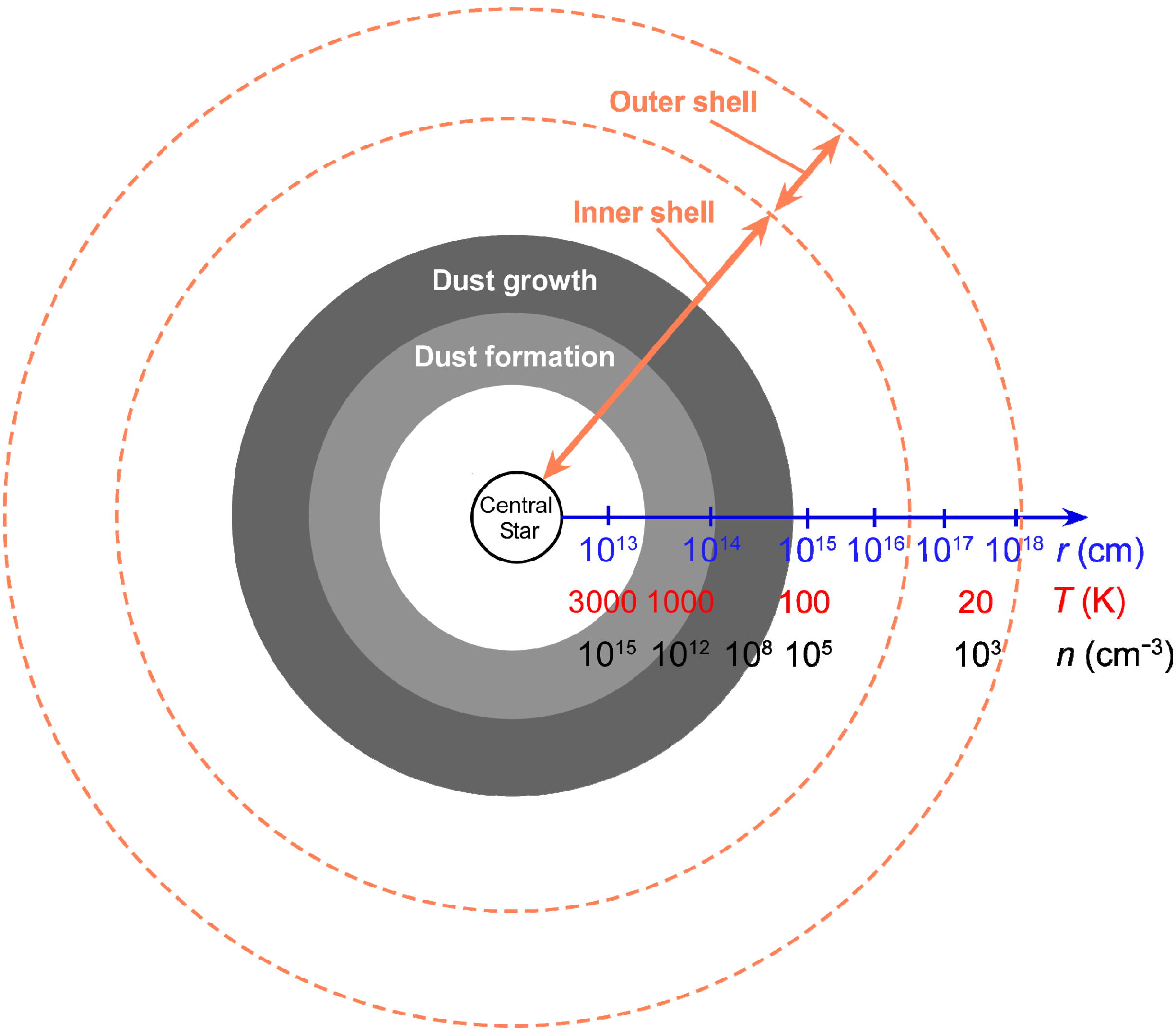

Figure 1.1. Schematic overview of the circumstellar envelop of IRC+10216. The parameters r, T, and n are the distance from the central star, the temperature of envelope materials, and the density of the materials, respectively.

helium is exhausted, leaving a carbon/oxygen shell surrounded by He-burning and H-burning shells. This is the beginning of the AGB phase. The AGB star alternates the H-burning and He-burning, and the energy released in this process brings carbon and other elements created in the He-burning shell into the stellar surface, eventually forming the chemically rich circumstellar shells. The AGB stars lose up to 80% of their original mass through the formation of the envelope. Although this object is obscure due to a plenty of dusts surrounding it, it is quite bright in radio wave and infrared observations. As shown in Fig.

1.1, the environment of the circumstellar shell varies depending on the distance from the central star, and it is roughly sorted into two regions: the inner envelope and the outer envelope. A boundary between the inner and outer envelopes is generally in the range 10^{16}–10^{17} cm. Near the central star, at ~10^{13} cm, envelope materials are hot (T ~3000 K) and dense (n ~10^{15} cm^{-3}). As they flow away from the central star, the temperature and density go down with $T \propto r^{-1}$ and $n \propto r^{-2}$, respectively. In the range 10^{13}–10^{14} cm, refractory species, such as silicon-bearing molecules and metal compounds, begin to form dust grains. It is thought that the composition of the dusts in the circumstellar shells reflects that of the gas phase.[32] Indeed, it was confirmed by infrared observations that the dust is primarily SiC in carbon-rich stars such as IRC+10216.[33] At the outer shell (10^{17}–10^{18} cm), the temperature and density of the envelope materials approach to T ~20 K and n ~10^3 cm^{-3}, respectively. All the silicon-bearing molecules presented in Table 1.2 seem to be confined in the inner envelope due to their non-volatility. However, it has been revealed that the silicon species other than SiO and SiS exist mainly in the outer envelopes.[20] Formation mechanisms of such refractory species in the cold and tenuous region has been poorly understood. Various chemical reactions have been suggested to explain the syntheses of the wide variety of gas phase silicon-bearing molecules in IRC+10216, for example, the ion-molecule reaction, the radical-molecule reaction, and the radical-radical reaction. In addition, Guélin *et al*. have pointed out that chemical reactions on dust surfaces can play an important role in the outer envelope.[34] According to the suggestion by Guélin *et al*., molecules can be synthesized on the dust grains and released in the gas phase when the grains reach the outer envelope and are exposed to interstellar UV radiation. In any case, to clarify the gas phase chemistry of silicon in this object, additional astronomical detections of the silicon-bearing molecules are highly desired. Fortunately, operations of the ALMA telescope, which covers the millimeter/sub-millimeter wavelengths range, launched last year. It is expected that more and more interstellar molecules will be detected in the near future, because the new telescope has much higher sensitivity and angular resolution than conventional ones. Now, with the advent of the "ALMA Era", more laboratory data on accurate spectroscopic constants of molecules relevant to astrochemistry, including silicon-bearing molecules, are required to support molecular identifications.

1.4 Spectroscopy of carbon chain molecules

Carbon chain molecules are the most famous interstellar molecules. Various carbon chain molecules with the forms of C_n, C_nH, C_nN, C_nS, *etc*., have been identified in a wide variety of astronomical sources. In addition to the neutral species, ion species have also been detected, C_6H^-,[35] for example. Furthermore, the carbon chains have been received much attention in connection with diffuse interstellar bands (DIBs).[36] The DIBs are absorption bands observed in the region from 400−900 nm in diffuse interstellar clouds. Although identifications of the DIBs have been attempted since their first discovery a century ago, they remain elusive. The carbon chain molecules have been considered as potential carriers of the DIBs for many years, owing to their strong electronic transtions in the visible region. Electronic spectra of the carbon chains have been observed by LIF spectroscopy, cavity ring-down spectroscopy, and resonance enhanced techniques. Their gas-phase electronic spectra derived by a number of laboratory works in the last two decades unfortunately did not show any coincidence with the DIBs data. They, however, are still attractive candidates of the DIBs, and additional laboratory detections are highly desired. From these astrochemical interests, the carbon chain molecules have been studied in laboratory by microwave/mm-wave and optical spectroscopy.

Another interest is how the properties of the carbon chains vary depending on the difference of terminal atoms. A famous example is the difference of the geometry between HC_nS and HC_nO, which are isovalent to each other. The HC_nS series are linear in their ground electronic states, while the HC_nO series are bent. Furthermore, it is well known that electronic structures change alternately with the addition of a C atom. For example, the ground electronic states of even- and odd-n C_nX (X = O, S) are $^3\Sigma^-$ and $^1\Sigma^+$, respectively. Substitution of C with Si also makes significant differences on the electronic structures. The ground electronic state of C_3N is $^2\Sigma^+$. In contrast, SiC_3H (Chapter 5) has the $^2\Pi_i$ ground electronic state, which corresponds to the low-lying $\tilde{A}\,^2\Pi_i$ state of C_4H (T_0 = 213 cm^{-1}[37]). This difference is due to unfavorable hybridization of the Si 3*s* and 3*p* orbitals in comparison to the C 2*s* and 2*p* orbitals.[38] In addition to derivatives containing non-metallic atoms, metal-terminated carbon chains MC_2H (M = Mg, Ca, Sr) have been studied. These studies have indicated the ionic binding property of the M−C bond arising from the electro-positive properties of the alkaline earth metals and the high electron affinity of C_2H.

As mentioned above, the carbon chain molecules are of importance from the point of view of astrochemistry and the studies of electronic structures, and have been considered as interesting subjects for both microwave and optical spectroscopic studies.

1.5 Outline of this thesis

With the backgrounds mentioned above, an oxidation product of allene (C_3H_4), the allenyloxy radical (CH_2=CCHO), and three silicon-bearing carbon chain radicals, SiC_2N, SiC_3N, and SiC_3H have been investigated by high-resolution spectroscopy. Experimental methods and apparatuses used in the present study are presented in Chapter 2.

Chapter 3 describes a microwave spectroscopic study of the allenyloxy radical (CH_2=CCHO). In 1993, CH_2=CCHO was first detected by a crossed molecular beam method as an intermediate in the reaction of allene (C_3H_4) with the oxygen atom (^{3}P).[39] So far, however, no spectroscopic study on this radical has been reported. In the present study, CH_2=CCHO was first detected spectroscopically. On the basis of experimentally determined molecular constants, the electronic structure and molecular geometry of CH_2=CCHO in the ground electronic state are discussed.

Chapter 4 describes laboratory observations of SiC_2N and SiC_3N by microwave spectroscopy. These two radicals have been considered as plausible candidates of interstellar molecules, owing to their large dipole moments, the high cosmic abundances of C and Si, and richness of carbon chain molecules in interstellar media such as IRC+10216. In these studies, accurate molecular constants of the two silicon-bearing molecules were determined. From the determined constants, it was revealed that SiC_2N and SiC_3N have the $^2\Pi_i$ and $^2\Pi_r$ ground electronic states, respectively. In addition, transition frequencies of these two radicals in the mm-wave region have been predicted based on the experimentally determined constants. Now, it is possible to search these radicals in interstellar media using a highly sensitive radio telescope such as ALMA.

In Chapter 5, a laser spectroscopic study of SiC_3H is presented. This radical has been received much attention in astrochemistry, as is the case for SiC_2N/SiC_3N (Chapter 4). Investigations of electronic structures of SiC_3H are also highly desired for understanding differences in properties of chemical bonding between Si and C. Very recently, this radical was first detected in laboratory by microwave and optical spectroscopy.[40] In the previous work, the $\tilde{A}\,^2\Sigma^+ - \tilde{X}\,^2\Pi_i$ band system (T_0 ~14700 cm^{-1}) was observed by resonant two-color ionization (R2PI) and low-resolution LIF spectroscopy. As mentioned before, in the case of the isovalent radical, C_4H, the $^2\Sigma^+$ state is lower in energy than the $^2\Pi_i$ state by 213 cm^{-1}. In the present study, the $\tilde{A}\,^2\Sigma^+ - \tilde{X}\,^2\Pi_i$ band system of SiC_3H was investigated by high-resolution LIF and DF spectroscopy. Rotational constants of three vibrational levels in the $\tilde{A}$ state were determined, indicating that SiC_3H is linear in the $\tilde{A}$ state. Vibrational structures in the $\tilde{X}$ state are discussed in detail based on the observed DF spectrum.

References

[1]G. Herzberg, *The Spectra and Structures of Simple Free Radicals: An Introduction to Molecular Spectroscopy* (Dover, New York, 1971).

[2]E. Herbst, Chem. Soc. Rev. **30**, 168 (2001).

[3]D. A. Ramsey, J. Chem. Phys. **43**, S18 (1965).

[4]R. J. Buss, R. J. Baseman, G. He, and Y. T. Lee, J. Photochem. **17**, 389 (1981).

[5]K. Kleinermanns and A. C. Luntz, J. Phys. Chem. **85**, 1966 (1981).

[6]A. M. Schmoltner, P. M. Chu, R. J. Brudzynski, and Y. T. Lee, J. Chem. Phys. **91**, 6926 (1989).

[7]Y. Endo, S. Saito, and E. Hirota, J. Chem. Phys. **83**, 2026 (1985).

[8]Y. Endo, and M. Nakajima, J. Mol. Spec. **301**, 15 (2014).

[9]L. R. Brock and E. A. Rohlfing, J. Chem. Phys. **106**, 10048 (1997) and references therein.

[10]S. Inomata, I. Bridier, M. Furubayashi, T. Imamura, G. Inoue, M. Yamaguchi, and N. Washida, J. Phys. Chem. A **105**, 7559 (2001).

[11]M. Furubayashi, I. Bridier, and S. Inomata, J. Chem. Phys. **106**, 6302 (1997).

[12]A. Watanabe, Y. Sumiyoshi, and Y. Endo, J. Chem. Phys. **130**, 224304 (2009).

[13]S. Inomata, M. Yamaguchi, and N. Washida, J. Chem. Phys. **116**, 6961 (2002).

[14]M. Nakajima, A. Miyoshi, Y. Sumiyoshi, and Y. Endo, J. Chem. Phys. **126**, 044307 (2007).

[15]M. Nakajima, A. Miyoshi, Y. Sumiyoshi, and Y. Endo, J. Chem. Phys. **136**, 184311 (2012).

[16]R. Kawachi, M. Nakajima, and Y. Endo, Chem. Phys. Lett. **584**, 53 (2013).

[17]E. Anders and N. Grevesse, Geochim. Cosmochim. Acta **53**, 197 (1989).

[18]R. W. Wilson, A. A. Penzias, K. B. Jefferts, M. Kutner, and P. Thaddeus, Astrophys. J. **167**, L97 (1971).

[19]L. M. Ziurys, P. Friberg, and W. M. Irvine, Astrophys. J. **343**, 201 (1989).

[20]M. Morris, W. Gilmore, P. Palmer, B. E. Turner, and B. Zuckerman, Astrophys. J. **199**, L47 (1975).

[21]L. M. Ziurys, Astrophys. J. **379**, 260 (1991).

[22]D. M. Goldhaber and A. L. Betz, Astrophys. J. **279**, L55 (1984).

[23]P. Thaddeus, S. E. Cummins, and R. A. Linke, Astrophys. J. **283**, L45 (1984).

[24]J. Cernicharo, C. A. Gottlieb, M. Guélin, P. Thaddeus, and J. M. Vrtilek, Astrophys. J. **341**, L25 (1989).

[25]M. Ohishi, N. Kaifu, K. Kawaguchi, A. Murakami, S. Saito, S. Yamamoto, S. Ishikawa, Y. Fujita, Y. Shiratori, and W. M. Irvine, Astrophys. J. **345**, L83 (1989).

[26]B. E. Turner, Astrophys. J. **388**, L35 (1992).

[27]A. J. Apponi, M. C. McCarthy, C. A. Gottlieb, and P. Thaddeus, Astrophys. J. **516**, L103 (1999).

[28]M. Guélin, S. Muller, J. Cernicharo, A. J. Apponi, M. C. McCarthy, C. A. Gottlieb, and P. Thaddeus, Astron. Astrophys. **363**, L9 (2000).

[29]M. Guélin, S. Muller, J. Cernicharo, M. C. McCarthy, and P. Thaddeus, Astron. Astrophys. **426**, L49 (2004).

[30]M. Agúndez, J. Cernicharo, and M. Guélin, Astron. Astrophys. **570**, A45 (2014).

[31]L. M. Ziurys, PNAS. **103**, 12274 (2006).

[32]S. Kwok, Nature **430**, 985 (2004).

[33]S. Kwok, K. Volk, and W. P. Bidelman, Astrophys. J. Suppl. **112**, 557 (1997).

[34]M. Guélin, R. Lucas, and J. Cernicharo, Astron. Astrophys. **280**, L19 (1993).

[35]M. C. McCarthy, C. A. Gottlieb, H. Gupta, and P. Thaddeus, Astrophys. J. **652**, L141 (2006).

[36]C. A. Rice and J. P. Maier, J. Phys. Chem. A **117**, 5559 (2013).

[37]J. Zhou, E. Garand, and D. M. Neumark, J. Chem. Phys. **127**, 154320 (2007).

[38]W. Kutzelnigg, Angew. Chem., Int. Ed. **23**, 272 (1984).

[39]A. M. Schmoltner, S. Y. Huang, R. J. Brudzynski, P. M. Chu, and Y. T. Lee, J. Chem. Phys. **99**, 1644 (1993).

[40]D. L. Kokkin, N. J. Reilly, R. C. Fortenberry, T. D. Crawford, and M. C. McCarthy, J. Chem. Phys. **141**, 044310 (2014).

Chapter 2
Experimental Method

2.1 Production of transient species

Pulsed discharge method

Various methods to efficiently produce transient species have been developed, for example, flash photolysis, pyrolysis, electric discharge, laser ablation, and laser photodissociation.[1] Our laboratory employs one of the most powerful methods, the pulsed electric discharge method. The technique has advantages in various aspects. First, it has compatibility with the supersonic jet technique. Secondly, it produces a wide variety of molecules from a single precursor. This second point, however, sometimes annoys us, because by-products contaminate a spectrum to be observed. For example, when a precursor containing the carbon atom is used, C_2 and C_3 heavily perturb optical spectra in the UV-visible energy region. However, it is still possible to pick up the spectrum of a target molecule with a help of a simulation spectrum based on molecular constants predicted by *ab initio* calculations.

In the pulsed electric discharge methods, so-called "Pulse Discharge Nozzle (PDN)" is used in our laboratory, which is composed of discharge electrodes and a commercially available solenoid valve.[2] A schematic diagram of PDN is shown in Fig. 2.1. As shown in Fig. 2.1(a), two electrodes, which are separated by a "Teflon ®" insulator, are attached at the exit of the nozzle. The solenoid valve is operated at a repetition rate of 5 or 10 Hz. Synchronized to the operation of the valve, a pulsed high voltage of 1−3 kV was applied between the two electrodes. Time durations of the discharge pulse are typically 400 and 10 μs in microwave and laser spectroscopic studies, respectively. Stainless steel or titanium is used for the material of the electrodes. The inner electrode is grounded, and a negative high voltage is applied to the outer electrode. As shown in Fig. 2.1(b), different shapes of electrodes are adopted for the outer electrode as well as their material. The production efficiency of a molecule depends on various parameters, *i.e.* applied electric voltage, the material of the electrodes, the shape of the outer electrode. It is necessary to find an optimal condition among many combinations of the parameters by cut-and-try.

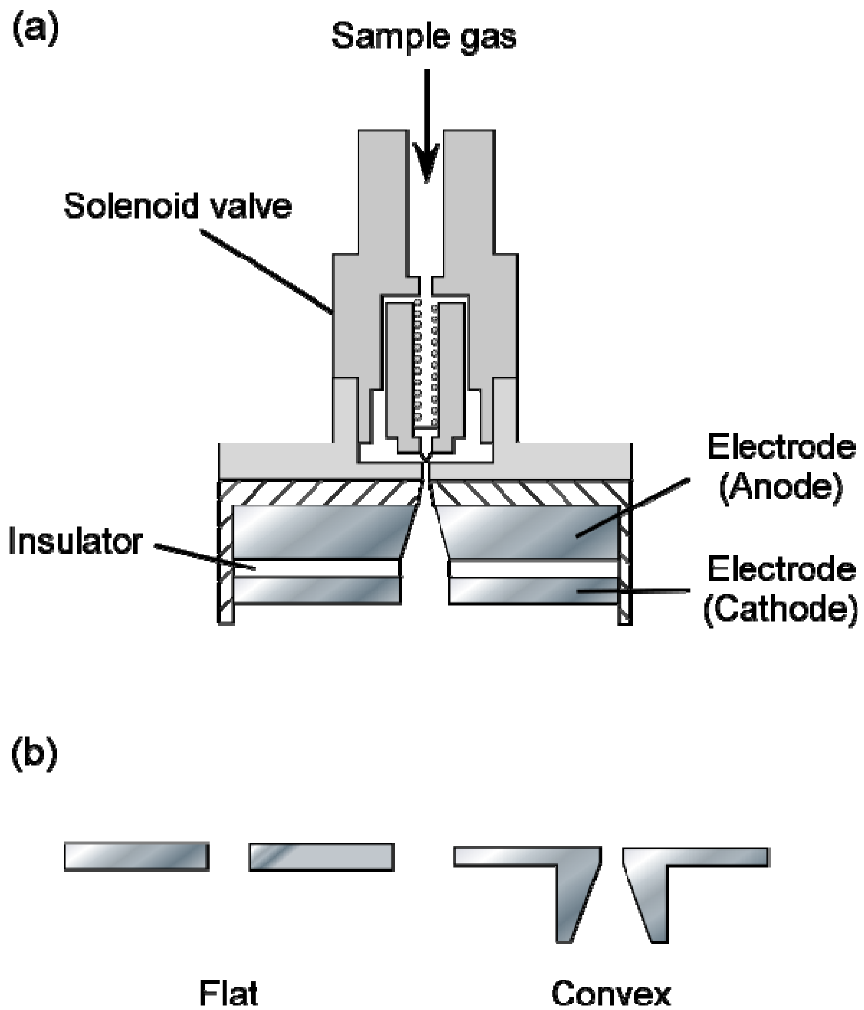

Figure 2.1. (a) Schematic diagram of a pulse discharge nozzle (PDN). (b) Two different shapes are adopted for outer electrodes (cathode) in our laboratory.

Supersonic jet technique

Complicated energy level structures originating from an unpaired electron are a major feature of an open shell radical species. A study of the complicated energy level structures requires a high-resolution spectrum of the radical. However, when a spectral measurement is made at room temperature, lines broadened due to intermolecular collisions are observed, which make a rotational analysis difficult. In addition, at room temperature, many hot bands are also observed in the spectrum, bringing into difficulty in the assignment of the observed bands. Hence, in a high-resolution spectroscopic study, we must prepare an ideal ensemble of molecules, where almost all molecules are in a particular quantum state and travel in free space without intermolecular collisions. The supersonic jet technique provides such a desirable ensemble.

In the supersonic jet technique, precursor molecules heavily diluted in an inert gas (Ne, Ar, *etc*.) are injected into a vacuum chamber through an orifice of a valve ($\phi < 1$ mm) with a high backing pressure, which is called a supersonic expansion. During the gas expansion, the translational temperature of the buffer gas goes down to extremely low via two-body collisions. The precursor molecules collide with the extremely cold rare gas atoms during the expansion. As a result, most parts of the vibrational and rotational energies of the molecules are transferred to the translational energies of the rare gas atoms. In general, the rate of equilibration between the translation and the rotation is faster than that between the translation and the vibration. The rotational temperature is, thus, cooled more efficiently than the vibrational temperature. Once the translational temperature goes down to a few K, further intermolecular collisions scarcely take place and the internal energies of the molecules remain preserved. Therefore, even reactive transient species can survive for a long periods in the jet.

Quantitative descriptions of the supersonic jet technique are as follows.[3,4] Let us introduce a parameter, M. This parameter is called the "Mach number" and defined as a ratio of a mass flow velocity u and the speed of sound a at a given beam temperature T,

$$M = \frac{u}{a} = \frac{u}{(\gamma RT)^{1/2}}, \tag{2.1}$$

where γ is the ratio of the heat capacities (C_p/C_v), and R is the gas constant. The beam temperature T is related to the Mach number M and γ as

$$\frac{T}{T_0} = \left(\frac{P}{P_0}\right)^{(\gamma-1)/\gamma} = \left(\frac{\rho}{\rho_0}\right)^{\gamma-1} = \frac{1}{1+\frac{1}{2}(\gamma-1)M^2}, \tag{2.2}$$

where P and ρ are the pressure and the density of the gas, respectively, the subscript "0" is used for those of the gas in a reservoir. Equation (2.2) indicates that the beam temperature falls down with an increase of M. The Mach number M is written as a function of the distance from the nozzle, X,

$$M = A\left(\frac{X}{D}\right)^{\gamma-1}, \tag{2.3}$$

where A is a quantity which depends on γ, and D is a nozzle diameter. Note that Eq. (2.3) is based on an assumption that the gas is continuous, whereas in reality it is composed of discrete particles. The total number of collisions is finite and thus M reaches a terminal Mach number M_T. The terminal Mach number M_T is expressed in terms of the collisional effectiveness constant ε and the mean free path of the gas, λ_0,

$$M_T = 2.05\varepsilon^{-(1-\gamma)/\gamma}\left(\frac{\lambda_0}{D}\right)^{(1-\gamma)/\gamma}. \tag{2.4}$$

In addition, it is empirically known that when Ar is used as a buffer gas, M_T is estimated from P_0 and D according to the following relation,

$$M_T = 133(P_0 D)^{0.4}, \tag{2.5}$$

where the units for P_0 and D are atmosphere and centimeter, respectively. For example, T_0 = 300 K, P_0 = 1 atm, and D = 1 mm give the terminal Mach number M_T of 53 and the beam temperature T of 0.3 K. If one wishes to make an ensemble of molecules as cold as possible, a higher backing pressure and a larger nozzle orifice should be utilized. According to the report by Smalley *et al.*,[5] when a 2−5% mixture of NO_2 in Ar was used at T_0 = 300 K, P_0 = 0.7−1 atm, and D = 0.72 mm, the translational and rotational temperatures of NO_2 were cooled to 2 and 3 K, respectively. In contrast, the vibrational temperature remained at the room temperature under the experimental conditions.

2.2 Fourier transform microwave spectroscopy

Fourier transform microwave (FTMW) spectroscopy is one of the most sophisticated method to observe rotational spectra of short-lived species. In the micorowave spectroscopic study, rotational transitions of molecules are observed, and molecular constants such as the rotational constants and the hyperfine coupling constants are determined by analyses of the observed spectra. In 1976, FTMW spectroscopy was first proposed by Ekkers and Flygare at University of Illinois.[6] In their initial system, molecules enclosed in a waveguide is irradiated with a traveling wave pulsed microwave, by which the molecules are polarized coherently. After the microwave pulse, free induction decay (FID) signals emitted from the polarized molecules are detected. The performance of the instrument was demonstrated by observing a rotational spectrum of formaldehyde, and it successfully provided a spectrum with high signal-to-noise ratio and resolution. However, there was a disadvantage that it required high power for the microwave pulse to efficiently polarize molecules. For example, when the instrument was applied to a molecule with a permanent dipole moment of 1 D, it was necessary to obtain a pulse power of 10 W using a traveling wave tube (TWT) amplifier. Therefore, it was applicable only to molecules with relatively large dipole moments.

Balle and Flygare had improved the spectrometer for the next couple of years, and a new type of pulsed microwave spectrometer was released in 1981, which is so-called the "Balle-Flygare type" FTMW spectrometer and is used in our laboratory.[7] Balle and Flygare replaced the traveling wave pulse with the standing wave pulse in a high-Q Fabry-Perot cavity. Hence, it became unnecessary to use high-power microwave pulses utilizing the TWT amplifier. Furturemore, they combined the system with the supersonic jet technique, which made it possible to detect transient species. A frequency coverage obtained by a single microwave pulse, however, is inferior to the original instrument invented in 1976. A bandwidth of the Fabry-Perot cavity is 1 MHz at 10 GHz, whereas a 50 MHz bandwidth is covered by a single pulse in the original Ekkers and Flygare type FTMW spectrometer.

Free induction decay (FID)

The most important part of the operation of the FTMW spectrometer is a coherent interaction between molecules and the pulsed microwave. Consider an ideal two-level system as shown in Fig. 2.2. A time-dependent Schrödinger equation for a fictious atom with a two-level system is written as

$$i\hbar\frac{\partial}{\partial t}\psi_n(\mathbf{r},t)=\mathbf{H}\psi_n(\mathbf{r},t), \qquad (n = 1,2). \tag{2.6}$$

In the absence of a perturbation term $\mathbf{H}_1$, time-dependent solutions of Eq. (2.6) are

$$\psi_n(\mathbf{r},t)=\phi_n(\mathbf{r})\exp(-i\,E_n t/\hbar), \qquad (n = 1,2). \tag{2.7}$$

The interaction of the oscillating electromagnetic field and the fictious atom is taken into account by an addition of a time-dependent perturbation term as

$$\mathbf{H}_1(t)=-\boldsymbol{\mu}\cdot\mathbf{E}(t). \tag{2.8}$$

The wave function for the perturbed two-level system is given by a linear combination of ψ_1 and ψ_2,

$$\Psi=a_1(t)\psi_1(\mathbf{r},t)+a_2(t)\psi_2(\mathbf{r},t), \tag{2.9}$$

where a_1 and a_2 are time-dependent coefficients. If the electric field oscillates at an angular frequency ω with its amplitude uniform in the system, then

$$|\mathbf{E}|=|\varepsilon|\cos(\omega t+\theta)=\frac{1}{2}\left\{\varepsilon\exp(i\omega t)+\varepsilon^*\exp(-i\omega t)\right\}. \tag{2.10}$$

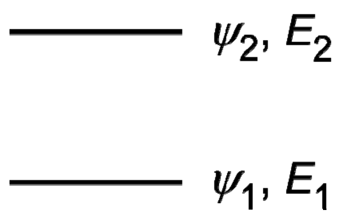

Figure 2.2. Two-level system.

Substituting Eq. (2.9) and $\mathbf{H} = \mathbf{H}_0 + \mathbf{H}_1$ into Eq. (2.6) yields

$$i\hbar\left(\frac{da_1}{dt}\psi_1 + a_1\frac{d\psi_1}{dt} + \frac{da_2}{dt}\psi_2 + a_2\frac{d\psi_2}{dt}\right) = (\mathbf{H}_0 + \mathbf{H}_1)(a_1\psi_1 + a_2\psi_2). \tag{2.11}$$

Applying the rotating wave approximation after some algebraic manipulation gives the following second-order differential equation,

$$\frac{d^2}{d^2t}a_2(t) + i(\omega - \omega_0)\frac{d}{dt}a_2(t) + \frac{(\mu_{12}\varepsilon)^2}{4\hbar^2}a_2(t) = 0, \tag{2.12}$$

where $\omega_0 = (W_2 - W_1)/\hbar$, $\mu_{12} = \langle\phi_1(r)|\mu_z|\phi_2(r)\rangle = \mu_{21}{}^*$. A general solution to Eq. (2.12) is given by,

$$a_2(t) = \exp\left[-\frac{i(\omega-\omega_0)}{2}t\right]\left\{C_1\exp\left(\frac{i\Omega}{2}t\right) + C_2\exp\left(-\frac{i\Omega}{2}t\right)\right\}, \tag{2.13}$$

where $\Omega = \sqrt{(\omega-\omega_0)^2 + (\mu_{12}\varepsilon/\hbar)^2}$, C_1 and C_2 are unknown constants. Setting the initial conditions as $a_1(0) = 1$ and $a_2(0) = 0$,

$$a_2(t) = \frac{i\mu_{12}\varepsilon}{\Omega\hbar}\exp\left[-\frac{i(\omega-\omega_0)}{2}t\right]\sin\frac{\Omega}{2}t. \tag{2.14}$$

Consequently, the time-dependent probability that the system is found in the excited state is given by

$$|a_2(t)|^2 = \left|\frac{\mu_{12}\varepsilon}{\Omega\hbar}\right|^2\sin^2\frac{\Omega}{2}t. \tag{2.15}$$

The probability $|a_2(t)|^2$ is plotted in Fig. 2.3. As seen in Fig. 2.3, the system alternates absorptions and emissions with a cycle of $\hbar\pi/|\mu_{12}\varepsilon|$. The coherent cycling is in reality dumped out by collisions with other atoms. The frequency Ω is called the nutation frequency. Especially, when $\omega = \omega_0$, $\Omega = |\mu_{12}\varepsilon|/\hbar$, which is so-called Rabi frequency.

The coherent interaction induces a oscillating electric dipole moment for the atomic system expressed as

$$\begin{aligned}\langle p(t)\rangle &= \langle\Psi(r,t)|\mu_z|\Psi(r,t)\rangle \\ &= a_1(t)a_2^*(t)\mu_{21}\exp(i\omega_0 t) + a_1^*(t)a_2(t)\mu_{12}\exp(-i\omega_0 t) \\ &= \frac{i\mu_{12}\varepsilon}{2\Omega\hbar}\mu_{21}\left\{\sin\Omega t - i\frac{\omega-\omega_0}{\Omega}(1-\cos\Omega t)\right\}\exp(i\omega t) + c.c.. \end{aligned} \tag{2.16}$$

If the coherent interaction terminates at $t = t_1$, then

$$\langle p(t)\rangle = a_1(t_1)a_2^*(t_1)\mu_{21}\exp(i\omega_0 t) + a_1^*(t_1)a_2(t_1)\mu_{12}\exp(-i\omega_0 t). \qquad (2.17)$$

Now, $a_1(t_1)$, $a_2(t_1)$, and their complex conjugates are constants, and $\langle p(t)\rangle$ oscillates at the resonance frequency, ω_0. Electromagnetic radiations induced by the oscillating electric dipole moment are called the free induction decay (FID) signals. It is readily understood that $|a_1(t_1)| = |a_2^*(t_1)|$ gives the maximum signal intensity, since the intensity is proportional to $a_1(t_1)a_2^*(t_1)$. Figure 2.3 indicates that if the following relation,

$$\Delta t = \frac{\hbar\pi}{2|\mu_{12}\varepsilon|},$$

or

$$\frac{|\mu_{12}\varepsilon|}{\hbar}\Delta t = \frac{\pi}{2}, \qquad (2.18)$$

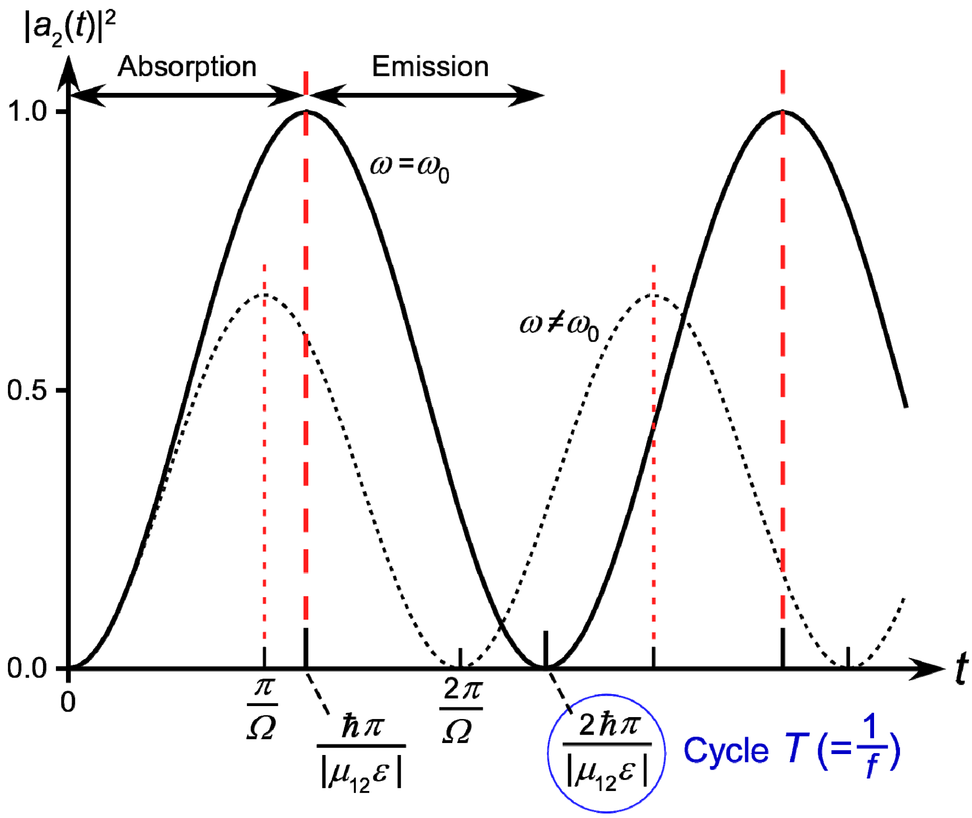

Figure 2.3. Probabilities that the system is found in the excited state for two detuning frequencies, $\omega = \omega_0$ and $\omega \neq \omega_0$.

is satisfied, $|a_1(t_1)| = |a_2^*(t_1)|$. In other words, a pulsed microwave with the time duration expressed in Eq. (2.18), so-called $\pi/2$ pulse, yields the maximum intensity of the FID signal. Note that in addition to the time duration Δt, two parameters, μ_{12} and ε, appear in Eq. (2.18), where μ_{12} and ε are a dipole moment and an electromagnetic field intensity, respectively. Therefore, we must optimize the pulse duration and its power for each molecule to be observed.

Apparatus

An observable frequency range in our FTMW spectrometer is 4−40 GHz. Equipments such as microwave components and switches for the frequency region are not so expensive and readily available. Furthermore, in the frequency region, it is possible to observe rotational spectra of molecules with their rotational constants of a few of or several tens of GHz, corresponding to *n*-atomic molecules with $n \geq 3$. Figure 2.4 shows a block diagram of the FTMW spectrometer. An output of the synthesizers (ROHDE&SCHWARZ SMR-40 for 0−40 GHz or Anritsu MG3692C for 0−20 GHz) is used as a microwave source. The microwave output is shaped to a pulsed microwave with < 1 μs duration by a microwave switch. The pulsed microwave is introduced into a Fabry-Perot cavity, set inside a vacuum chamber, using an L-shaped monopole antenna. The vacuum chamber is evacuated by a 18-inch oil diffusion pump (DAIVAC LIMITED DPF-18Z, 9000 *l*/s) connected to a mechanical booster pump (ULVAC PMB-006CM, 139 *l*/s) and an oil rotary pump (EDWARDS E2M80, 21 *l*/s) as mechanical forepumps. The Fabry-Perot cavity is depicted in Fig. 2.5. The cavity is composed of two aluminum spherical mirrors with a diameter of 300 mm and a curvature radius of 600 mm. The L-shaped monopole antenna is attached to the center of one side of the mirrors and used for both transmission and detection. Because an optimum length of the antenna depends on the frequency of the irradiated microwave, we must choose the most suitable one for the frequency. The distance between the two mirrors is adjusted by a stepping motor so that the cavity resonance frequency coincides to the input microwave frequency. In other words, the distance is always set to a multiple of the

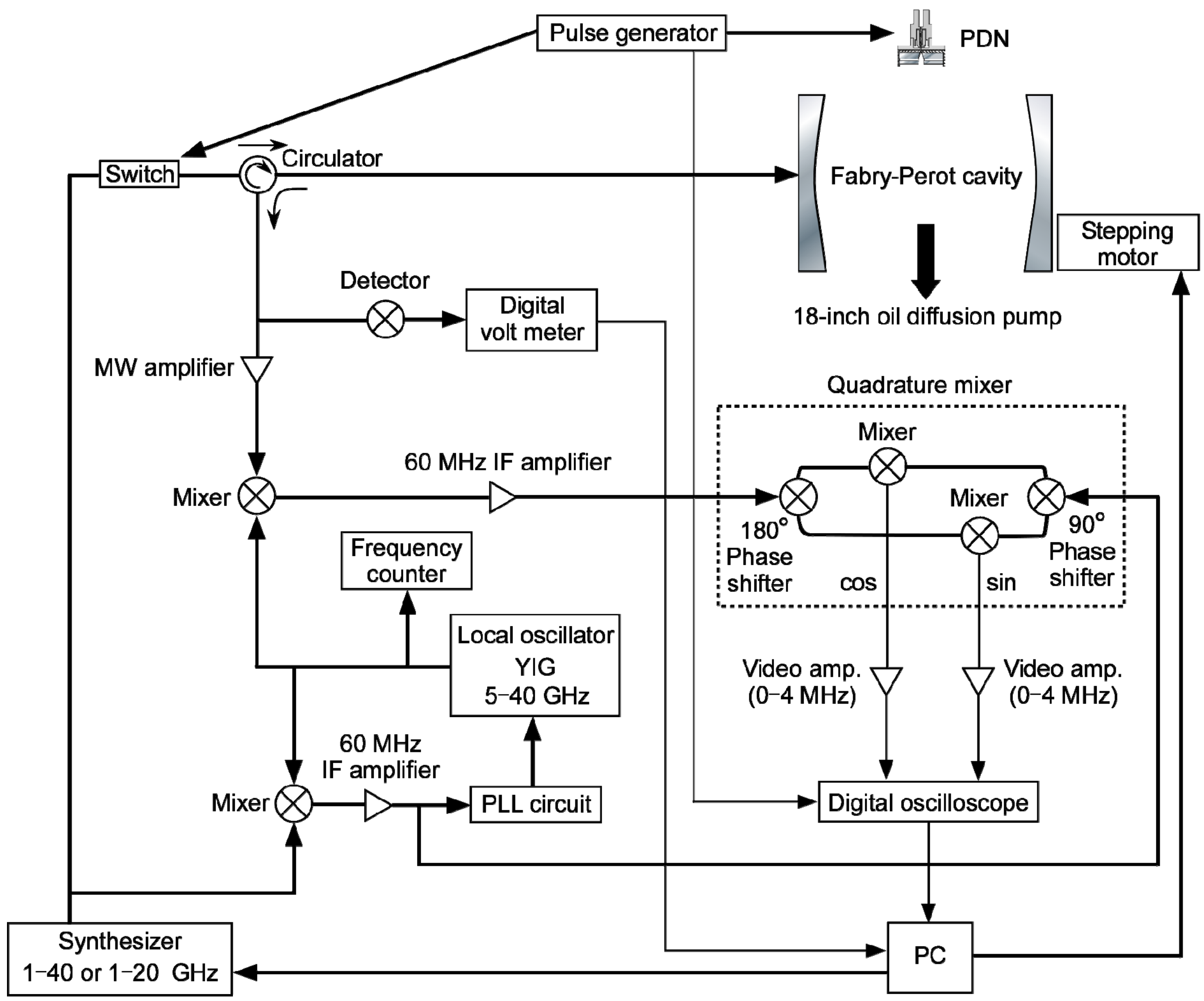

Figure 2.4. Block diagram of our FTMW spectrometer.

half-wavelength of the microwave. This condition is achieved by controlling the mirror distance so that the microwave reflected from the cavity is minimized. The PDN is set in the vacuum chamber in two arrangements: perpendicular (Fig. 2.5(a)) or parallel (Fig. 2.5(b)) to the travelling direction of the irradiated microwave. The parallel arrangement suppresses the Doppler broadenings of spectral lines and consequently provides a higher resolution. In addition, in the parallel arrangement, the Doppler doublings are observed, whereas no doubling is observed in the perpendicular arrangement. Synchronized to a supersonic expansion of a sample gas mixture from the PDN, a pulsed microwave is irradiated. FID signals emitted from the polarized molecules in the jet are detected by the same L-shaped monopole antenna. The signals are subsequently digitized by a digital oscilloscope (Iwatsu-LeCroy LT344L), in which 3200 waveform points are acquired with a sampling rate

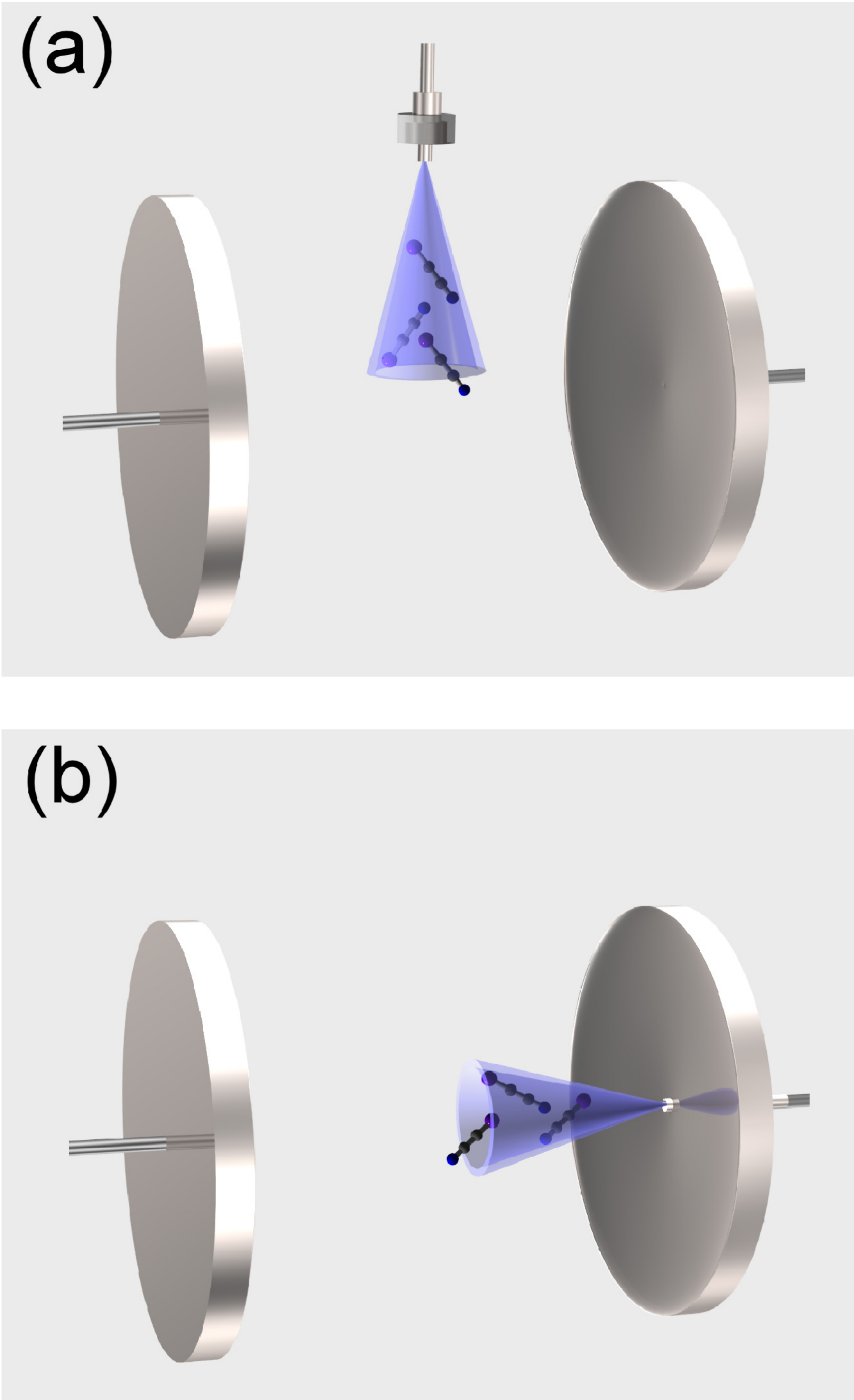

Figure 2.5. Schematic diagrams of the Fabry-Perot cavities. Nozzles are set in two arrangements: perpendicular (a) or parallel (b) to the travelling direction of the microwave.

of 25 MS/s. A Fourier-transformation of 512 points of signals obtained by a 6 points moving average of the input signals provides a spectrum in time-domain. The timing of the system is controlled by a home-made timing generator. A timing chart for the system is shown in Fig. 2.6. A microwave pulse is fired typically ~0.6 ms after the discharge pulse, because the distance from the nozzle to the center of the cavity is ~30 cm and a flow velocity of the jet is ~500 ms^{-1}. The data sampling with the oscilloscope is started ~3μs after the microwave pulse to avoid an influence of a residual electromagnetic field of the incident microwave in the cavity. The system is operated at a repetition rate of 10 Hz. In the cycle, a valve opening is processed alternately and the signal obtained with the valve closed is used as a background data. Subtracting the background data from the signal data obtained with the valve open, we obtain a data to be subjected to the Fourier-transformation. When a spectrum of a paramagnetic (**S** ≠ 0) species is observed, three-axis Hermholtz coils are used to cancel the earith's magnetic field at the center of the cavity.

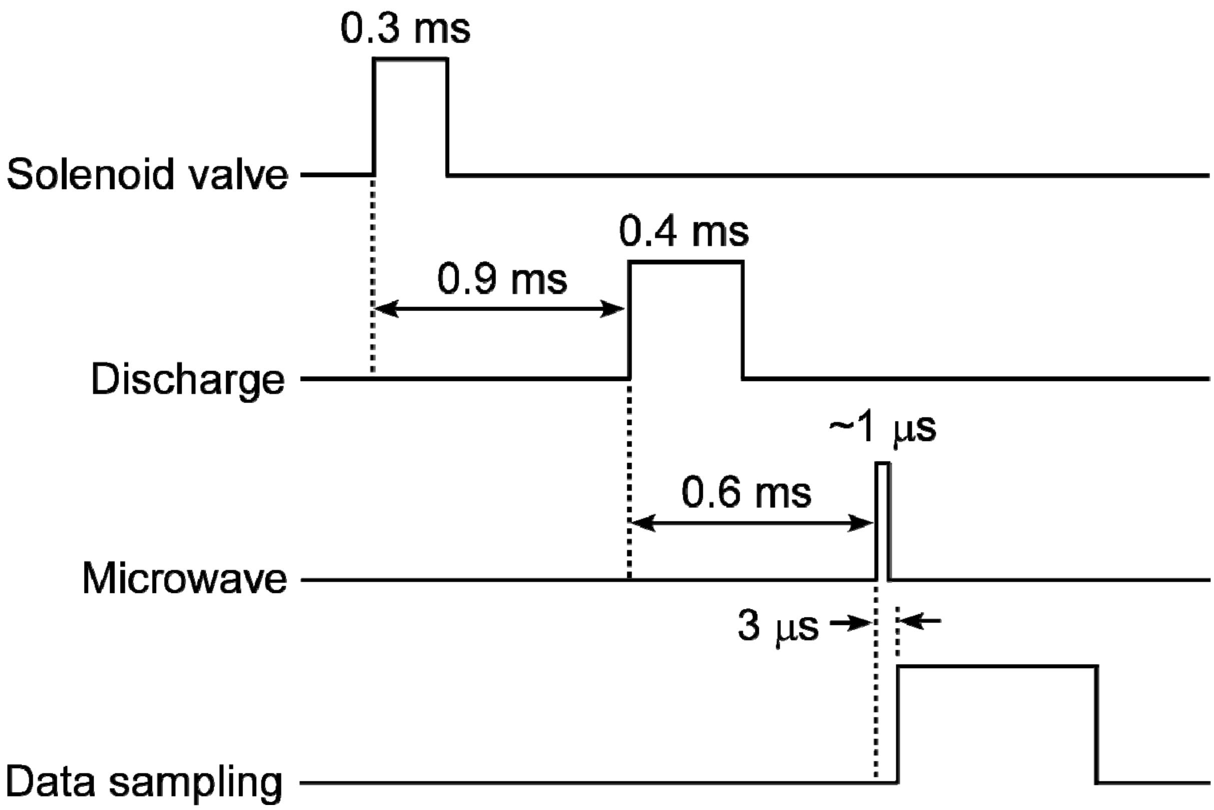

Figure 2.6. Timing chart for the system of our FTMW spectrometer.

A highly sensitive detection method, called superheterodyne system, is adopted in our instrument. In the system, an FID signal with its frequency of 4−40 GHz is finally down-converted to a signal with a frequency of 0−1 MHz, via 60 MHz intermediate frequency (IF). Processing such low-frequency signals takes an advantage of amplifying them, because an amplification efficiency of a signal increases as its frequency is low. The low-frequency signals are obtained by two steps of the down-conversion. First, FID signals are mixed with outputs of a local oscillator (YIG) tuned to the frequency 60 MHz off from that of the synthesizer, providing IF signals at the frequency of ~60 MHz. In the second step, the down-converted signal is further demodulated by a quadrature mixer using the 60 MHz beat signal, giving two zero-beat signals with a 90-degree phase difference. Outputs of the local oscillator are mixed with those of the synthesizer, and the beat signal at the frequency of 60 MHz is obtained. During the experiment, the phase of the local oscillator is synchronized to that of the synthesizer by a phase-locked loop (PLL) circuit. The two zero-beat signals are amplified and transferred to the oscilloscope. In this way, we can amplify the FID signals efficiently. The frequency of the two zero-beat signals, 0−1 MHz, corresponds to the difference in frequency between the FID signal and the synthesizer. This is eventually converted to the frequency domain signal by performing a complex Fourier-transformation of the two signals. The quadrature mixer enables us to distinguish the upper and lower sideband of the FID signal.

FTMW-mmW double resonance spectroscopy

The FTMW spectrometer mentioned above is applicable only in the frequency range of 4−40 GHz. Thus, it is impossible to observe transitions with resonance frequencies above 40 GHz by the FTMW spectrometer. We extended the frequency coverage up to the mm-wave bands, 40−110, 150−180, and 268−282 GHz, by introducing a new method called FTMW-mmW double resonance spectroscopy.[8,9] This technique combines the FTMW spectrometer with mm-wave light sources such as Gun oscillators. The mm-wave sources used in our laboratory are Gunn oscillators (65−110 GHz), frequency doublers of the output

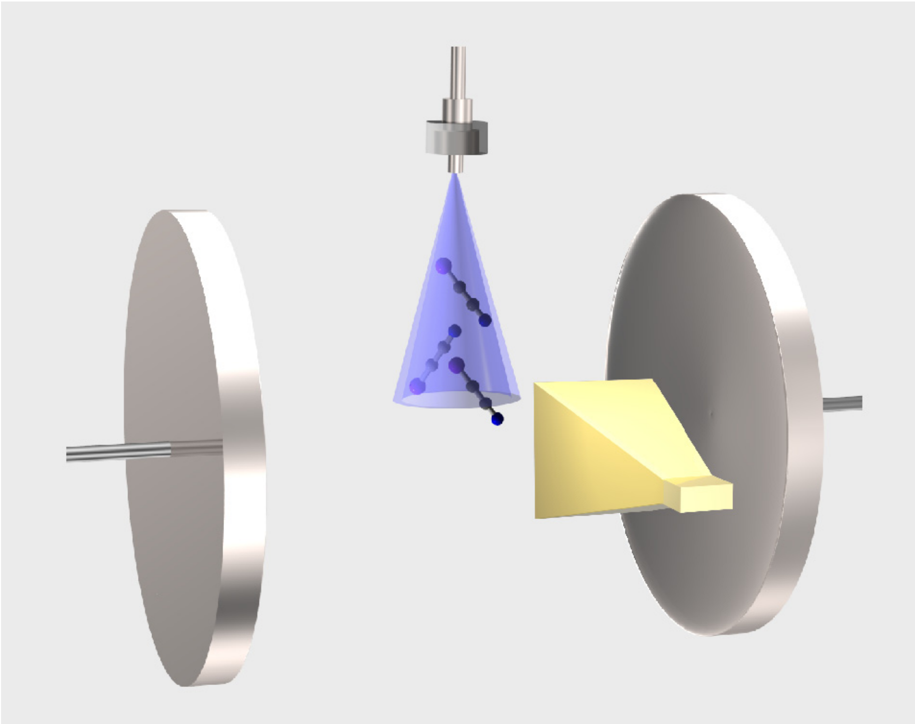

Figure 2.7. Setup for the FTMW-mmW double resonance spectroscopic system.

of the synthesizer (40−70 GHz), and doublers and triplers of the Gunn oscillators (150−180 and 268−282 GHz). A setup for the double-resonance spectroscopic system is presented in Fig. 2.7. As seen in the figure, the mm-wave source is placed at the right angle to the cavity axis. Figure 2.8 shows two types of mm-wave transitions observable in the technique. The double-resonance method is applicable only to a mm-wave transition sharing either a lower (Fig. 2.8(a)) or upper (Fig. 2.8(b)) level of a FTMW transition. Consider the situation that a frequency of the mm-wave is swept while the FTMW transition $|2\rangle \leftarrow |1\rangle$ is monitored. When the mm-wave frequency coincides with the resonance frequency of the transition $|3\rangle \leftarrow |1\rangle$, the intensity of the monitored FID signals decreases since the population of $|1\rangle$ is reduced. In contrast, when the mm-wave transition $|3\rangle \leftarrow |2\rangle$ is induced, the intensity of the monitored FID signals increases because the population difference between $|1\rangle$ and $|2\rangle$ becomes larger. In these ways, the mm-wave transitions are observed as changes of the FID signals of the monitored FTMW transitions. Note that there is an additional process causing the double resonance signals other than the population changes: coherence

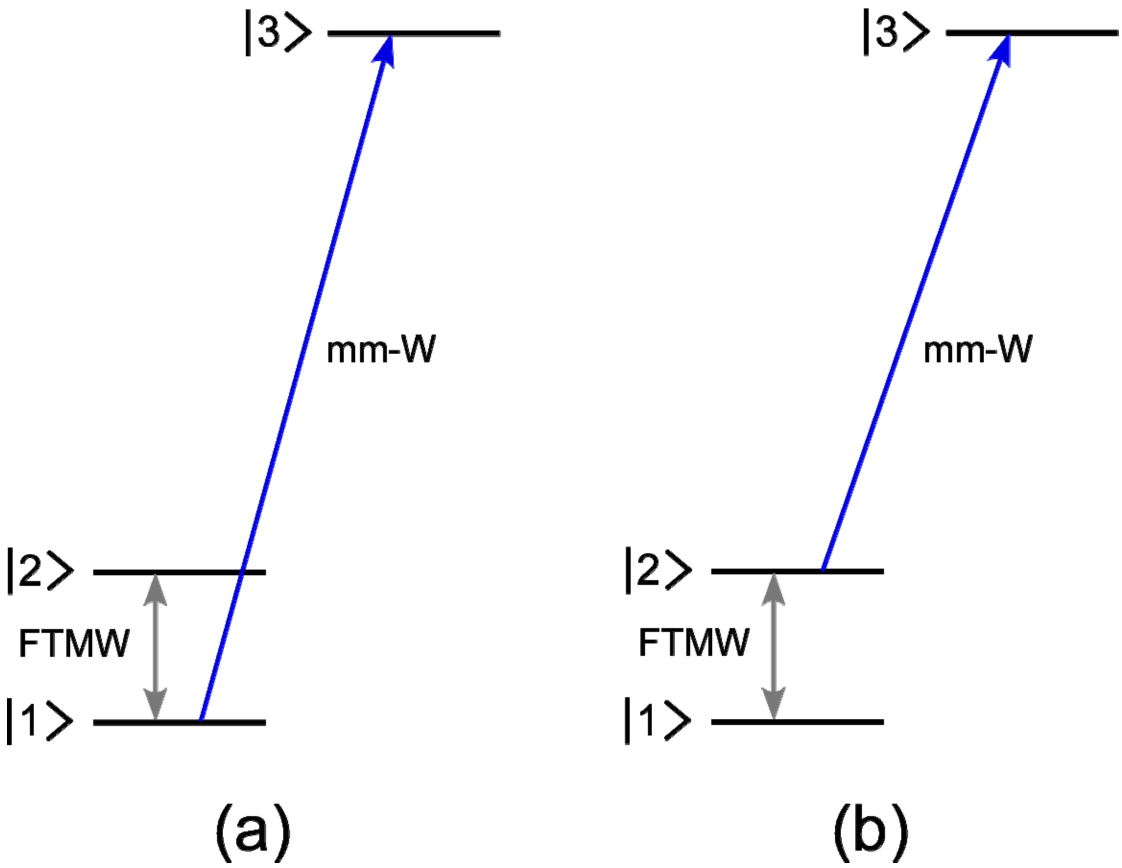

Figure 2.8. Two observable mm-wave transitions in the FTMW-mmW double resonance technique. The two transitions share lower (a) and upper (b) levels of a FTMW transition, respectively.

changes. In this process, the coherence between the two monitored levels is destroyed by the continuous mm-wave radiation, and consequently the intensity of the monitored FID signals decrease. In contrast to the population changes, the coherence destruction always decreases the intensity of the monitored FID signals. In principle, the coherence is thoroughly destroyed, in other words, the monitored signals are completely depleted by the latter mechanism, whereas the depletion rate does not exceed 50 % through the population changes. We should pay attention on treatments of these two different processes, because in a certain case they could contribute to the double resonance signals oppositely and provide a loss of the signals. The competition occurs in observing the transition $|3\rangle \leftarrow |2\rangle$ (Fig.

2.8(b)). In this case, the increase of the population difference between $|1\rangle$ and $|2\rangle$ induced by the continuous mm-wave radiation contributes to the increase of the double resonance signals, while the coherence destruction contributes oppositely. It is, however, still possible to avoid the competition for the measurement below 70 GHz, where frequency doublers of the synthesizer are used as the mm-wave source. The mm-wave radiation is able to be switched by the microwave switch. A timing chart of the switch of the mm-wave pulse is presented in Fig. 2.9. When the mm-wave radiation is switched off just before the microwave pulse, only the population change is induced. On the other hand, when it is irradiated just after the microwave pulse, the coherence destruction mainly contributes. Because it is impossible to switch the mm-wave radiation above 70 GHz, we must select a transition sharing its lower level with a mm-wave transition to be observed (Fig. 2.8(a)).

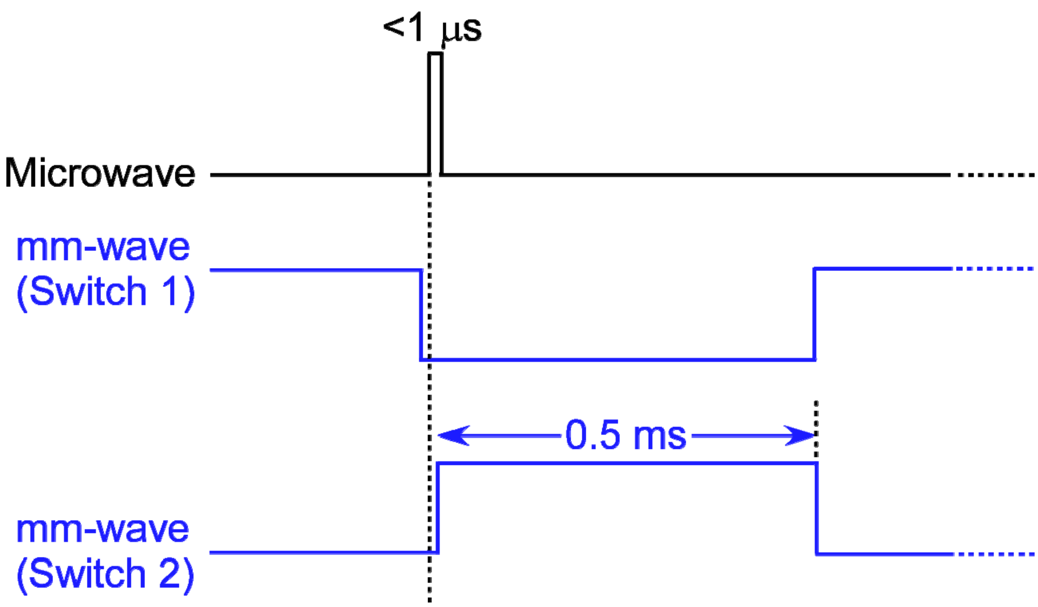

Figure 2.9. Timing chart for the switching of the mm-wave radiation. When the mm-wave radiation is switched off just before the microwave pulse (Switch 1), only the population change is induced. In contrast, when the mm-wave radiation is switched on after the microwave pulse (Switch 2), the coherence change mainly contributes.

2.3 Laser spectroscopy

FTMW spectroscopy is a powerful tool providing spectroscopic constants of molecules with high accuracy. The method is, however, inapplicable to non-polar molecules and it gives no information on properties of molecules in electronically excited states. In contrast, laser spectroscopy enables us to investigate vibronic structures of electronic excited states and changes of the geometrical structures arising from the electronic transitions. Furthermore, laser spectroscopy is applicable to non-polar molecules. Its sensitivity is comparable to that of FTMW spectroscopy. In our laboratory, UV-visible emission spectra are observed using pulsed dye lasers pumped by Q-switched Nd:YAG lasers. It is possible to observe rotationally-resolved electronic spectra unless molecules to be observed are not so large, with B > 0.04 cm^{-1}, for example. Additionally, by dispersing wavelengths of the fluorescence signals from an electronically excited molecule, we can obtain a spectrum giving vibrational structures of its ground electronic state. This section describes two optical spectroscopic methods adopted in our laboratory.

Laser induced fluorescence (LIF) spectroscopy

Electronic energies in atoms and molecules correspond to the UV-visible light. Applying the UV-visible radiation which satisfies the Bohr condition, $E' - E'' = h\nu$, to a molecule causes a change of the electronic configuration of the molecule. The process is called the electronic transition or electronic excitation. Molecules in the electronic excited state can give rise to the UV-visible light emissions through the spontaneous emission. The emitted light is so-called fluorescence. In the spontaneous emission, the photon is emitted in space isotropically, and the phase of the photon is random, which are not the case for the stimulated emission. The UV-visible light emission induced by a laser irradiation is called a laser induced fluorescence (LIF). A schematic diagram of two different LIF spectroscopic methods is shown in Fig. 2.10. An electronic excitation spectrum of a molecule is obtained by detecting all the fluorescence signals from the electronically excited molecule while

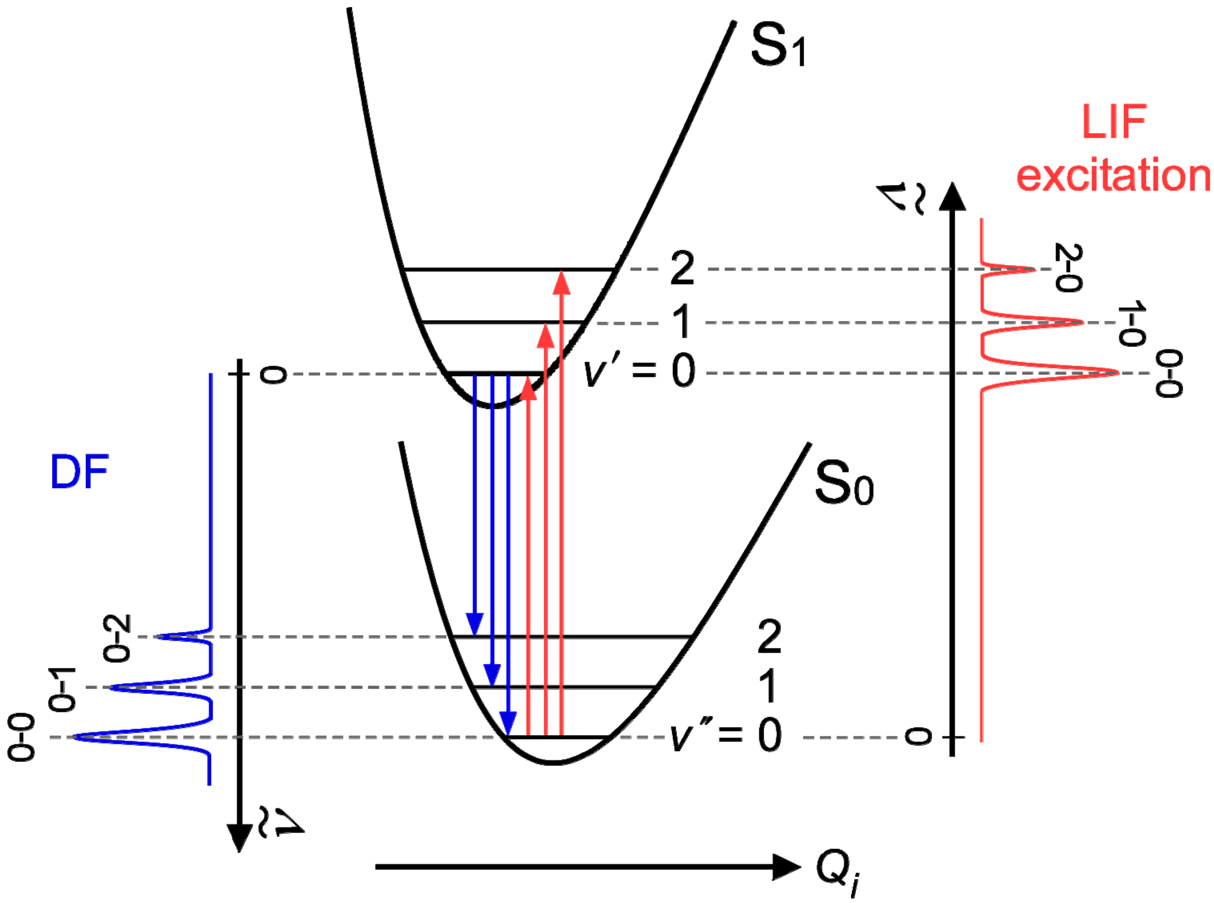

Figure 2.10. Schematic diagram of the LIF excitation and DF spectroscopy. Progression bands for Q_i th vibrational mode are shown.

sweeping the wavelength of the excitation laser. This technique is called LIF excitation spectroscopy. When it is combined with the supersonic jet technique, electronic transitions only from electronic ground states are observed because molecules produced in the jet are distributed almost in their ground electronic states. As mentioned above, it is possible to observe emissions from an electronically excited molecule by dispersing the fluorescence signals using a monochromator with the dye laser fixed to a resonance wavelength. The emission spectrum thus observed provides information on the vibrational structures in the ground electronic state of the molecule. This emission spectroscopy is called dispersed fluorescence (DF) spectroscopy. Irradiations of the UV-visible light using high power lasers such as the pulsed dye laser induce the electronic transitions efficiently. A spectral linewidth of the outputs of the pulse dye laser is ~0.1 cm^{-1}. Furthermore, by inserting an étalon in the cavity of the dye laser, the linewidth is narrowed to ~0.02 cm^{-1}, which is suffieintly narrow to obtain rotationally-resolved LIF excitation spectra.

LIF spectroscopy enables us to investigate vibronic structures, even rotational structures in many cases, with a high sensitivity. However, it is not always the case. Molecules in electronic excited states can lose their internal energies through processes other than the fluorescence emissions, for example, a relaxation via an internal conversion. The non-radiative excited states are called "dark" states. For large molecules, the internal conversion can largely contribute to the loss of fluorescence emissions due to high densities of vibrational levels. LIF spectroscopy, in which fluorescences emitted by electronically excited molecules are detected, is inapplicable to the studies of such non-radiative levels. In this case, electronic transitions should be directly observed by absorption spectroscopy.

Fluorescence depletion (FD) spectroscopy

Fluorescence depletion (FD) spectroscopy is an optical-optical double resonance technique, and exhibits its power in observing non-radiative excited states. The fundamental principle of the technique is the same as that of FTMW-mmW double resonance spectroscopy. Figure 2.11 indicates a schematic diagram of FD spectroscopy. The double resonance technique requires two dye lasers pumped by different Nd:YAG lasers. One is used to monitor an electronic transition $|2\rangle \leftarrow |1\rangle$, and the other to probe a transition $|3\rangle \leftarrow |1\rangle$, where the electronic excited state $|3\rangle$ can be non-radiative. The probe laser is fired typically ~500 ns before the monitoring laser pulse. When a wavelength of the probe laser hits the resonance wavelength of the $|3\rangle \leftarrow |1\rangle$ transition, the population of the ground state $|1\rangle$ is reduced. Consequently, the monitored LIF is depleted as shown in Fig. 2.11. We can, thus, observe an electronic transition even terminating to a dark level. In addition to the observability of the dark states, FD spectroscopy has an advantage of assignments of observed vibronic bands. In LIF spectroscopy combined with the pulsed discharge method, vibronic bands of a molecule are often perturbed by emission bands arising from other discharge products. The problem, however, is not important in FD spectroscopy, since

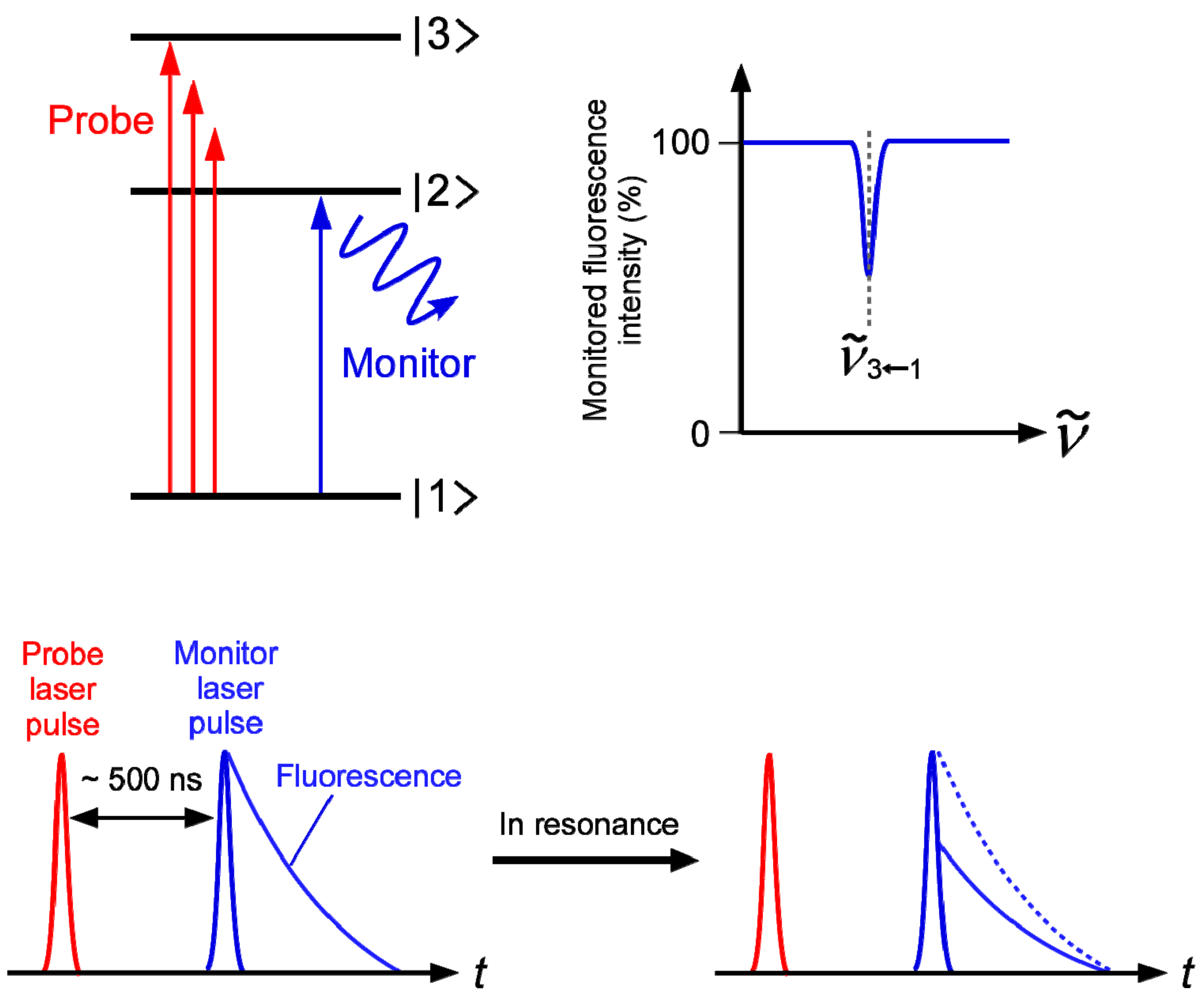

Figure 2.11. Schematic diagram of FD spectroscopy.

observed vibronic bands in the FD spectrum are originated from an identical species, whose fluorescence signals are monitored.

Apparatus

A block diagram of our laser spectroscopic system is presented in Fig. 2.12. Two pairs of dye lasers (Lambda Physics Scanmate 2E) and Nd:YAG lasers (Spectra Physics Lab-170-10, Spectra Physics GCR-230) are available in our laboratory. The dye lasers are pumped by the 2nd (532 nm) or 3rd (355 nm) harmonics of the Q-switched Nd:YAG lasers.

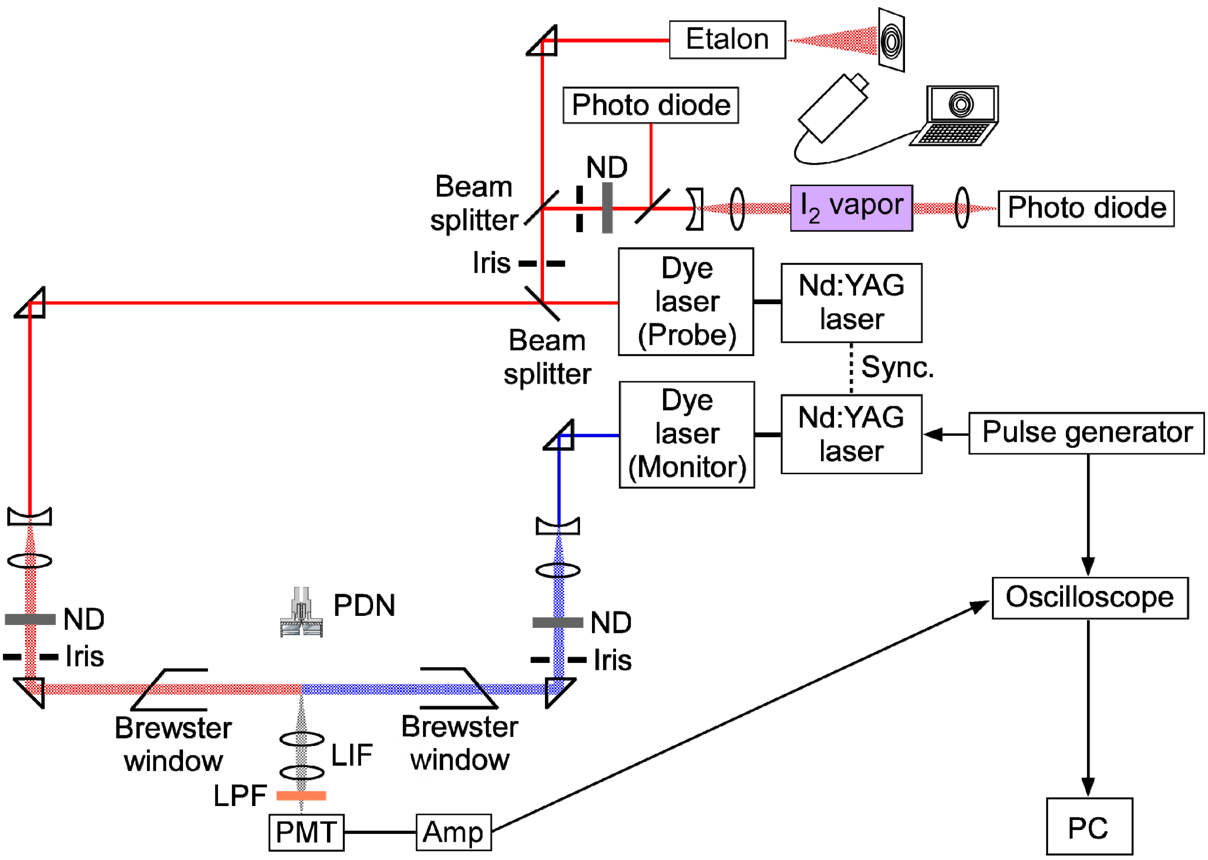

Figure 2.12. Block diagram of our laser spectroscopic system.

Optical paths are adjusted by optical prisms. In order to avoid a spectral saturation, the output beam of the dye laser is expanded to a diameter of ~1 cm by a telescope system. Subsequently, the beam is attenuated by neutral density (ND) filters, and introduced into a vacuum chamber via a Brewster window after passing through an iris. In measuring an FD spectrum, two output beams enter the chamber from the opposite sides with the beams overlapping to each other. The vacuum chamber is evacuated by a 14-inch oil diffusion pump (ULVAC ULK-14A, 4900 *l*/s) connected to a roots blower pump (SHINKO SMB-200, 56 *l*/s) and an oil rotary pump (EDWARDS E2M40, 10 *l*/s) as mechanical forepumps. The output beam is irradiated to the jet at 3−4 cm downstream from the PDN. LIF signals emitted from the discharge products are collected by two plano-convex lenses and detected by a photomultiplier tube (PMT; R3896 for 220−700 nm, R636-10 for 700−930 nm) at the right angle to the laser optical axis. A low-pass glass filter is set in front of the PMT to cut off the laser scattered lights. The arrangements of the PDN and the fluorescence detection unit are depicted in Fig. 2.13. In the DF spectroscopic study, a 0.5 m monochromator (Jobin Yvon SPEX 500M) is placed before the PMT. The detected signals are amplified and subsequently digitized with a digital oscilloscope (LeCroy 64MXs-B). The digitized signals are transferred to a personal computer (PC) and processed. It is possible to calibrate the absolute wavelength of the dye laser by simultaneously observing an absorption spectrum of the I_2 vapor. The output beam of the probe laser is divided into two beams by a beam splitter, one of which passes through a reference cell containing the I_2 vapor. A temperature of the vapor is adjusted by a heating wire depending on the wavelength of the probe laser. During the experiment, an interferometer fringe obtained by a passage of the output beam through an étalon is monitored, and the operation of the dye laser is confirmed from the visibility of the fringe pattern. The laser spectroscopic system is operated at a repetition rate of 10 Hz. The timing of each process is controlled by a home-made timing generator. A timing chart for the system is shown in Fig. 2.14. When a laser beam is irradiated at 4 cm downstream from the PDN, the laser radiation is fired 80 μs after a discharge pulse because of the gas flow velocity of 500 ms^{-1}.

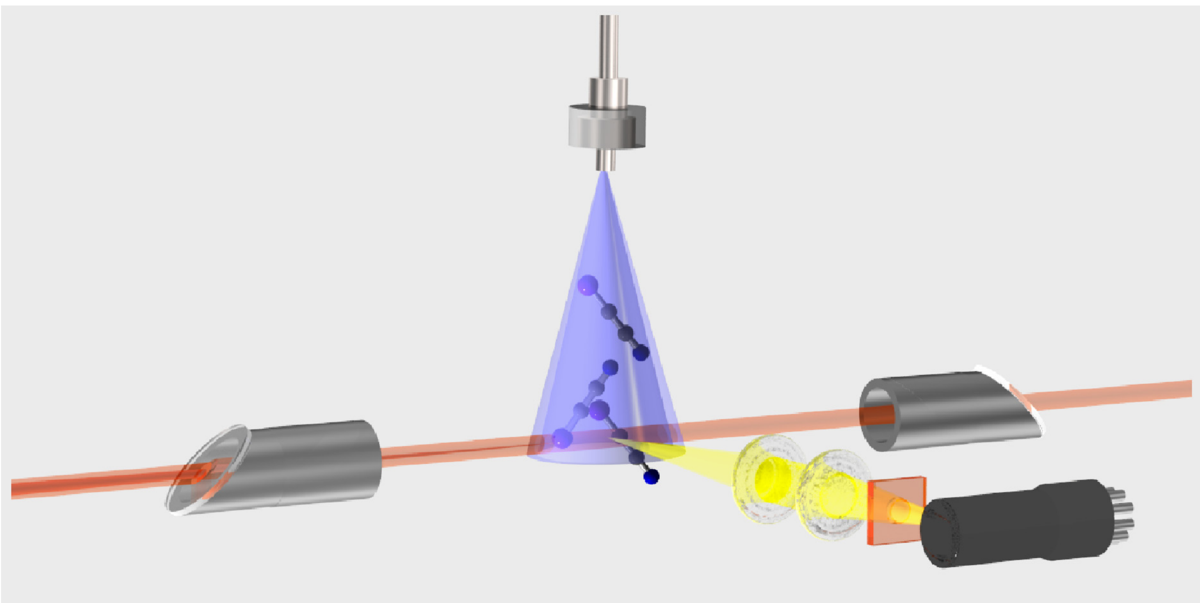

Figure 2.13. Arrangements of the PDN and LIF detection unit.

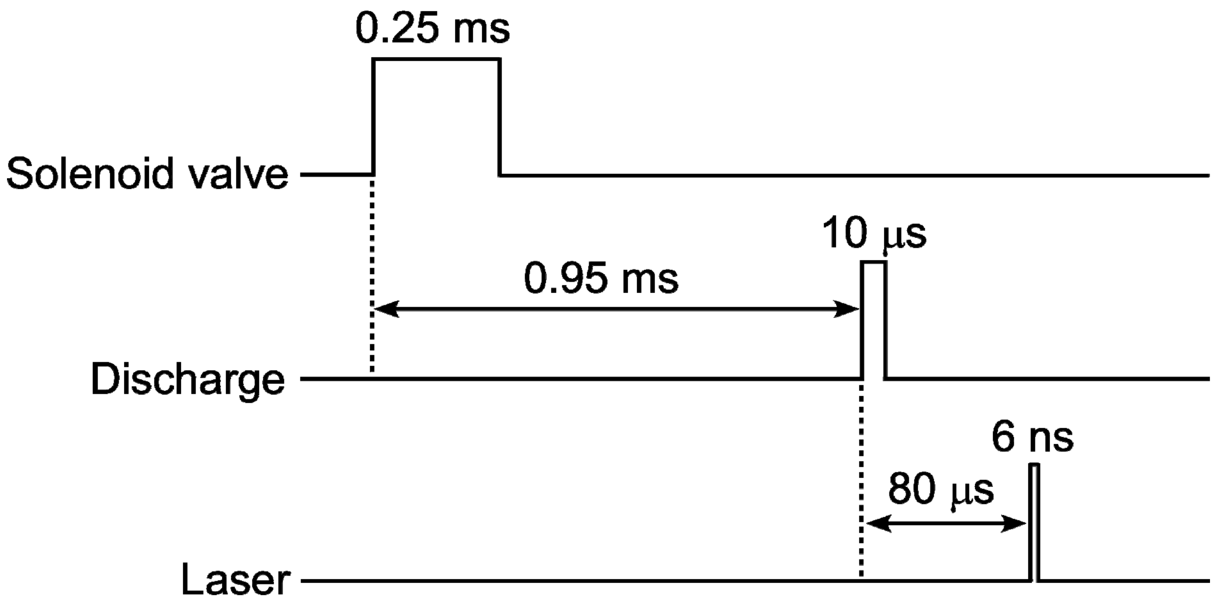

Figure 2.14. Timing chart for our laser spectroscopic system.

References

[1]E. Hirota, *High-Resolution Spectroscopy of Transient Molecules* (Springer, Berlin, 1985).

[2]Y. Endo, H. Kohguchi, and Y. Ohshima, Faraday Discuss. **97**, 341 (1994).

[3]J. B. Anderson and J. B. Fenn, Phys. Fluids. **8**, 780 (1965).

[4]R. E. Smalley, L. Wharton, D. H. Levy, Acc. Chem. Res. **10**, 139 (1977).

[5]R. E. Smalley, L. Wharton, D. H. Levy, J. Chem. Phys. **63**, 4977 (1965).

[6]J. Ekkers and W. H. Flygare, Rev. Sci. Instrum. **47**, 448 (1976).

[7]T. J. Balle and W. H. Flygare, Rev. Sci. Instrum. **52**, 33 (1981).

[8]W. Jäger and M. C. L. Gerry, J. Chem. Phys. **102**, 3587 (1995).

[9]Y. Sumiyoshi, H. Katsunuma, K. Suma, and Y. Endo, J. Chem. Phys. **123**, 054324 (2005).

Chapter 3
Microwave Spectroscopy of the Allenyloxy Radical ($CH_2{=}CCHO$)

3.1 Introduction

Oxidation intermediates of simple unsaturated hydrocarbons such as ethylene (C_2H_4), propylene (C_3H_6), and allene (C_3H_4) have been known to play important roles in combustion processes of hydrocarbon fuels as has been reviewed in Chapter 1. The reaction of allene with the ground state oxygen atom (^3P) has thus attracted much attention in combustion chemistry, and many studies have been reported.[1−10] In 1993, a crossed molecular beam experiment by Schmoltner *et al.* identified the allenyloxy radical ($CH_2{=}CCHO$) for the first time as a product in the reaction of allene with the oxygen atom (^3P),[8] where two reaction channels were identified unambiguously; a major channel producing C_2H_4 + CO and a minor generating $CH_2{=}CCHO$ + H. Very recently, Leonori *et al.* also detected the $CH_2{=}CCHO$ radical by a similar crossed molecular beam experiment and found additional reaction channels yielding C_2H_2 + H_2CO, C_2H_3 + HCO, and CH_2CO + CH_2.[10] To our knowledge, however, no spectroscopic study on the $CH_2{=}CCHO$ radical has been reported.

The ground state $CH_2{=}CCHO$ radical has an interesting feature on its electronic structure, since it has two resonant structures, allenyloxy ($CH_2{=}C{=}CH{-}\dot{O}$) and formylvinyl ($CH_2{=}\dot{C}{-}CH{=}O$) forms, similar to the cases for the vinoxy and its substituted radicals. Endo *et al.* have observed pure rotational spectra of the vinoxy radical in the millimeter-wave region, and have determined its molecular constants.[11] From the Fermi contact constants, the spin density on the carbon atom in the methylene group has been estimated to be slightly less than 80%, showing that the formylmethyl ($\dot{C}H_2{-}CH{=}O$) form is the major contributor to the $^2A''$ ground electronic state. Nakajima *et al.* have reported the rotational spectra of CH_2CHS by Fourier-transform microwave (FTMW) and FTMW-millimeter wave double-resonance spectroscopy, where they have concluded that the two canonical forms, $\dot{C}H_2{-}CH{=}S$ and $CH_2{=}CH{-}\dot{S}$, contribute equally to the actual structure of CH_2CHS based on the experimentally determined spin-rotation constant.[12] The molecular constants including the hyperfine interaction constants have also been determined for CH_2CFO by FTMW spectroscopy,[13] and the contribution of the formylmethyl form ($\dot{C}H_2{-}CF{=}O$) has been estimated to be about 85%, which is similar to the result of the CH_2CHO system, indicating that the fluorine atom substitution gives a very small effect on the electronic structure. In 1990, the electronic structure of $CH_2{=}CCHO$ was investigated theoretically by Hammond *et al.*, where the molecular orbital calculations were performed at the CASSCF/DZ level of theory for the three low-lying electronic states.[7] The result of the study has indicated that $CH_2{=}CCHO$ in the $^2A''$ ground electronic state has a linear C−C−C backbone with the C−C−O π orbital perpendicular to the terminal C−C π orbital, and that the formylvinyl form ($CH_2{=}\dot{C}{-}CH{=}O$) is dominant between the two canonical forms.

In the present study, we report the first spectroscopic detection of the $CH_2{=}CCHO$ radical. The rotational spectra of this molecule were observed by FTMW spectroscopy and the FTMW-millimeter wave double-resonance technique. The molecular constants in the $^2A''$ ground electronic state were determined precisely. The molecular geometry and electronic structure of the ground state $CH_2{=}CCHO$ are discussed based on the spectroscopic constants and results of *ab initio* calculations.

3.2 *Ab initio* calculation

A geometrical optimization of $CH_2{=}CCHO$ was carried out using the spin-restricted coupled cluster method with single and double excitations and perturbative treatment of triples, RCCSD(T), with Dunning's correlation-consistent polarized valence triple-zeta (cc-pVTZ) basis set. At the optimized geometry, dipole moments along the *a*- and *b*-inertial axes were calculated at the same level of theory as that for the geometrical optimization. The calculations were performed using the MOLPRO 2012.1 package.[14] The fine and hyperfine coupling constants of the $CH_2{=}CCHO$ radical were estimated at the second order Møller–Plesset perturbation (MP2) and the quadratic configuration interaction with single and double excitations (QCISD) levels of calculations, respectively, with the cc-pVTZ basis set. These calculations were performed using the GAUSSIAN 03 package.[15]

The calculated geometry of CH_2=CCHO in the $^2A''$ ground electronic state is depicted in Fig. 3.1 together with the unpaired electron orbital, where two hydrogen atoms of the methylene group are numbered 1 and 2, the other hydrogen atom is numbered 3, and three carbon atoms are numbered 1 to 3 from the methylene group side. Hereafter, we refer to the numbering in Fig. 3.1. The calculated geometrical parameters, the rotational constants, and the dipole moments are summarized in Table 3.1. These results show that CH_2=CCHO has C_s symmetry and has a linear C−C−C backbone with the C−C−O π orbital perpendicular to the terminal C−C π orbital, and that the unpaired electron is almost localized on the central carbon atom, as discussed by Hammond *et al.*[7]

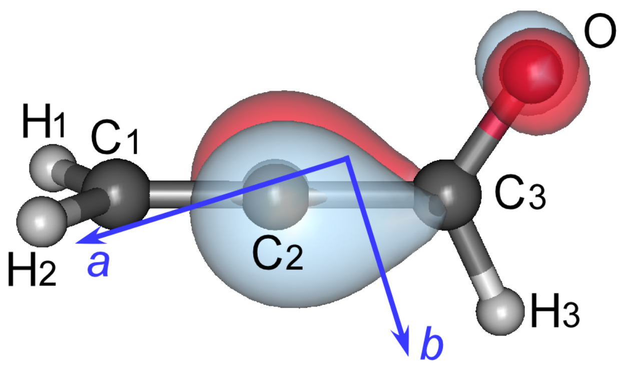

Figure 3.1. Geometry and the unpaired electron orbital of CH_2=CCHO in the $^2A''$ ground electronic state calculated at the RCCSD(T)/cc-pVTZ level of theory. The colors of the orbital lobes reflect the phases of the orbital.

Table 3.1. *Ab initio* geometrical parameters, rotational constants, and permanent dipole moments of CH_2CCHO.[a]

$R(CH_1)$	(Å)	1.087
$R(CH_2)$	(Å)	1.087
$R(CH_3)$	(Å)	1.100
$R(C_1C_2)$	(Å)	1.305
$R(C_2C_3)$	(Å)	1.408
$R(C_3O)$	(Å)	1.237
$\angle H_1C_1C_2$	(degree)	121.3
$\angle H_2C_1C_2$	(degree)	121.3
$\angle H_3C_3C_2$	(degree)	115.4
$\angle C_1C_2C_3$	(degree)	180.0
$\angle C_2C_3O$	(degree)	123.3
A	(MHz)	51534.1
B	(MHz)	4495.7
C	(MHz)	4256.0
μ_a	(debye)	2.83
μ_b	(debye)	1.30

[a]RCCSD(T)/cc-pVTZ

3.3 Experiment

Since the experimental setup has been described in Chapter 2, only a brief explanation is given here. The CH_2=CCHO radical was produced by the pulsed electric discharge in a gas mixture, 0.3% CH_2=CCH−O−CH_3 (methoxyallene) diluted in Ar, using the PDN system. The gas mixture was expanded into the vacuum chamber at the stagnation pressure of 3 atm, where the pressure in the vacuum chamber was kept at 3×10^{-5} torr. Synchronized to the gas expansion, a pulsed high voltage of 1.1 kV with a duration of 400 μs was applied between the stainless steel electrodes. Pure rotational transitions were observed using the FTMW spectrometer. In order to resolve the hyperfine splittings, the PDN was arranged in parallel to the Fabry-Perot cavity to reduce the Doppler width (Fig. 2.5(b)).

3.4 Results and analysis

In the present experiment, *a*-type transitions of CH_2=CCHO were observed by FTMW spectroscopy. At first, we searched the $3_{03}-2_{02}$ transition, which is predicted to be observed around 26.3 GHz. Nineteen paramagnetic lines were observed in the 26.5 GHz region, and they were readily assigned to the $3_{03}-2_{02}$ transition of CH_2=CCHO. Figure 3.2 shows an example of the spectrum of the $3_{03}-2_{02}$ transition. As shown in Fig. 3.2, one rotational line splits into two peaks because of the Doppler doubling. The observed spectral pattern is shown in Fig. 3.3. The two fine-structure components have hyperfine structures caused by two protons, H_1 and H_2 with fairly large splittings, and each of the hyperfine components further splits into two with smaller splittings by the third proton, showing complicated spectral structures. The double-resonance technique (see Chapter 2) was employed for the observations of two *b*-type transitions, $2_{12}-1_{01}$ and $3_{13}-2_{02}$, in the 64 and 73 GHz regions, respectively. The double resonance spectra of the $2_{12}-1_{01}$ and $3_{13}-2_{02}$ transitions were observed as changes of the signal intensity of the monitored transitions, $2_{02}-1_{01}$ and $3_{03}-2_{02}$, respectively. Figure 3.4 shows an example of the double-resonance spectrum of the $2_{12}-1_{01}$ transition. Finally, a total of 143 lines were observed, which are composed of *a*-type transitions with $N = 1-0$, $2-1$, and $3-2$ for $K_a'' = 0$ and 1, and two *b*-type transitions, $2_{12}-1_{01}$ and $3_{13}-2_{02}$. All the observed transition frequencies are given in Appendix I.

To confirm the possibility of the generation of CH_2=CCHO by the reaction of allene with the oxygen atom, two measurements were performed using mixture gases of 0.5% allene / 1.0% O_2 and 0.5% allene / 1.0% N_2O both diluted in Ar as precursors. No spectra of CH_2=CCHO were observed using the allene / O_2 / Ar mixture. On the other hand, spectra

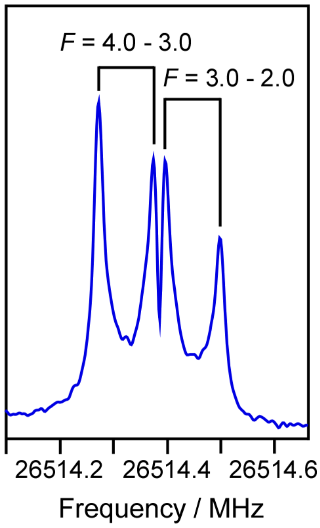

Figure 3.2. Rotational lines of 3_{03}−2_{02}, J = 3.5−2.5, F_1 = 3.5−2.5 observed by FTMW spectroscopy. This spectrum was obtained by accumulating 300 shots of pulses at a repetition rate of 5 Hz.

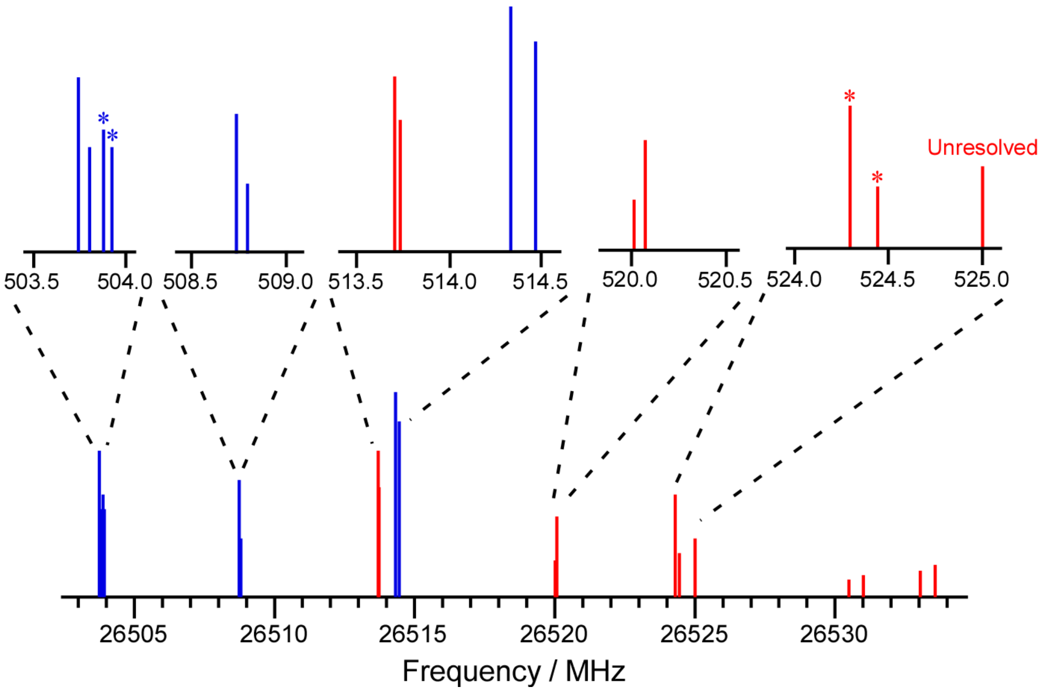

Figure 3.3. Stick diagram of the observed lines of the 2_{02}−1_{01} transition. The blue and red colors of the sticks are the fine structure components with J = 3.5−2.5 and J = 2.5−1.5, respectively. The upper traces are drawn in an expanded scale, where small hyperfine splittings due to the third proton are identified. Sticks with asterisks are the I_1 = 0 transitions.

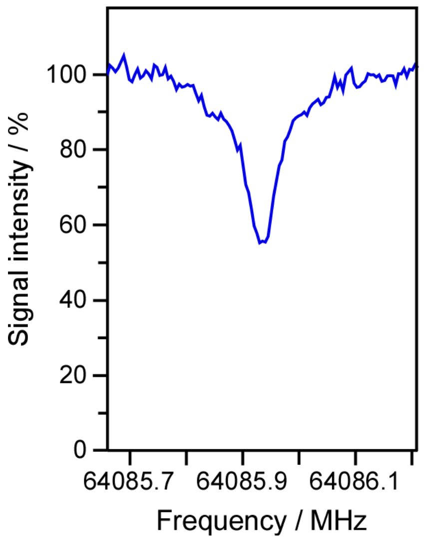

Figure 3.4. Double resonance spectrum of $2_{12}-1_{01}$, J = 2.5−1.5, F_1 = 3.5−2.5, F = 4.0−3.0 observed by monitoring the $2_{02}-1_{01}$, J = 2.5−1.5, F_1 = 3.5−2.5, F = 4.0−3.0 transition. The vertical axis corresponds to the signal intensity of the monitored transition.

of CH_2=CCHO were obtained using the allene / N_2O / Ar mixture, where the intensity, however, was about 10-times weaker than that using the mixture gas of 0.3% CH_2=CCH−O−CH_3 / Ar.

The observed transitions were analyzed using the Hamiltonian appropriate for doublet asymmetric top molecules with the centrifugal distortion expressed in Watson's A-reduced form.[16] The explicit form of the Hamiltonian and its matrix elements are given in Appendix II. An appropriate coupling scheme for the nuclear spin angular momenta of the three protons is necessary to properly reproduce the observed hyperfine structure. The results of the molecular orbital calculations indicate that CH_2=CCHO has C_s symmetry and the two protons of the methylene group have the same hyperfine interaction constants except for an off-diagonal component of the dipolar-constant. Hence, the two protons were able to be treated equivalently, which is not the case for CH_2CHO and CH_2CHS. The coupling scheme used in the present study is $\mathbf{J} = \mathbf{N} + \mathbf{S}$, $\mathbf{F}_1 = \mathbf{J} + \mathbf{I}_1$, and $\mathbf{F} = \mathbf{F}_1 + \mathbf{I}_2$, where $\mathbf{I}_1 = \mathbf{I}^{(\mathrm{H}_1)} + \mathbf{I}^{(\mathrm{H}_2)}$ and $\mathbf{I}_2 = \mathbf{I}^{(\mathrm{H}_3)}$. Resultant I_1 takes the value, 0 or 1. Since the interchange of the two protons, H_1 and H_2, is not possible by any overall rotations, $I_1 = 0$ and

1 patterns are observed simultaneously for all the rotational levels. The hyperfine interaction term $\mathbf{H}_{hfs}$ is thus written explicitly as a two spin system,

$$\mathbf{H}_{hfs} = a_F{}^{(\mathrm{H}_1,\mathrm{H}_2)}\,\mathbf{S}\cdot\mathbf{I}_1 + \mathbf{I}_1\cdot\mathbf{T}^{(\mathrm{H}_1,\mathrm{H}_2)}\cdot\mathbf{S} + a_F{}^{(\mathrm{H}_3)}\,\mathbf{S}\cdot\mathbf{I}_2 + \mathbf{I}_2\cdot\mathbf{T}^{(\mathrm{H}_3)}\cdot\mathbf{S}\,, \tag{3.1}$$

where a_F and $\mathbf{T}$ stand for the Fermi contact constant and the dipole-dipole interaction tensor, respectively, and $a_F{}^{(\mathrm{H}_1,\mathrm{H}_2)}$ and $\mathbf{T}^{(\mathrm{H}_1,\mathrm{H}_2)}$ are averages of the coupling constants for the two protons:

$$a_F{}^{(\mathrm{H}_1,\mathrm{H}_2)} = \left(a_F{}^{(\mathrm{H}_1)} + a_F{}^{(\mathrm{H}_2)}\right)/2\,, \tag{3.2}$$

$$\mathbf{T}^{(\mathrm{H}_1,\mathrm{H}_2)} = \left(\mathbf{T}^{(\mathrm{H}_1)} + \mathbf{T}^{(\mathrm{H}_2)}\right)/2\,. \tag{3.3}$$

Note that the first and second terms in Eq. (3.1) are not exactly equivalent to the following terms,

$$\mathbf{H}_{hfs}{}^{(\mathrm{H}_1,\mathrm{H}_2)} = a_F{}^{(\mathrm{H}_1)}\,\mathbf{S}\cdot\mathbf{I}^{(\mathrm{H}_1)} + a_F{}^{(\mathrm{H}_2)}\,\mathbf{S}\cdot\mathbf{I}^{(\mathrm{H}_2)} + \mathbf{I}^{(\mathrm{H}_1)}\cdot\mathbf{T}^{(\mathrm{H}_1)}\cdot\mathbf{S} + \mathbf{I}^{(\mathrm{H}_2)}\cdot\mathbf{T}^{(\mathrm{H}_2)}\cdot\mathbf{S}\,. \tag{3.4}$$

The Fermi interaction terms in Eq. (3.4), for example, are

$$\begin{aligned} a_F{}^{(\mathrm{H}_1)}\,\mathbf{S}\cdot\mathbf{I}^{(\mathrm{H}_1)} + a_F{}^{(\mathrm{H}_2)}\,\mathbf{S}\cdot\mathbf{I}^{(\mathrm{H}_2)} &= \left(\frac{a_F{}^{(\mathrm{H}_1)} + a_F{}^{(\mathrm{H}_2)}}{2}\right)\mathbf{S}\cdot\left(\mathbf{I}^{(\mathrm{H}_1)} + \mathbf{I}^{(\mathrm{H}_2)}\right) \\ &\quad + \left(\frac{a_F{}^{(\mathrm{H}_1)} - a_F{}^{(\mathrm{H}_2)}}{2}\right)\mathbf{S}\cdot\left(\mathbf{I}^{(\mathrm{H}_1)} - \mathbf{I}^{(\mathrm{H}_2)}\right) \\ &= a_F{}^{(\mathrm{H}_1,\mathrm{H}_2)}\,\mathbf{S}\cdot\mathbf{I}_1 + \left(\frac{a_F{}^{(\mathrm{H}_1)} - a_F{}^{(\mathrm{H}_2)}}{2}\right)\mathbf{S}\cdot\left(\mathbf{I}^{(\mathrm{H}_1)} - \mathbf{I}^{(\mathrm{H}_2)}\right). \end{aligned} \tag{3.5}$$

Similarly, the dipole-dipole interaction terms in Eq. (3.4) are

$$\mathbf{I}^{(\mathrm{H}_1)}\cdot\mathbf{T}^{(\mathrm{H}_1)}\cdot\mathbf{S} + \mathbf{I}^{(\mathrm{H}_2)}\cdot\mathbf{T}^{(\mathrm{H}_2)}\cdot\mathbf{S} = \mathbf{I}_1\cdot\mathbf{T}^{(\mathrm{H}_1,\mathrm{H}_2)}\cdot\mathbf{S} + \left(\mathbf{I}^{(\mathrm{H}_1)} - \mathbf{I}^{(\mathrm{H}_2)}\right)\cdot\left(\frac{\mathbf{T}^{(\mathrm{H}_1)} - \mathbf{T}^{(\mathrm{H}_2)}}{2}\right)\cdot\mathbf{S}\,. \tag{3.6}$$

By neglecting the terms,

$$\left(\frac{a_F{}^{(\mathrm{H}_1)} - a_F{}^{(\mathrm{H}_2)}}{2}\right)\mathbf{S}\cdot\left(\mathbf{I}^{(\mathrm{H}_1)} - \mathbf{I}^{(\mathrm{H}_2)}\right)$$

and

$$\left(\mathbf{I}^{(\mathrm{H}_1)} - \mathbf{I}^{(\mathrm{H}_2)}\right)\cdot\left(\frac{\mathbf{T}^{(\mathrm{H}_1)} - \mathbf{T}^{(\mathrm{H}_2)}}{2}\right)\cdot\mathbf{S}\,,$$

Eq. (3.1) is derived. These two terms connect levels only off-diagonal in K_a, and thus scarcely contribute the energy level structures in the present case. Hence, the two protons were treated as if they are equivalent.

At first, transitions with $I_1 = 0$ were analyzed, since the hyperfine structure is caused only by the third proton. With the help of the prediction of the spectral pattern using the calculated molecular constants, transitions with $I_1 = 0$ were assigned and the molecular constants except for the hyperfine constants of H_1 and H_2 were tentatively determined. Again, the spectral pattern was simulated using the tentatively determined molecular constants, and assignments for the remaining lines including the $I_1 = 1$ transitions were attempted. In this way, assignments for all the observed lines were accomplished. Seventeen molecular constants were determined by the least-squares analysis for all the observed transition frequencies. The standard deviation of the fit is 10.0 kHz, which is comparable to the experimental accuracy of the measurements, indicating that the complicated hyperfine structures caused by the three protons in the CH_2=CCHO system were well described in terms of the two spin system. The determined molecular constants are summarized in Table 3.2 along with those calculated by *ab initio* calculations. The Fermi contact constants of CH_2=CCHO are compared with those of the related molecules, CH_2CHO,[11,17] CH_2CHS,[18] and CH_2CFO,[13] in Table 3.3.

Table 3.2. Molecular constants of the CH_2=CCHO radical (in MHz).[a]

	Exp.	*ab initio*
A	51282.0209(35)	51534.1[b]
B	4544.26552(77)	4495.7[b]
C	4295.17971(94)	4256.0[b]
Δ_N	0.002035(43)	
Δ_{NK}	−0.11796(41)	
ε_{aa}	−500.244(22)	−730.25[c]
ε_{bb}	−40.799(25)	−62.12[c]
ε_{cc}	−0.757(22)	3.71[c]
Δ_N^S	0.00362(22)	
Δ_{NK}^S	0.0383(55)	
δ_N^S	0.00355(48)	
$a_F^{(\mathrm{H_1,H_2})}$	136.2100(31)	115.93[d]
$T_{aa}^{(\mathrm{H_1,H_2})}$	5.7150(73)	6.46[d]
$T_{bb}^{(\mathrm{H_1,H_2})}$	−3.2958(91)	−3.74[d]
$a_F^{(\mathrm{H_3})}$	−1.0303(58)	−2.23[d]
$T_{aa}^{(\mathrm{H_3})}$	3.032(12)	5.01[d]
$T_{bb}^{(\mathrm{H_3})}$	1.754(14)	0.56[d]
Inertial defect / uÅ^2	−3.41	−3.48
σ_{fit} / kHz	10.0	

[a]Values in parentheses denote 1σ errors applied to the last digits.

[b]RCCSD(T)/cc-pVTZ.

[c]MP2/cc-pVTZ.

[d]QCISD/cc-pVTZ.

Table 3.3. Comparison of the Fermi contact constants of CH_2=CCHO with those of related molecules (in MHz).

	CH_2=CCHO	CH_2CHO[a]	CH_2CHS[b]	CH_2CFO[c]
$a_F^{(H_1)}$ [d]	136.2	−54.6	−31.4	−60.3
$a_F^{(H_2)}$ [d]	136.2	−56.5	−29.3	−61.4
$a_F^{(X)}$ [e]	−1.0	−0.6[f]	4.6	−23.3

[a]Ref. 11.

[b]Ref. 18.

[c]Ref. 13.

[d]H_1 and H_2 are hydrogen atoms of the methylene group. H_1 is on the same side as O for CH_2CHO and CH_2CFO, and S for CH_2CHS.

[e]X = H_3 for CH_2=CCHO, CH_2CHO, and CH_2CHS, while X = F for CH_2CFO.

[f]Ref. 17.

3.5 Discussion

As summarized in Table 3.2, the experimentally determined rotational constants and the inertial defect, which is mainly contributed by the two protons lying out of the symmetry plane, agree well with the *ab initio* values, implying that the calculated molecular structure is reasonable. The *ab initio* C_2−C_3 bond length, 1.408 Å, is clearly longer than the carbon-carbon double bond length of ethylene, 1.334 Å,[19] and the *ab initio* C_3−O bond length, 1.237 Å, is close to the carbon-oxygen double bond length of formaldehyde, 1.203 Å,[19] showing that the C_2−C_3 and C_3−O bonds of CH_2=CCHO have mostly single- and double-bond characters, respectively. The *ab initio* geometry thus indicates that the formylvinyl (CH_2=$\dot{C}$−CH=O) form dominantly contributes to the electronic structure for the $^2A''$ ground state. The unpaired electron has also been predicted to be located mainly on the central carbon atom as shown in Fig. 3.1.

The spin-rotation coupling constant ε_{aa} is approximately given by a second-order expression,[20]

$$\varepsilon_{aa} \approx -\frac{4A\,A_{\mathrm{SO}}}{E(\tilde{A})-E(\tilde{X})}, \tag{3.7}$$

where A and A_{SO} are the rotational constant and the effective spin-orbit interaction constant along the a-axis, respectively. In order to estimate the A_{SO} value using Eq. (3.7), the energy difference, $E(\tilde{A})-E(\tilde{X})$, was calculated with the RCCSD(T)/cc-pVTZ level of theory at the optimized geometry for the $\tilde{X}\ ^2A''$ state. Using the determined ε_{aa} and A together with the calculated energy difference of 12916 cm^{-1}, A_{SO} is estimated to be 31.5 cm^{-1}. This value is very close to the spin-orbit interaction constant of the carbon atom, $A_{\mathrm{SO}}(\mathrm{C})$ = 29.0 cm^{-1},[21] but is much smaller than that of the oxygen atom, $A_{\mathrm{SO}}(\mathrm{O})$ = 151.0 cm^{-1},[21] supporting that CH_2=CCHO has the spin density mostly on the central carbon atom.

The Fermi contact constant a_F gives information on the unpaired electron density at the proton.[22] This constant is explicitly expressed as

$$a_F = \frac{8\pi}{3} g_S g_N \mu_B \mu_N \left|\psi_{1s}(0)\right|^2, \tag{3.8}$$

where g_S and g_N are the electron and nuclear g-factors, μ_B and μ_N are the Bohr and nuclear magnetons, $\left|\psi_{1s}(0)\right|$ is the unpaired electron density at the proton. From Eq. (3.8), it is apparent that the Fermi contact constant a_F is non-zero only if $\left|\psi_{1s}(0)\right|^2$ has a finite value, in other words, if the unpaired electron orbital has s-character. All the parameters appearing on the right side in Eq. (3.8) have positive values, and thus a_F is usually a positive value. In the case of HCO, for example, the unpaired electron lies in in-plane orbital, giving the large positive a_F value, ~391 MHz.[23] Such radicals are called σ radicals, and they generally have large positive values for a_F. In contrast, radicals with out-plane unpaired electron orbitals are called π radicals. In the case of the π radical, such as CH_2CHO, the proton lies in the nodal plane of the unpaired electron orbital. Hence, the π radicals seem to have no values for a_F. In fact, however, the π radicals have small negative a_F values. The negative a_F value of the π radical is explained by a negative net spin in the hydrogen 1s orbital arising from the spin-polarization effects. Figure 3.5 shows a schematic diagram of the spin-polarization effect in a π radical with the form R_1R_2CH. In

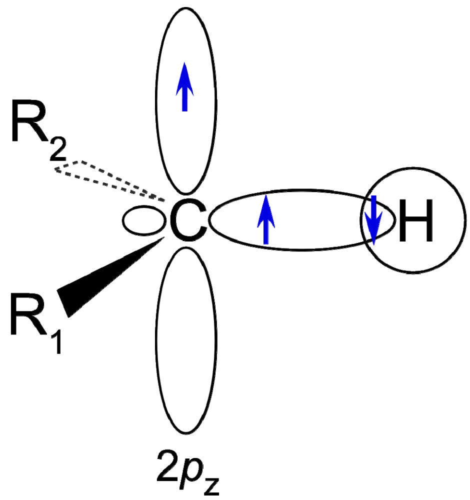

Figure 3.5. Schematic diagram of the spin-polarization effect. The unpaired electron occupies the carbon $2p_z$ orbital.

Fig. 3.5, the unpaired electron in the carbon $2p_z$ orbital causes the spin-polarization in the sp^2-bonding orbital. As seen in the figure, the positive net spin density is induced in the carbon orbital through the spin exchange interaction, yielding the negative net spin in the hydrogen 1*s* orbital. Consequently, the negative values were given for a_F of the π radicals. As listed in Table 3.2, for CH_2=CCHO, the positive values were determined for the a_F constants of the two protons H_1 and H_2, whereas the negative a_F value was determined for the third proton H_3. These results indicate that H_1 and H_2 are located outside of the nodal plane of the unpaired electron orbital and H_3 is in the nodal plane, consistent with the predictions of the molecular structure and the unpaired electron orbital depicted in Fig. 3.1. Furthermore, it is different from the cases of the planar π radicals such as CH_2CHO, CH_2CHS and CH_2CFO, where all the protons are in the nodal plane of the π orbital of the unpaired electron, giving negative signs for a_F through the spin polarization effect.

The principal axis values of the dipole-dipole interaction tensors for the three protons of CH_2=CCHO have been determined precisely, which reasonably agree with the *ab initio* values as shown in Table 3.2. The signs of the principal axis values of the dipole-dipole interaction tensor reflect the spatial distribution of the unpaired electron. When the unpaired electron occupies the p_π orbital of atom X, the component along the H−X bond has a positive value, and the component perpendicular to both the H−X bond and the p_π orbital has a negative value. Figure 3.6 shows the *ab initio* molecular geometry and unpaired electron orbital of CH_2=CCHO. In the case of CH_2=CCHO, $T_{aa} > 0$ and $T_{bb} < 0$ for the two equivalent protons H_1 and H_2, and $T_{aa} > 0$ and $T_{bb} > 0$ for the third proton H_3. As shown in Fig. 3.6, these results indicate that the central carbon atom has the unpaired electron in the p_π orbital perpendicular to the plane of the formyl group, consistent with the previous discussions. When the unpaired electron is localized in the oxygen p_π orbital perpendicular to the plane of the formyl group, T_{aa} for H_3 should have a negative value. The magnitudes of T_{aa} and T_{bb} for the three protons in CH_2=CCHO are comparable with each other, meaning that the unpaired electron is located at essentially the same distances from the three protons, namely, on the central carbon atom, since the magnitudes of the dipole-dipole interaction constants is proportional to the factor r^{-3}, where r is the distance between the unpaired electron and the proton.

The production of CH_2=CCHO by the reaction of allene with the oxygen atom was confirmed in the measurement using N_2O as an oxygen source, while it was not detected in the measurement using O_2 instead of N_2O. Dissociation of O_2 by an electric discharge mainly produces the ground state oxygen atom (^{3}P), as pointed out by Schmoltner *et al.*[8] and Leonori *et al.*,[10] who applied a microwave discharge to induce the dissociation of O_2. On the other hand, dissociation of N_2O may produce the excited state oxygen atom (^{1}D), since

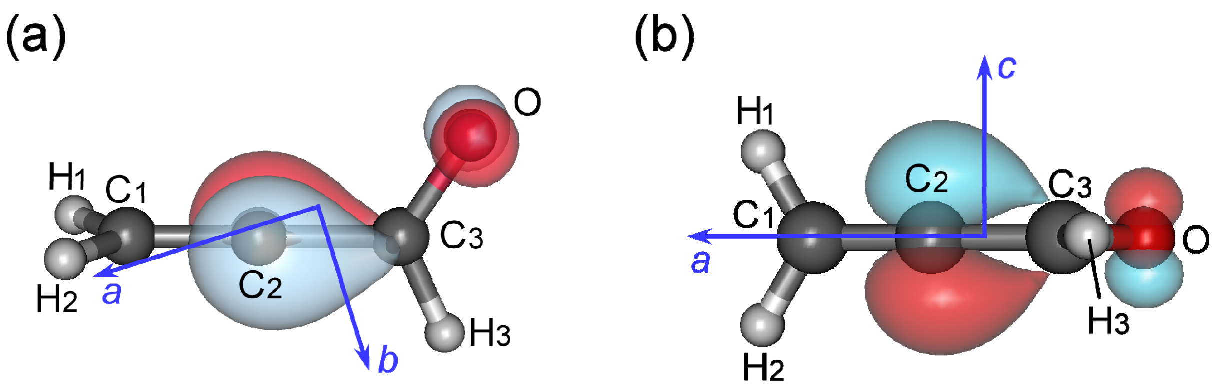

Figure 3.6. Calculated molecular geometry and unpaired electron orbital of the ground state CH_2=CCHO viewed from (a) c-axis and (b) b-axis directions, respectively.

the ground and three low-lying excited states of N_2O, $\tilde{X}\,^1A'$, $2\,^1A'$, $1\,^1A''$ and $2\,^1A''$, correlate to the O (^{1}D) + N_2 ($^1\Sigma_g^+$) dissociation limit, as suggested by the recent theoretical study.[24] It is, thus, considered that allene reacts mainly with O (^{3}P) and O (^{1}D) in the measurements using allene / O_2 and allene / N_2O mixtures, respectively, and the efficiency to produce CH_2=CCHO is much higher for the latter case.

We also attempted to observe electronic spectra of CH_2=CCHO by LIF spectroscopy. Molecular orbital calculations at RS2(11e,10o)/cc-pVTZ level of theory predicted a relatively strong transition, $\tilde{C}\,^2A'' \leftarrow \tilde{X}\,^2A''$, at ~29500 cm^{-1}, in which the transition dipole moment was calculated to be about 0.5 D. The $\tilde{C}-\tilde{X}$ band was searched in the region from 28000−32000 cm^{-1} under the same experimental condition as that in the microwave spectroscopic study. However, no spectrum was observed, possibly because non-radiative relaxation processes are dominant in the $\tilde{C}\,^2A''$ state.

References

[1]V. P. Herbrechtsmeier and H. G. Wagner, Ber. Bunsenges. Phys. Chem. **76**, 517 (1972).

[2]J. J. Havel, J. Am. Chem. Soc. **96**, 530 (1974).

[3]M. C. Lin, R. G. Shortridge, and M. E. Umstead, Chem. Phys. Lett. **37**, 279 (1976).

[4]R. Atkinson and J. N. Pitts, Jr., J. Chem. Phys. **67**, 2492 (1977).

[5]Y.-N. Chiu and M. S. F. A. Abidi, J. Phys. Chem. **86**, 3288 (1982).

[6]K. A. Singmaster and G. C. Pimentel, J. Mol. Struct. **194**, 215 (1989).

[7]B. L. Hammond, S.-Y. Huang, W. A. Lester, Jr., and M. Dupuis, J. Phys. Chem. **94**, 7969 (1990).

[8]A. M. Schmoltner, S. Y. Huang, R. J. Brudzynski, P. M. Chu, and Y. T. Lee, J. Chem. Phys. **99**, 1644 (1993).

[9]T. L. Nguyen, J. Peeters, and L. Vereecken, J. Phys. Chem. A **110**, 12166 (2006).

[10]F. Leonori, A. Occhiogrosso, N. Balucani, A. Bucci, R. Petrucci, and P. Casavecchia, J. Phys. Chem. Lett. **3**, 75 (2012).

[11]Y. Endo, S. Saito, and E. Hirota, J. Chem. Phys. **83**, 2026 (1985).

[12]M. Nakajima, A. Miyoshi, Y. Sumiyoshi, and Y. Endo, J. Chem. Phys. **126**, 044307 (2007).

[13]A. Watanabe, Y. Sumiyoshi, and Y. Endo, J. Chem. Phys. **130**, 224304 (2009).

[14]H.-J. Werner, P. J. Knowles, F. R. Manby, M. Schütz *et al.*, MOLPRO, version 2012.1, a package of *ab initio* programs, 2012, see http://www.molpro.net.

[15]M. J. Frisch, G. W. Trucks, and H. B. Schlegel *et al.*, GAUSSIAN, Revision E.01, Gaussian, Inc., Pittsburgh, PA, 2003.

[16]J. K. G. Watson, J. Chem. Phys. **46**, 1935 (1967).

[17]Y. Endo, M. Nakajima, J. Mol. Spec. **301**, 15 (2014).

[18]T. Tokumasu, Y. Sumiyoshi, and Y. Endo, to be published.

[19]J. L. Duncan, Mol. Phys. **28**, 1177 (1974).

[20]R. F. Curl, Jr., J. Chem. Phys. **37**, 779 (1962).

[21]H. Lefebvre-Brion and R. W. Field, *Perturbations in the Spectra of Diatomic Molecules* (Academic, New York, 1986) p. 214.

[22]J. R. Morton, Chem. Rev. **64**, 453 (1964).

[23]J. M. Brown, K. Dumper, and R. S. Lowe, J. Mol. Spec. **97**, 441 (1983).

[24]R. Schinke, J. Chem. Phys. **134**, 064313 (2011).

Chapter 4
Microwave Spectroscopy of SiC_2N and SiC_3N

4.1 Introduction

Silicon-bearing molecules have attracted much attention in astrophysics, since silicon has a relatively high cosmic abundance. Indeed, a wide variety of silicon-bearing molecules such as SiO,[1] SiS,[2] SiN,[3] SiC_n (n = 1−4),[4−7] SiCN,[8] and SiNC[9] have been detected in interstellar media, for example, in the circumstellar envelope of the carbon-rich evolved star IRC+10216. In addition, many N-terminated carbon chain molecules such as C_nN (n = 1−3, 5)[10−13] have been identified as interstellar molecules. It is thus expected that a series of silicon-bearing carbon chain molecules such as SiC_2N and SiC_3N may be detected in astronomical objects. Large dipole moments predicted from the present *ab initio* calculations, 3.8 and 3.5 D for SiC_2N and SiC_3N, respectively, also suggest the radicals as candidates for astronomical detections.

Studies of electronic structures of the SiC_nN radicals are of importance for understanding the origin of the difference from those of other related radicals. The isoelectronic radicals, $SiC_{n+1}H$ ($n \leq 5$), have been investigated by optical and microwave spectroscopy.[14−18] These studies have revealed that the $SiC_{n+1}H$ radicals with even and odd number carbons have linear structures with the $^2\Pi_r$ and $^2\Pi_i$ ground electronic states, respectively. The electronic structures of the isovalent radicals, $C_{n+1}N$ ($n \leq 5$), in the ground electronic states have also been studied extensively.[19−22] These investigations have clarified that C_3N and C_5N have the $^2\Sigma^+$ ground electronic states in contrast to their isovalent radicals, SiC_3H (Chapter 5) and SiC_5H, which have the $^2\Pi_i$ ground electronic states. On the other hand, CCN, C_4N, and C_6N have the $^2\Pi_r$ ground electronic states as are the cases for SiC_2H, SiC_4H, and SiC_6H. So far, experimental studies for the SiC_nN series have been limited to the shortest member, SiCN, in contrast to the related radicals. In 1998, Maier *et al*. detected the SiCN radical for the first time in an Ar matrix by infrared spectroscopy.[23] Two years later, Apponi *et al*. identified SiCN in the gas phase by Fourier transform microwave

(FTMW) and millimeter-wave absorption spectroscopy.[16] They concluded that SiCN has a linear structure in the $^2\Pi_r$ ground electronic state. Recently, the electronically excited state of SiCN, $\tilde{A}\,^2\Delta$, was also observed by Fukushima and Ishiwata.[24] For the longer members of the series, SiC_2N and SiC_3N, only information from theoretical studies is available.[25,26] It has been pointed out that the most stable isomers are linear with the $^2\Pi$ ground electronic states for both the systems. Moreover, SiC_2N and SiC_3N are expected to have the inverted and regular fine structures, respectively. Table 4.1 summarizes the symmetries of the ground electronic states expected for SiC_3N and SiC_3N, and those observed for their related radicals.

In the present study, we report laboratory detections of SiC_2N and SiC_3N by FTMW spectroscopy. Molecular constants including the hyperfine coupling constants were determ-

Table 4.1. Symmetries of the ground electronic states of SiC_nN and their related radicals.

even *n*	$n = 2$	$n = 4$	$n = 6$	Symmetry
SiC_nN	SiC_2N	···	···	$^2\Pi_i$
$SiC_{n+1}H$	SiC_3H[a]	SiC_5H[b]	···	$^2\Pi_i$
$C_{n+1}N$	C_3N[c]	C_5N[d]	···	$^2\Sigma^+$
odd *n*	$n = 1$	$n = 3$	$n = 5$	Symmetry
SiC_nN	SiCN[b]	SiC_3N	···	$^2\Pi_r$
$SiC_{n+1}H$	SiC_2H[b]	SiC_4H[b]	SiC_6H[b]	$^2\Pi_r$
$C_{n+1}N$	C_2N[e]	C_4N[f]	C_6N[f]	$^2\Pi_r$

[a]Reference 18.

[b]Reference 17.

[c]Reference 20.

[d]Reference 22.

[e]Reference 19.

[f]Reference 21.

ined for the two radicals. The experimentally determined constants were compared with other related radicals, and the spin density on the N atom was estimated for the two radicals on the basis of the magnetic hyperfine constants. It has been concluded that SiC_2N and SiC_3N have the $^2\Pi_i$ and $^2\Pi_r$ ground electronic states as expected. Furthermore, transition frequencies in the millimeter-wave region were predicted for both the radicals using the determined molecular constants. The predicted transition frequencies were compared with available line survey data toward IRC+10216, which led to the conclusion that no lines have been detected so far.

4.2 *Ab initio* calculation

Equilibrium molecular geometries, rotational constants B, and dipole moments μ were calculated at the RCCSD(T)/cc-pVQZ level of theory for SiC_2N and SiC_3N in the ground electronic states. The predicted molecular geometries and molecular constants are given in Fig. 4.1 and Table 4.2, respectively. As seen in Fig. 4.1, the linear equilibrium structures were obtained for both of the radicals. The calculated B constants were multiplied by scaling factors in order to obtain better values for spectral searches. The scaling factors for SiC_2N and SiC_3N were calculated as the ratios of the experimental B constants of SiC_3H[18] and SiC_4H[17] to those calculated at the RCCSD(T)/cc-pVQZ level of theory, respectively. The dipole moments were calculated to be 3.8 and 3.5 D for SiC_2N and SiC_3N, respectively.

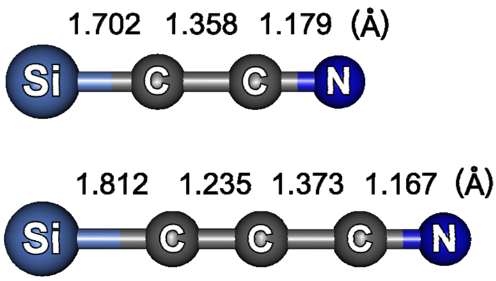

Figure 4.1. Optimized molecular geometries of SiC_2N and SiC_3N in their ground electronic states at the RCCSD(T)/cc-pVQZ level of theory.

The spin-orbit interaction constants A_{so} were calculated at the MRCI/cc-pVQZ level of theory based on the wave functions obtained by the MCSCF calculations, where bond lengths were constrained to those optimized at the RCCSD(T)/cc-pVQZ level of theory. In the MCSCF calculations for SiC_2N and SiC_3N, reference configurations were obtained by distributing 11 and 13 electrons in 9 and 11 valence orbitals, $10\sigma 2\pi 11\sigma 3\pi 4\pi 12\sigma$ and $12\sigma 2\pi 3\pi 13\sigma 4\pi 5\pi 14\sigma$, respectively. In the MRCI calculation for SiC_2N, the same active space as that in the MCSCF calculation was used, whereas the active space consisting of 11 electrons in 2π to 14σ orbitals was used for SiC_3N. The calculations gave the negative and positive values for the A_{so} constants of SiC_2N and SiC_3N, indicating the lower spin sub-levels of the radicals are $^2\Pi_{3/2}$ and $^2\Pi_{1/2}$, respectively. The calculated A_{so} value of SiC_2N, −66.8 cm^{-1}, was very close to the experimental A_{so} value of SiC_3H (Chapter 5), −65.6 cm^{-1}, indicating the validity of the calculated value. The electric quadrupole coupling constant eQq_0 and the magnetic hyperfine constants were predicted at the QCISD/cc-pVTZ level of theory at the RCCSD(T)/cc-pVQZ geometry. The Frosch and Foley[27] hyperfine constants defined as

$$a = 2g_N \mu_B \mu_N \langle \Lambda = 1 | r^{-3} | \Lambda = 1 \rangle , \tag{4.1}$$

$$b = b_F - \frac{c}{3} , \tag{4.2}$$

$$c = \frac{3}{2} g_S g_N \mu_B \mu_N \left\langle \frac{3\cos^2\theta - 1}{r^3} \right\rangle = 3 g_S g_N \mu_B \mu_N \langle \Lambda = 1 | C_0^2(\theta, \phi) r^{-3} | \Lambda = 1 \rangle , \tag{4.3}$$

$$d = \frac{3}{2} g_S g_N \mu_B \mu_N \left\langle \frac{\sin^2\theta}{r^3} \right\rangle = -\sqrt{6} g_S g_N \mu_B \mu_N \langle \Lambda = 1 | C_2^2(\theta, \phi) r^{-3} | \Lambda = 1 \rangle , \tag{4.4}$$

were also predicted. In Eqs. (4.1) to (4.4), r is the distance between the unpaired electron and the nucleus considered (nitrogen nucleus in the preset case), b_F is the Fermi contact interaction constant, $C_q^2(\theta, \phi)$ is related to the second-rank spherical harmonics as

$$C_q^2(\theta, \phi) = \sqrt{\tfrac{4\pi}{5}} Y_{2q}(\theta, \phi) . \tag{4.5}$$

These four magnetic hyperfine constants were derived from the dipole-dipole interaction tensor **T** and the Fermi contact constant b_F using the relations as,

$$b = b_F - \frac{1}{2} T_{aa} , \tag{4.6}$$

$$c = \frac{3}{2} T_{aa} , \tag{4.7}$$

$$d = T_{bb} - T_{cc} . \tag{4.8}$$

The derivations of Eqs. (4.6) to (4.8) are described in Appendix III (see Eqs.(A-III.22−30)). The constants *a* and *c*/*d* have slightly different physical meanings. An average of r^{-3} in Eq. (4.1) is over the spatial distribution of the unpaired electron, whereas those in Eqs. (4.3) and (4.4) are over the unpaired electron spin density. An approximate relation between *a*, *c*, and *d* is obtained by neglecting this difference,

$$c = 3(a - d) . \tag{4.9}$$ [28]

Using this approximation, the constant *a* is related to T_{aa} and T_{bb} as

$$a = \frac{c}{3} + d = \frac{3}{2} T_{aa} + 2T_{bb} . \tag{4.10}$$

Calculations of the hyperfine coupling constants were carried out using the GAUSSIAN 03 package.[29] The other calculations were performed using the MOLPRO 2012.1 package.[30]

Table 4.2. Predicted molecular constants of SiC_2N and SiC_3N (in MHz).

	SiC_2N ($\tilde{X}\,^2\Pi_i$)	SiC_3N ($\tilde{X}\,^2\Pi_r$)
A_{so} (cm^{-1})	-66.8^a	118.3^a
B	$2637.7^{b,c}$	$1415.0^{b,c}$
	2617.5^b	1398.8^b
$a+(b+c)/2$	13.51^d	3.17^d
$a-(b+c)/2$	30.69^d	11.34^d
b	7.74^d	0.31^d
d	30.40^d	10.09^d
eQq_0	-4.25^e	-4.46^e

^{a}MRCI/cc-pVQZ.

^{b}RCCSD(T)/cc-pVQZ.

^{c}Scaled by multiplying $B^{\text{Expt.}}/B^{\text{Calc.}}$ of the isoelectronic radical, $SiC_{n+1}H$.

^{d}Estimated using Eqs. (4.6) to (4.8) and (4.10), see text for details.

^{e}QCISD/cc-pVTZ.

4.3 Experiment

Since the experimental setup has been described in Chapter 2, only a brief explanation is given here. The gas mixture of 0.2% $SiCl_4$ and 0.2% CH_3CN diluted in Ar was used for the production of SiC_2N. For SiC_3N, 0.2% $SiCl_4$ and 0.2% HC_3N diluted in Ar was used. The gas mixture was expanded into the Fabry-Perot cavity with a backing pressure at 3 atm. During the experiment, the pressure inside the vacuum chamber was kept at 3.0×10^{-5} Torr. Synchronized to the gas expansion, a pulse voltage of 1500 V with a duration of 400 μs was applied between stainless steel electrodes attached to the PDN. The PDN was arranged parallel to the cavity in order to resolve small hyperfine splittings (Fig. 2.5(b)). For both the radicals, pure rotational transitions with ΔF = 1 were observed by FTMW spectroscopy. For SiC_3N, weak ΔF = 0 transitions were observed utilizing the MW-MW double-resonance technique (see Chapter 2). Although the $\Delta F = 0$ transitions are more than 10 times weaker than the $\Delta F = 1$ transitions, the double-resonance method enabled us to observe such very weak lines when sufficiently large power was applied for the pumping radiation.

4.4 Observed spectra

SiC_2N

On the basis of the transition frequencies calculated from the scaled B constant, 2638 MHz, rotational transitions were searched by FTMW spectroscopy. At first, we searched the $J = 5.5-4.5$ transition, calculated at 28.975 GHz. Three paramagnetic lines, which could be assigned to the hyperfine components due to the nitrogen ($I = 1$) nucleus, were observed. The observed spectrum of $J = 5.5-4.5$, $F = 6.5-5.5$ is shown in Fig. 4.2. As seen in the figure, Λ-doubling was not resolved, presumably due to a very small Λ-doubling constant of SiC_2N as expected by analogy with SiC_3H.[18] The observed lines show a relatively large broadening due to a residual earth's magnetic field, preventing us from resolving the doubling. The $J = 4.5-3.5$ transition were then searched around 23.7 GHz. Three paramagnetic lines with similar line intensities and widths to those observed around 29 GHz were found. It was readily confirmed that the spectral carrier is SiC_2N, from the following facts: (i) the observed transition frequencies of the two transitions agree well with those calculated, (ii) each transition has three hyperfine components due to the nitrogen nucleus, (iii) the lines exhibit the paramagnetic behavior. Finally, a total of 12 lines composed of four rotational transitions each split into three hyperfine components were observed in the region from 13 to 29 GHz. All the observed transition frequencies are listed in Table 4.3.

The following experimental evidences provide further support for our identification: (i) the observed lines disappeared in the absence of electric discharge, (ii) the lines disappeared when a CH_3CN / Ar mixture was used, (iii) the lines were also observed when $SiCl_4$ was replaced by phenylsilane, where the line intensity, however, was about 20% weaker than that observed using the $SiCl_4$ / CH_3CN / Ar mixture, (iv) no isotope shift was observed when

CH_3CN was replaced by CD_3CN.

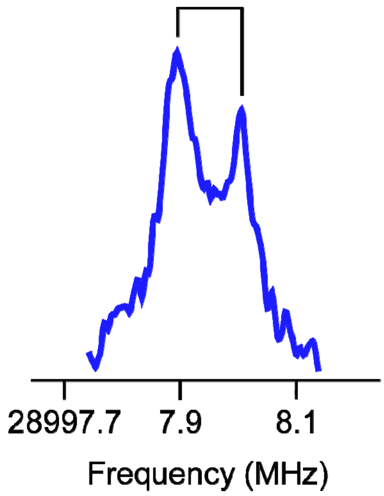

Figure 4.2. The FTMW spectrum of the $J = 5.5-4.5$, $F = 6.5-5.5$ transition of SiC_2N. Since the PDN was arranged parallel to the cavity, the Doppler-doubling was observed. The spectrum was obtained by accumulating 1500 shots at a repetition rate of 10 Hz.

Table 4.3. Observed transition frequencies of SiC_2N in the $\tilde{X}\ ^2\Pi_{3/2}$ state.

J'	F'	J''	F''	Obs. (MHz)	Obs. − Calc. (kHz)
2.5	3.5	1.5	2.5	13178.328	5
2.5	2.5	1.5	1.5	13184.558	2
2.5	1.5	1.5	0.5	13190.096	2
3.5	4.5	2.5	3.5	18452.110	−1
3.5	3.5	2.5	2.5	18454.860	3
3.5	2.5	2.5	1.5	18457.230	−4
4.5	5.5	3.5	4.5	23725.178	−4
4.5	4.5	3.5	3.5	23726.729	−4
4.5	3.5	3.5	2.5	23728.099	0
5.5	6.5	4.5	5.5	28997.956	1
5.5	5.5	4.5	4.5	28998.952	0
5.5	4.5	4.5	3.5	28999.847	3

SiC_3N

We searched the J = 6.5−5.5 transition, predicted at 18.39 GHz from the scaled B constant, 1415 MHz. Two transitions each split into three hyperfine components were observed at 18.380 and 18.389 GHz, respectively. By analogy with SiC_4H, whose rotational spectrum shows Λ-doublings with a separation of ~8 MHz,[17] the observed two transitions were assigned to a Λ-doubling pair of the J = 6.5−5.5 transition of SiC_3N. Subsequently, two transitions each split into three hyperfine components were observed around 15.56 GHz with a separation of ~9 MHz. They were readily assigned to the J = 5.5−4.5 transition of SiC_3N. The observed spectrum of J = 5.5−4.5 is shown in Fig. 4.3. The observed line intensity of SiC_3N is almost the same as that of SiC_2N. In contrast to SiC_2N, lines of SiC_3N show sharp profiles due to its very small magnetic g-factor in the $\tilde{X}\ ^2\Pi_{1/2}$ state. This difference in the magnetic g-factor between SiC_2N and SiC_3N is explained as follows. The Zeeman Hamiltonian $\mathbf{H}_Z$ is written as the sum of four terms:

$$\mathbf{H}_Z = g_L \mu_B \mathbf{B}\cdot\mathbf{L} + g_S \mu_B \mathbf{B}\cdot\mathbf{S} - g_N \mu_N \mathbf{B}\cdot\mathbf{I} - g_r \mu_B (\mathbf{J}-\mathbf{L}-\mathbf{S})\cdot\mathbf{B}, \tag{4.11}$$

where g_L and g_S are the orbital and spin g-factors, respectively, g_N is the g-factor for nucleus considered, g_r is the nuclear rotational g-factor, $\mathbf{B}$ is a static magnetic field. On the assumption of a free electron (g_L = 1) and a good case (a) molecule, an effective magnetic g-factor for a rotational level J is written by

$$g_J = \frac{(\Lambda+\Sigma)(\Lambda+g_S\Sigma)}{J(J+1)}. \tag{4.12}$$

Putting g_S = 2, the g-factor for the $^2\Pi_{1/2}$ state is calculated to be zero. Hence, the good case (a) molecules in the $^2\Pi_{1/2}$ states are less susceptible to an external magnetic field than those in the $^2\Pi_{3/2}$ states.

The MW-MW double-resonance technique was utilized to observe ΔF = 0 lines of the J = 2.5−1.5 transition. Figure 4.4 shows the observed double-resonance spectrum of the J = 2.5−1.5 (e), F = 2.5−2.5 transition. In the measurement, the J = 3.5−2.5 (e), F = 3.5−2.5 transition, which shares the upper level of the ΔF = 0 transition, was monitored. Scan step was 3 kHz and the monitored FID signal was recorded by averaging 100 discharge shots at a repetition rate of 10 Hz at each step. Five to eight spectra thus measured were averaged afterwards to obtain a spectrum with a higher signal-to-noise ratio. In order to suppress the power broadening as much as possible, the power of the pumping radiation was reduced so that the depletion of the monitored signal does not exceed 50%. The pump radiation was irradiated after the polarization MW pulse to avoid the competition between the two processes causing the change of the monitored signal; the coherence change and the population change (see Chapter 2). In this way, four ΔF = 0 lines of the J = 2.5−1.5 transition were observed by the MW-MW double-resonance technique. Eventually, a total of 50 lines were observed by FTMW spectroscopy and the double-resonance technique in the region from 7 to 27 GHz. The measured transition frequencies are listed in Table 4.4. They were very close to those predicted, supporting our identification of the spectral carrier. Since all the transitions appeared at frequencies of odd multiples of B_{eff}, ~1415 MHz, it was concluded that the observed lines, which show almost no Zeeman effect, are originating from a radical species in a $^2\Pi$ electronic state.

Other experimental evidences for our identification of the carrier molecule are: (i) the observed lines disappeared in the absence of electric discharge, (ii) the lines disappeared when CCl_4 was used instead of $SiCl_4$, (iii) the same lines were observed when $SiCl_4$ was replaced by phenylsilane, where the line intensity was almost the same as that obtained using the $SiCl_4$ / CH_3CN / Ar mixture.

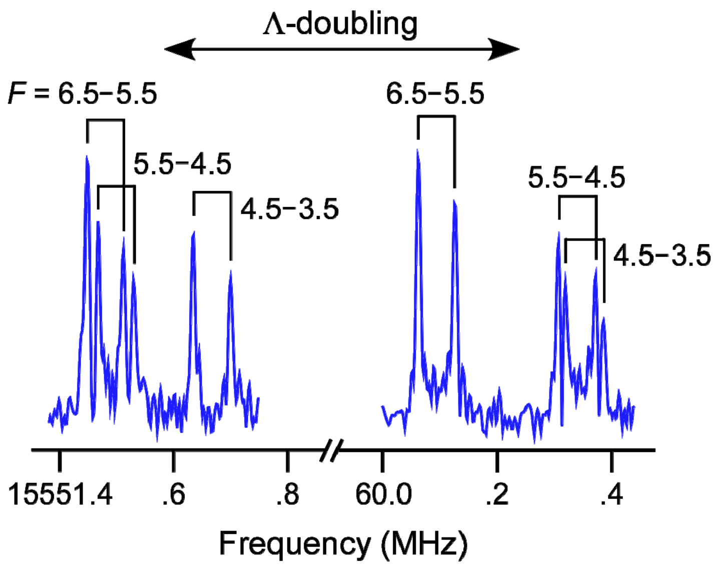

Figure 4.3. The FTMW spectrum of the $J = 5.5{-}4.5$ transition of SiC_3N. Since the PDN was arranged parallel to the cavity, the Doppler-doublings were observed. The spectrum was obtained by accumulating 2500 shots at a repetition rate of 10 Hz.

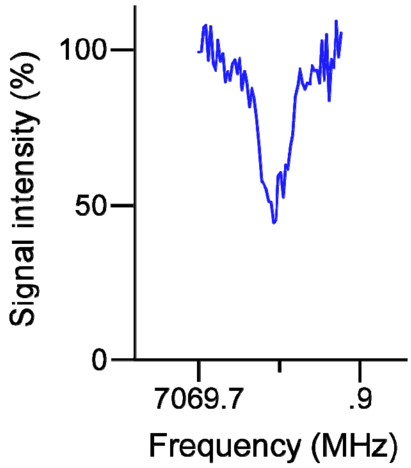

Figure 4.4. The MW-MW double-resonance spectrum of the J = 2.5−1.5 (e), F = 2.5−2.5 transition of SiC_3N. The vertical axis corresponds to the signal intensity of the monitored transition, J = 3.5−2.5 (e), F = 3.5−2.5.

Table 4.4. Observed transition frequencies of SiC_3N in the $\tilde{X}\ ^2\Pi_{1/2}$ state.

J'	F'	J''	F''	Parity	Obs. (MHz)	Obs. − Calc. (kHz)
2.5	3.5	1.5	2.5	*e*	7065.939	−3
2.5	2.5	1.5	1.5	*e*	7066.073	4
2.5	3.5	1.5	2.5	*f*	7075.044	−2
2.5	2.5	1.5	1.5	*f*	7076.677	4
2.5	2.5	1.5	2.5	*e*	7069.794[a]	−1
2.5	1.5	1.5	1.5	*e*	7071.568[a]	5
2.5	2.5	1.5	2.5	*f*	7065.360[a]	4
2.5	1.5	1.5	1.5	*f*	7072.471[a]	−2
3.5	4.5	2.5	3.5	*e*	9894.593	−2
3.5	3.5	2.5	2.5	*e*	9894.649	1
3.5	2.5	2.5	1.5	*e*	9895.035	1
3.5	4.5	2.5	3.5	*f*	9903.413	0
3.5	3.5	2.5	2.5	*f*	9904.109	1
3.5	2.5	2.5	1.5	*f*	9904.139	−1
4.5	5.5	3.5	4.5	*e*	12723.073	−1
4.5	4.5	3.5	3.5	*e*	12723.103	−1
4.5	3.5	3.5	2.5	*e*	12723.348	−1
4.5	5.5	3.5	4.5	*f*	12731.760	−1
4.5	4.5	3.5	3.5	*f*	12732.145	−2
4.5	3.5	3.5	2.5	*f*	12732.165	−1
5.5	6.5	4.5	5.5	*e*	15551.482	−1
5.5	5.5	4.5	4.5	*e*	15551.501	0
5.5	4.5	4.5	3.5	*e*	15551.669	−1
5.5	6.5	4.5	5.5	*f*	15560.097	0
5.5	5.5	4.5	4.5	*f*	15560.341	−1
5.5	4.5	4.5	3.5	*f*	15560.355	1

(*Continued.*)

J'	F'	J''	F''	Parity	Obs. (MHz)	Obs. − Calc. (kHz)
6.5	7.5	5.5	6.5	*e*	18379.854	0
6.5	6.5	5.5	5.5	*e*	18379.868	2
6.5	5.5	5.5	4.5	*e*	18379.990	0
6.5	7.5	5.5	6.5	*f*	18388.424	1
6.5	6.5	5.5	5.5	*f*	18388.592	0
6.5	5.5	5.5	4.5	*f*	18388.602	2
7.5	8.5	6.5	7.5	*e*	21208.198	−1
7.5	7.5	6.5	6.5	*e*	21208.211	3
7.5	6.5	6.5	5.5	*e*	21208.301	−2
7.5	8.5	6.5	7.5	*f*	21216.738	0
7.5	7.5	6.5	6.5	*f*	21216.864[b]	2
7.5	6.5	6.5	5.5	*f*	21216.864[b]	−4
8.5	9.5	7.5	8.5	*e*	24036.530[b]	4
8.5	8.5	7.5	7.5	*e*	24036.530[b]	−2
8.5	7.5	7.5	6.5	*e*	24036.603	−3
8.5	9.5	7.5	8.5	*f*	24045.042	−1
8.5	8.5	7.5	7.5	*f*	24045.139[b]	3
8.5	7.5	7.5	6.5	*f*	24045.139[b]	−2
9.5	10.5	8.5	9.5	*e*	26864.838[b]	3
9.5	9.5	8.5	8.5	*e*	26864.838[b]	−1
9.5	8.5	8.5	7.5	*e*	26864.898	−1
9.5	10.5	8.5	9.5	*f*	26873.336	2
9.5	9.5	8.5	8.5	*f*	26873.408[b]	1
9.5	8.5	8.5	7.5	*f*	26873.408[b]	−3

[a]Measured by the MW-MW double-resonance technique.

[b]Unresolved.

4.5 Analysis

The observed transition frequencies of SiC_2N and SiC_3N were analyzed using an effective Hamiltonian for $^2\Pi$ electronic states including the hyperfine interaction. The explicit form of the Hamiltonian and its matrix elements are given in Appendix III. The molecular constants determined by the least-squares fittings are listed in Table 4.5. Since the A_{so} values are unable to be determined from the present data, they were fixed to the theoretical values. The Λ-doubling constant of SiC_2N was assumed to be zero because the doubling was not resolved in the present measurement. The $a-(b+c)/2$ and d constants of SiC_2N were fixed to zero because these constants describe the hyperfine interaction mainly in the $^2\Pi_{1/2}$ state (see Eqs. (A-III.16,18)) for which no data has been obtained. Similarly, for SiC_3N, the $a+(b+c)/2$ constant, which mainly contributes the hyperfine coupling in the $^2\Pi_{3/2}$ state (see Eq. (A-III.16)), was assumed to be zero owing to the lack of data for the spin sub-level. The assignment of the Λ-doubling components for SiC_3N was made for the d constant to be positive in accordance with its definition. The b constant should be included in the fits to reproduce the observed line positions for both of the radicals. Analyses including the b constant reduced the standard deviations of the fits from 12.0 to 3.8 kHz and 2.8 to 2.2 kHz for SiC_2N and SiC_3N, respectively. In order to determine $a-(b+c)/2$ and eQq_0 simultaneously for SiC_3N, at least one $\Delta F = 0$ line of the $J = 2.5-1.5$ transition must be included in the fit.

4.6 Discussion

The magnetic hyperfine constants describing the interactions in the $\Omega = 3/2$ and 1/2 spin sub-levels were determined for SiC_2N and SiC_3N, showing that they have the $^2\Pi_i$ and $^2\Pi_r$ ground electronic states, respectively. This is confirmed from the fact that almost no Zeeman effect was observed for the lines of SiC_3N, which is a typical behavior for a molecule in a $^2\Pi_{1/2}$ state. Furthermore, since SiCN has the $^2\Pi_r$ ground electronic state, it is presumed that the SiC_nN series with odd and even n have $^2\Pi_r$ and $^2\Pi_i$ ground electronic

Table 4.5. Molecular constants of SiC_2N and SiC_3N (in MHz).

	SiC_2N ($\tilde{X}\,^2\Pi_i$)		SiC_3N ($\tilde{X}\,^2\Pi_r$)	
	Expt.[a]	Theory	Expt.[a]	Theory
A_{so} (cm^{-1})	−66.8(fixed)	−66.8[b]	118.3(fixed)	118.3[b]
B	2639.72807(46)	2637.7[c,d]	1414.740120(66)	1415.0[c,d]
		2617.5[c]		1398.8[c]
$D \times 10^6$	233.6(93)	⋯	58.31(49)	⋯
$p + 2q$	⋯	⋯	8.4647(12)	⋯
$(p + 2q)_D \times 10^6$	⋯	⋯	−81.5(77)	⋯
$a+(b+c)/2$	18.978(13)	13.51[e]		
$a-(b+c)/2$			8.4647(12)	11.34[e]
b	13.9(16)	7.74[e]	3.97(81)	0.31[e]
d			11.2959(25)	10.09[e]
eQq_0	−4.1362(94)	−4.25[f]	−4.2532(34)	−4.46[f]
σ_{fit} (kHz)	3.8		2.2	

[a]Values in parentheses denote 1σ errors and apply to the last digits.

[b]MRCI/cc-pVQZ.

[c]RCCSD(T)/cc-pVQZ.

[d]Scaled by multiplying $B^{\mathrm{Expt.}}/B^{\mathrm{Calc.}}$ of the isoelectronic radical, $SiC_{n+1}H$.

[e]Estimated using Eqs. (4.6) to (4.8) and (4.10), see text for details.

[f]QCISD/cc-pVTZ.

states, respectively, as is the case for the $SiC_{n+1}H$ series.

The determined rotational constants of SiC_2N and SiC_3N agree well even with the non-scaled theoretical B constants, indicating the *ab initio* geometries presented in Fig. 4.1 are fairly accurate. The experimentally determined centrifugal distortion constants D and the Λ-doubling constants of SiC_2N and SiC_3N are compared with those of SiC_3H[18] and SiC_4H[17] in Table 4.6. The D constants of SiC_2N and SiC_3N, and the Λ-doubling constants of SiC_3N are very close to those of the corresponding isoelectronic radicals. The similar values for the Λ-doubling constants between SiC_3N and SiC_4H are expected by the pure-precession hypothesis. According to the hypothesis, the constants p and q are related to the rotational constant B, the spin-orbit interaction constant A_{so}, and the energy difference between the $^2\Pi$ and $^2\Sigma^+$ states that are interacting with each other through the spin-orbit and rotational electronic Coriolis interactions:

$$p = \frac{4BA_{so}}{E\left(^2\Sigma^+\right) - E\left(^2\Pi\right)}, \tag{4.13}$$

$$q = -\frac{4B^2}{E\left(^2\Sigma^+\right) - E\left(^2\Pi\right)}. \tag{4.14}$$

These expressions mean that p and q are proportional to $B \times A_{so}$ and B^2, respectively. In general, molecules isoelectronic to each other have similar electronic structures, that is, the energy differences $E\left(^2\Sigma^+\right) - E\left(^2\Pi\right)$ may be close to each other. Furthermore, as listed in Table 4.7, B and A_{so} have similar values between SiC_3N and SiC_4H. Hence, the similar values for the Λ-doubling constants of SiC_3N and SiC_4H presented in Table 4.6 are fairly

Table 4.6. Comparison of the centrifugal distortion constants and the Λ-doubling constants of SiC_2N and SiC_3N with those of the $SiC_{n+1}H$ radicals (in MHz).

	$\tilde{X}\,^2\Pi_{3/2}$		$\tilde{X}\,^2\Pi_{1/2}$	
	SiC_2N	SiC_3H[a]	SiC_3N	SiC_4H[b]
$D \times 10^6$	234	209	58	56
$p + 2q$	⋯	⋯	8.5	8.4
$(p + 2q)_D \times 10^6$	⋯	⋯	−81	−102
q	Unresolved	−0.09	⋯	⋯

[a]Reference 18.

[b]Reference 17.

Table 4.7. Comparison of A_{so} and B of SiC_2N and SiC_3N with those of the $SiC_{n+1}H$ radicals (in MHz).

	$\tilde{X}\,^2\Pi_{3/2}$		$\tilde{X}\,^2\Pi_{1/2}$	
	SiC_2N	SiC_3H	SiC_3N	SiC_4H
A_{so} (cm^{-1})	−64[a]	−66[b]	118[a]	114[a]
B	2640[c]	2605[b]	1415[c]	1416[d]

[a]MRCI/cc-pVQZ.

[b]Experimental value, see Chapter 5.

[c]Present study.

[d]Experimental value cited from Ref. 17.

reasonable results. For the same reason, the Λ-doubling constant q of SiC_2N may have a very small value as is the case for SiC_3H, although it was not determined in the present experiment.

The magnetic hyperfine constants of the radicals are in reasonable agreement with those predicted from the QCISD/cc-pVTZ calculations, as shown in Table 4.5. The electric quadrupole coupling constants eQq_0 agree even better with those predicted at the same level of theory. The dependence of the magnetic hyperfine constants on the chain length for the SiC_nN radicals with n = 1[16] and 3 is shown in Fig. 4.5. The hyperfine constants of the isovalent radicals, C_2N,[19] C_4N,[21] and C_6N,[21] are also plotted in the same figure. As seen in Fig. 4.5, for the two series of radicals, all the constants decrease about 50% when one C_2 unit is added to the chain. This indicates the increase of the delocalization of the unpaired electron along the chain, since magnetic hyperfine constants are proportional to $\langle 1/r^3 \rangle$, where r is the distance of the unpaired electron from the nucleus considered. The experimental data for SiC_4N is required for a similar discussion for the even number of carbon series.

The spin density on the N atom for SiC_2N and SiC_3N was estimated, using the experimentally determined magnetic hyperfine constants. In the present study, however, the complete sets of the four constants were not available because of the lack of either $a+(b+c)/2$ or $a-(b+c)/2$. Several approximations were thus made to estimate a constants from the determined magnetic hyperfine constants. For SiC_3N, using the experimental values for $a-(b+c)/2$, b, and d, and Eq. (4.9), the a constant was estimated to be 13.4 MHz. The spin density on the N atom of SiC_3N was estimated to be ~10% by comparing the a constant with $g_S g_N \mu_B \mu_N \langle r^{-3} \rangle$ of the N atom, 138.8 MHz,[31] where g_S is approximated to be 2 to compare it with a. For SiC_2N, because of the lack of the experimental d constant, it was necessary to utilize a ratio of $-a/c$ to be $5/3$, instead of Eq. (4.9). This ratio is derived on the assumption that the unpaired electron occupies the pure p_π orbital. As shown in Eq. (A-III.24), the c constant is proportional to the integral $\langle \Lambda = 1 | (3\cos^2\theta - 1)/r^3 | \Lambda = 1 \rangle$. The angular part of the integral is approximated to be $-2/5$,

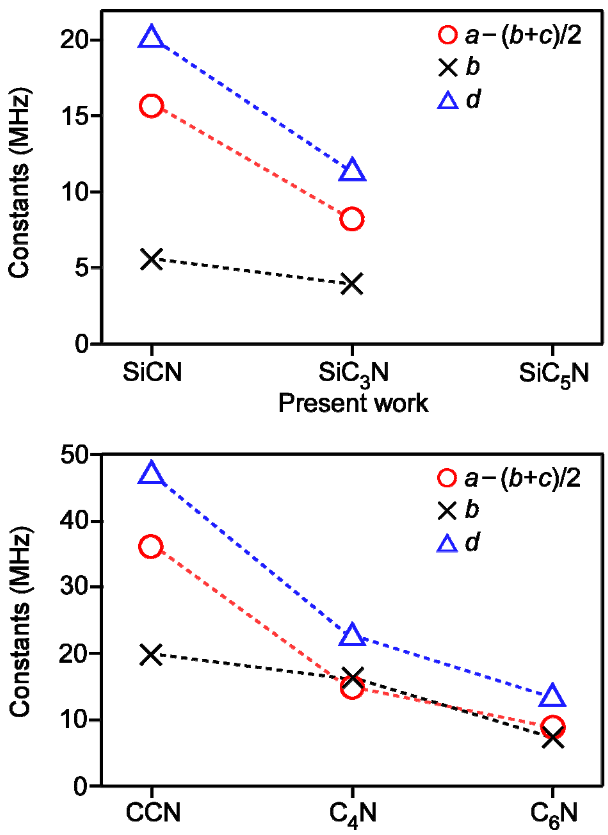

Figure 4.5. The chain length dependence of the magnetic hyperfine constants for the SiC_nN radicals with odd n and their isovalent radicals $C_{n+1}N$.

on the assumption of the the pure p_π orbital, giving the ratio $-a/c$ of $5/3$. Using this ratio and the experimental d constant, the a constant was estimated to be 17.8 MHz, yielding the spin density on the N atom to be ~13%. Figure 4.6 shows the calculated singly occupied molecular orbitals (SOMO) of SiC_2N and SiC_3N for comparison.

An electronic spectrum of the $\tilde{A}\,^2\Sigma^+ - \tilde{X}\,^2\Pi_{3/2}$ transition of SiC_2N was searched by LIF spectroscopy in the region from 13000 to 16400 cm^{-1}, based on the excitation energy calculated at the MRCI/cc-pVQZ level of theory, ~14000 cm^{-1}. The LIF spectrum of the radical, however, was not observed by our apparatus, although the $\tilde{A} - \tilde{X}$ transition of SiC_3H (Chapter 5) has already been observed by LIF spectroscopy around the same energy region.[18] An LIF spectroscopic study for SiC_3N has not been attempted.

The molecular constants have been determined precisely for SiC_2N and SiC_3N in the present work. Using the experimentally determined constants presented in Table 4.5, transition frequencies in the millimeter-wave region were predicted for SiC_2N and SiC_3N. The predicted transition frequencies are summarized in Appendix IV. The frequencies were compared with available line survey data toward IRC+10216 listed in Table 4.8.[32–34] No lines, however, correspond to the reported unidentified lines. Astronomical searches for these two radicals using highly sensitive telescopes such as ALMA may be desired.

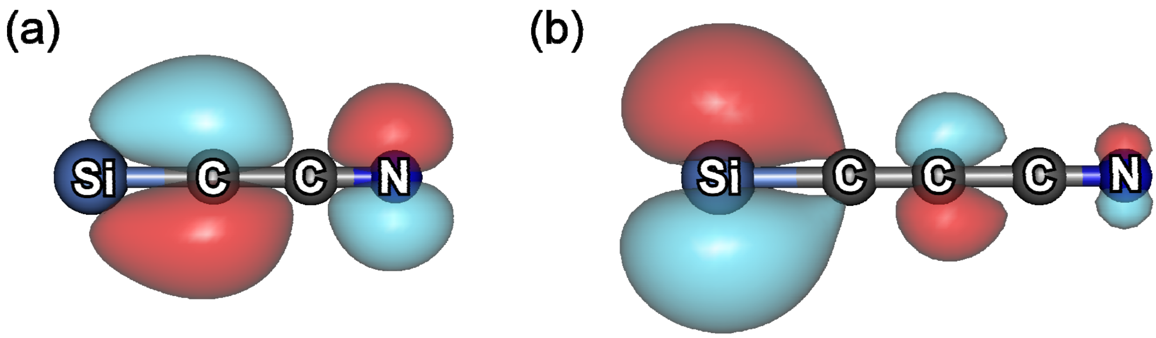

Figure 4.6. Calculated SOMO of (a) SiC_2N and (b) SiC_3N.

Table 4.8. Line survey data referred to in the present study.

Frequency region (GHz)	Telescope	Reference
28−50	Nobeyama 45-m	32
130−170	IRAM 30-m	33
130−170	KP 12-m	34
220−270	HHT 10-m	34

References

[1]R. W. Wilson, A. A. Penzias, K. B. Jefferts, M. Kutner, and P. Thaddeus, Astrophys. J. **167**, L97 (1971).

[2]M. Morris, W. Gilmore, P. Palmer, B. E. Turner, and B. Zuckerman, Astrophys. J. **199**, L47 (1975).

[3]B. E. Turner, Astrophys. J. **388**, L35 (1992).

[4]J. Cernicharo, C. A. Gottlieb, M. Guélin, P. Thaddeus, and J. M. Vrtilek, Astrophys. J. **341**, L25 (1989).

[5]P. Thaddeus, S. E. Cummins, and R. A. Linke, Astrophys. J. **283**, L45 (1984).

[6]A. J. Apponi, M. C. McCarthy, C. A. Gottlieb, and P. Thaddeus, Astrophys. J. **516**, L103 (1999).

[7]M. Ohishi, N. Kaifu, K. Kawaguchi, A. Murakami, S. Saito, S. Yamamoto, S. Ishikawa, Y. Fujita, Y. Shiratori, and W. M. Irvine, Astrophys. J. **345**, L83 (1989).

[8]M. Guélin, S. Muller, J. Cernicharo, A. J. Apponi, M. C. McCarthy, C. A. Gottlieb, and P. Thaddeus, Astron. Astrophys. **363**, L9 (2000).

[9]M. Guélin, S. Muller, J. Cernicharo, M. C. McCarthy, and P. Thaddeus, Astron. Astrophys. **426**, L49 (2004).

[10]A. McKellar, Publ. Astron. Soc. Pac. **52**, 312 (1940).

[11]J. K. Anderson and L. M. Ziurys, Astrophys. J. **795**, L1 (2014).

[12]M. Guélin and P. Thaddeus, Astrophys. J. **212**, L81 (1977).

[13]M. Guélin, N. Neininger, and J. Cernicharo, Astron. Astrophys. **335**, L1 (1998).

[14]T. C. Smith, H. Li, and D. J. Clouthier, J. Am. Chem. Soc. **121**, 6068 (1999).

[15]T. C. Smith, H. Li, D. J. Clouthier, C. T. Kingston, and A. J. Merer, J. Chem. Phys. **112**, 3662 (2000).

[16]A. J. Apponi, M. C. McCarthy, C. A. Gottlieb, and P. Thaddeus, Astrophys. J. **536**, L55 (2000).

[17]M. C. McCarthy, A. J. Apponi, C. A. Gottlieb, and P. Thaddeus, J. Chem. Phys. **115**, 870 (2001).

[18]D. L. Kokkin, N. J. Reilly, R. C. Fortenberry, T. D. Crawford, and M. C. McCarthy, J. Chem.

Phys. **141**, 044310 (2014).

[19]Y. Ohshima and Y. Endo, J. Mol. Spec. **172**, 225 (1995).

[20]C. A. Gottlieb, E. W. Gottlieb, P. Thaddeus, and H. Kawamura, Astrophys. J. **275**, 916 (1983).

[21]M. C. McCarthy, G. W. Fuchs, J. Kucera, G. Winnewisser, and P. Thaddeus, J. Chem. Phys. **118**, 3549 (2003).

[22]Y. Kasai, Y. Sumiyoshi, Y. Endo, and K. Kawaguchi, Astrophys. J. **477**, L65 (1997).

[23]G. Maier, H. P. Reisenauer, H. Egenolf, and J. Glatthaar, Eur. J. Org. Chem. **1998**, 1307 (1998).

[24]M. Fukushima and T. Ishiwata, J. Phys. Chem. A **117**, 9435 (2013).

[25]Y. H. Ding, Z. S. Li, X. R. Huang, and C. C. Sun, J. Phys. Chem. A **105**, 5896 (2001).

[26]H. L. Liu, X. R. Huang, G. H. Chen, Y. H. Ding, and C. C. Sun, J. Phys. Chem. A **108**, 6919 (2004).

[27]R. A. Frosch and H. M. Foley, Phys. Rev. **88**, 1337 (1952).

[28]C. H. Townes and A. L. Schawlow, *Microwave Spectroscopy* (Dover, New York, 1975) p. 245.

[29]M. J. Frisch, G. W. Trucks, and H. B. Schlegel *et al*., GAUSSIAN, Revision E.01, Gaussian, Inc., Pittsburgh, PA, 2003.

[30]H.-J. Werner, P. J. Knowles, F. R. Manby, M. Schütz *et al*., MOLPRO, version 2012.1, a package of *ab initio* programs, 2012, see http://www.molpro.net.

[31]J. R. Morton and K. F. Preston, J. Magn. Res. **30**, 577 (1978).

[32]K. Kawaguchi, Y. Kasai, S. Ishikawa, and N. Kaifu, Publ. Astron. Soc. Japan **47**, 853 (1995).

[33]J. Cernicharo, M. Guélin and C. Kahane, Astron. Astrophys. Suppl. **142**, 181 (2000).

[34]J. H. He, D-V-Trung, S. Kwok, H. S. P. Müller, Y. Zhang, T. Hasegawa, T. C. Peng, and Y. C. Huang, Astrophys. J. Suppl. Ser. **177**, 275 (2008).

Chapter 5
Laser Spectroscopy of the $\tilde{A}^2\Sigma^+ \leftarrow \tilde{X}^2\Pi_i$ Transition of SiC_3H

5.1 Introduction

The SiC_3H radical is a member of silicon and hydrogen terminated carbon chain radicals SiC_nH. This series of radicals have attracted interest in astrochemistry, because silicon and carbon have high cosmic abundances and many hydrogen terminated carbon chain radicals C_nH have been detected in interstellar media. For this reason, laboratory detections of the SiC_nH radicals have been attempted, and several members, n = 2−6, have been identified by Fourier transform microwave (FTMW) spectroscopy.[1−3] From the microwave spectroscopic study,[3] it was clarified that SiC_3H has the $^2\Pi_i$ ground electronic state whereas its isovalent radicals C_4H[4] and C_3N[5] have the $^2\Sigma^+$ ground electronic states.

Electronic spectra of the SiC_nH radicals have also been reported. The shortest member, SiCH, was the first subject to the optical spectroscopic studies.[6−10] It was revealed that SiCH has the $\tilde{A}^2\Sigma^+ - \tilde{X}^2\Pi_i$ system in the region from 11800−16600 cm^{-1}. This is not the case for its isovalent radical C_2H,[11] in which the $^2\Sigma^+$ state is lower in energy than the $^2\Pi_i$ state. Very recently, Kokkin *et al.* observed optical spectra of jet-cooled SiC_nH (n = 3−5) by resonant two-color ionization (R2PI) and laser induced fluorescence (LIF) spectroscopy.[3] In their studies, the electronic excitation spectrum of SiC_3H was observed in the region from 14700−16500 cm^{-1}. The observed spectrum was assigned to the $\tilde{A}^2\Sigma^+ - \tilde{X}^2\Pi_i$ transition based on the *ab initio* adiabatic transition energy of 16450 cm^{-1}. A total of 27 vibronic bands were observed in the excitation spectrum. Vibrational assignments were made for the prominent 19 features on the basis of the theoretical vibrational frequencies, giving experimental frequencies for the $\tilde{A}$ state: ν_3 (C_1−C_2 stretch) = 1492 cm^{-1}, ν_4 (Si−C_1 stretch) = 672 cm^{-1}, ν_5 (C_2−C_3−H bend) = 723 cm^{-1}, ν_6 (C_1−C_2−C_3 bend) = 483 cm^{-1} and ν_7 (Si−C_1−C_2 bend) = 197 cm^{-1}. In addition to the excitation spectra, Kokkin *et al.* observed dispersed fluorescence (DF) spectra from the 0^0, 6^1, 7^1 levels. Although no detailed Renner-Teller analysis was attempted for the observed DF spectra, prominent features were tentatively assigned to vibrational levels associated with ν_4, ν_6, and ν_7 modes, and the experimental frequency of ν_4 mode for the $\tilde{X}$ state was determined to be 627 cm^{-1}. In the DF spectrum, the transition terminating to the 0_0 ($^2\Pi_{1/2}$) level was also observed, and the A_{so} value was determined to be −64 cm^{-1}.

As mentioned above, the vibrational structures of SiC_3H in both the electronic states have been investigated. Rotationally-resolved spectra for the $\tilde{A}-\tilde{X}$ band system, however, have not been measured yet. High-resolution spectral measurements were beyond the resolutions of the R2PI and LIF spectroscopic systems utilized by Kokkin *et al.* Rotational analyses of high-resolution spectra enable us to determine the rotational constants of the molecule and band types of the observed transitions. The experimentally determined rotational constants give information on the molecular geometry of the spectral career. Furthermore, the determined band types support the vibrational assignments of the observed bands.

In the present study, we report rotationally-resolved LIF spectra of the 0_0^0, 4_0^1, and $6_0^1 7_0^1$ bands of the SiC_3H $\tilde{A}-\tilde{X}$ transition. Prior to the high-resolution LIF spectroscopic studies, a low-resolution LIF excitation spectrum of the band system was re-measured. Because several bands previously reported[3] were masked by C_2 Swan and $d\,^3\Pi_g - c\,^3\Sigma_u^+$ bands, fluorescence depletion (FD) spectroscopy was also applied to the band system. The determined rotational constants of the 0_0^0, 4_0^1, and $6_0^1 7_0^1$ bands have strongly suggested that these three bands are originating from *l*-SiC_3H. Moreover, it has been revealed that the upper states of these three vibronic bands have Σ^+ symmetry. The DF spectrum from the 0^0 level was also observed with a higher signal-to-noise ratio, and the ν_3 band has been newly identified in the $\tilde{X}$ state.

5.2 *Ab initio* calculation

All calculations were performed by the multi-reference configuration interaction method with Davidson correction (MRCI+Q) using Dunning's correlation-consistent polarized valence triple-zeta (cc-pVTZ) basis set. Reference wave functions used in the

MRCI calculation were obtained by the state-averaged complete active space self-consistent field (CASSCF) calculation, where 11 electrons were seeded into 11 valence orbitals (11e,11o) and the three lowest electronic states were averaged. In the MRCI calculation, 9 electrons were seeded into 10 valence orbitals (9e,10o). All the computations were carried out using the MOLPRO 2012.1 package.[12]

Table 5.1 summarizes the calculated geometrical parameters, the spectroscopic constants, the excitation energy T_e ($\tilde{A}-\tilde{X}$), and the transition dipole moment μ ($\tilde{A}-\tilde{X}$). Linear geometries were predicted for both the electronic states, and it was suggested that ν_4 ($Si{-}C_1$ stretch) mode is Franck-Condon active. To support assignments of the observed vibronic levels, harmonic vibrational frequencies of SiC_3H in both the electronic states were calculated. For linear molecules in degenerate electronic states, such as SiC_3H in the $\tilde{X}$ state, the Renner-Teller effect has to be taken into account.[13−15] The bending motion of the

Table 5.1. Predicted geometrical parameters and spectroscopic constants in the $\tilde{X}$ and $\tilde{A}$ states, and the excitation energy and transition dipole moment for the $\tilde{A}-\tilde{X}$ transition.

		$\tilde{X}\,^2\Pi_i$	$\tilde{A}\,^2\Sigma^+$
$Si{-}C_1{-}C_2{-}C_3{-}H$			
$r(Si{-}C_1)$	(Å)	1.714	1.633
$r(C_1{-}C_2)$	(Å)	1.342	1.363
$r(C_2{-}C_3)$	(Å)	1.237	1.224
$r(C_3{-}H)$	(Å)	1.062	1.061
A_{so}	(cm^{-1})	−63.4 (−64 [a])	⋯
B	(cm^{-1})	0.0857 (0.08690 [a])	0.0886
T_e ($\tilde{A}-\tilde{X}$)	(cm^{-1})	14260	
μ ($\tilde{A}-\tilde{X}$)	(D)	0.52	

[a]Experimental value cited from Ref. 3.

molecule splits the degenerate potential function V into two non-degenerate functions $V^{+}(A')$ and $V^{-}(A'')$. For V^{+} and V^{-}, two distinct harmonic vibrational frequencies $\omega^{+}(A')$ and $\omega^{-}(A'')$ are obtained, respectively. By neglecting anharmonicity, $\omega^{+}(A')$ and $\omega^{-}(A'')$ are related to the Renner parameter ε as

$$\varepsilon = \frac{V^{+} - V^{-}}{V^{+} + V^{-}} = \frac{\left(\omega^{+}\right)^{2} - \left(\omega^{-}\right)^{2}}{\left(\omega^{+}\right)^{2} + \left(\omega^{-}\right)^{2}}. \tag{5.1}$$

The experimentally determinable average bending frequency ω^{0} is related to $\omega^{+}(A')$ and $\omega^{-}(A'')$ as

$$\omega^{0} = \sqrt{\frac{1}{2}\left\{\left(\omega^{+}\right)^{2} + \left(\omega^{-}\right)^{2}\right\}}. \tag{5.2}$$

Harmonic frequency calculations by the MRCI method implemented in MOLPRO utilize numerical Hessian for finite displacements in $3N$ cartesian coordinates. The frequency calculations are only possible in C_1 symmetry, and thus they are inapplicable to the calculations of the harmonic bending frequencies $\omega^{+}(A')$ and $\omega^{-}(A'')$ for degenerate states. Therefore, we utilized the **GF** matrix method based on the bending force constants for $V^{+}(A')$ and $V^{-}(A'')$ to derive $\omega^{+}(A')$ and $\omega^{-}(A'')$ for three possible bending modes of SiC_3H. The **GF** matrix was constructed using internal coordinates. A Definition of the internal coordinates for SiC_3H is shown in Fig. 5.1. In terms of the internal coordinates, the non-degenerate bending potential function $V^{\pm}$ is

$$\begin{aligned} V^{\pm} = {} & \tfrac{1}{2} f_{11}^{bend} (\Delta\theta_1)^2 + \tfrac{1}{2} f_{22}^{bend} (\Delta\theta_2)^2 + \tfrac{1}{2} f_{33}^{bend} (\Delta\theta_3)^2 \\ & + f_{12}^{bend} (\Delta\theta_1)(\Delta\theta_2) + f_{13}^{bend} (\Delta\theta_1)(\Delta\theta_3) + f_{23}^{bend} (\Delta\theta_2)(\Delta\theta_3), \end{aligned} \tag{5.3}$$

where f^{bend} denotes bending force constants, f_{12}^{bend} = f_{21}^{bend}, f_{13}^{bend} = f_{31}^{bend}, and f_{23}^{bend} = f_{32}^{bend} by symmetry. The force constants were evaluated from total energy changes associated with displacements of the bending coordinates. We calculated two points for each coordinate in C_s symmetry. The three quadratic force constants f_{11}^{bend}, f_{22}^{bend}, and f_{33}^{bend} were derived by displacing θ_1, θ_2, and θ_3, respectively, by 2 and 4 degrees. The cross terms were obtained by displacing the corresponding two bending coordinates together, by 2 and 4 degrees. The force constant calculations required 12 points of calculations for $V^{+}(A')$ and $V^{-}(A'')$, respectively. The **G** matrix is obtained by **B** and **M** matrices

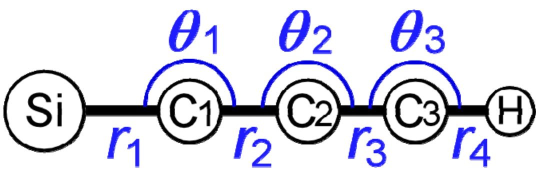

Figure 5.1. Definition of internal coordinates for SiC_3H.

as

$$\mathbf{G} = \mathbf{B}\mathbf{M}^{-1}\mathbf{B}^{t} \tag{5.4}$$

where $\mathbf{M}^{-1}$ is

$$\mathbf{M}^{-1} = \begin{pmatrix} \frac{1}{m_{Si}} & & & & \\ & \frac{1}{m_C} & & & \\ & & \frac{1}{m_C} & & \\ & & & \frac{1}{m_C} & \\ & & & & \frac{1}{m_H} \end{pmatrix}. \tag{5.5}$$

The $\mathbf{B}$ matrix is readily obtained as

$$\mathbf{B} = \begin{array}{c} \\ \Delta\theta_1 \\ \Delta\theta_2 \\ \Delta\theta_3 \end{array} \begin{array}{c} \begin{array}{ccccc} \Delta x_{Si} & \Delta x_{C_1} & \Delta x_{C_2} & \Delta x_{C_3} & \Delta x_H \end{array} \\ \begin{pmatrix} \frac{1}{r(\mathrm{Si-C_1})} & -\frac{1}{r(\mathrm{Si-C_1})}-\frac{1}{r(\mathrm{C_1-C_2})} & \frac{1}{r(\mathrm{C_1-C_2})} & 0 & 0 \\ 0 & \frac{1}{r(\mathrm{C_1-C_2})} & -\frac{1}{r(\mathrm{C_1-C_2})}-\frac{1}{r(\mathrm{C_2-C_3})} & \frac{1}{r(\mathrm{C_2-C_3})} & 0 \\ 0 & 0 & \frac{1}{r(\mathrm{C_2-C_3})} & -\frac{1}{r(\mathrm{C_2-C_3})}-\frac{1}{r(\mathrm{C_3-H})} & \frac{1}{r(\mathrm{C_3-H})} \end{pmatrix} \end{array}, \tag{5.6}$$

where $\Delta\, x$ denotes the cartesian displacement coordinates in the direction perpendicular to the molecular axis. Using Eqs. (5.5) and (5.6), matrix elements of the $\mathbf{G}$ matrix is given by

$$\mathbf{G} = \begin{pmatrix} g_{11} & g_{12} & g_{13} \\ g_{21} & g_{22} & g_{23} \\ g_{31} & g_{32} & g_{33} \end{pmatrix} \tag{5.7}$$

$$g_{11} = \frac{1}{m_{Si}\, r(\mathrm{Si-C_1})^2} + \frac{1}{m_C}\left(-\frac{1}{r(\mathrm{Si-C_1})} - \frac{1}{r(\mathrm{C_1-C_2})}\right)^2 + \frac{1}{m_C\, r(\mathrm{C_1-C_2})^2} \tag{5.8}$$

$$g_{22} = \frac{1}{m_C\, r(\mathrm{C_1-C_2})^2} + \frac{1}{m_C}\left(-\frac{1}{r(\mathrm{C_1-C_2})} - \frac{1}{r(\mathrm{C_2-C_3})}\right)^2 + \frac{1}{m_C\, r(\mathrm{C_2-C_3})^2} \tag{5.9}$$

$$g_{33} = \frac{1}{m_C r(C_2-C_3)^2} + \frac{1}{m_C}\left(-\frac{1}{r(C_2-C_3)} - \frac{1}{r(C_3-H)}\right)^2 + \frac{1}{m_H r(C_3-H)^2} \tag{5.10}$$

$$g_{12} = g_{21} = \frac{1}{m_C r(C_1-C_2)}\left(-\frac{1}{r(Si-C_1)} - \frac{1}{r(C_1-C_2)}\right) + \frac{1}{m_C r(C_1-C_2)}\left(-\frac{1}{r(C_1-C_2)} - \frac{1}{r(C_2-C_3)}\right) \tag{5.11}$$

$$g_{13} = g_{31} = \frac{1}{m_C r(C_1-C_2) r(C_2-C_3)} \tag{5.12}$$

$$g_{23} = g_{32} = \frac{1}{m_C r_3}\left(-\frac{1}{r(C_1-C_2)} - \frac{1}{r(C_2-C_3)}\right) + \frac{1}{m_C r(C_2-C_3)}\left(-\frac{1}{r(C_2-C_3)} - \frac{1}{r(C_3-H)}\right). \tag{5.13}$$

The matrix elements of the $\mathbf{G}$ matrix were calculated using the geometrical parameters of the ground state SiC_3H presented in Table 5.1. By diagonalizing the three-dimensional $\mathbf{GF}$ matrices for $V^+(A')$ and $V^-(A'')$, harmonic vibrational frequencies $\omega^+(A')$ and $\omega^-(A'')$ were obtained for the three bending modes. The bending frequency calculations utilizing the $\mathbf{GF}$ matrix method were also applied to the $\tilde{A}$ state SiC_3H, because it enabled us to save a great deal of time for the calculations in contrast to the original method implemented in MOLPRO. The original frequency calculations using the MRCI method require a total of 60 points of calculations in C_1 symmetry. In contrast, the $\mathbf{GF}$ matrix method needs only 12 points of calculations and it is even possible to calculate in C_s symmetry, which reduces the computation time considerably. The matrix elements of the $\mathbf{G}$ matrix were calculated based on the optimized geometries of the $\tilde{A}$ state SiC_3H presented in Table 5.1. Table 5.2 summarizes calculated force constants f^{bend} and bending vibrational frequencies of SiC_3H in both the electronic states.

Vibrational frequency calculations using the $\mathbf{GF}$ matrix method were also applied to four stretching modes for the $\tilde{X}$ and $\tilde{A}$ states. In terms of the internal coordinates, a stretching potential function V is

$$\begin{aligned} V = {} & \tfrac{1}{2} f_{11}^{str}(\Delta r_1)^2 + \tfrac{1}{2} f_{22}^{str}(\Delta r_2)^2 + \tfrac{1}{2} f_{33}^{str}(\Delta r_3)^2 + \tfrac{1}{2} f_{44}^{str}(\Delta r_4)^2 \\ & + f_{12}^{str}(\Delta r_1)(\Delta r_2) + f_{13}^{str}(\Delta r_1)(\Delta r_3) + f_{14}^{str}(\Delta r_1)(\Delta r_4) \\ & + f_{23}^{str}(\Delta r_2)(\Delta r_3) + f_{24}^{str}(\Delta r_2)(\Delta r_4) + f_{34}^{str}(\Delta r_3)(\Delta r_4), \end{aligned} \tag{5.14}$$

where f^{str} denotes stretching force constants, $f_{12}^{str} = f_{21}^{str}$, $f_{13}^{str} = f_{31}^{str}$, $f_{14}^{str} = f_{41}^{str}$, $f_{23}^{str} = f_{32}^{str}$, $f_{24}^{str} = f_{42}^{str}$ by symmetry. The force constants were evaluated from total

Table 5.2. Calculated force constants and bending vibrational frequencies of SiC_3H in the $\tilde{X}$ and $\tilde{A}$ states.

Parameters	$\tilde{X}\,^2\Pi_i$		$\tilde{A}\,^2\Sigma^+$
	A'	A''	
f_{11}^{bend} (mdyne Å)	0.16415	0.21163	0.34635
f_{22}^{bend} (mdyne Å)	0.33968	0.42489	0.37861
f_{33}^{bend} (mdyne Å)	0.18991	0.10188	0.17372
f_{12}^{bend} (mdyne Å)	0.01428	0.01255	0.00805
f_{13}^{bend} (mdyne Å)	−0.00716	−0.00831	−0.01760
f_{23}^{bend} (mdyne Å)	0.07500	0.11583	0.11105
ω_5^0 (C_2−C_3−H bend) (cm^{-1})	543.3		561.0
ε_5	0.1882		⋯
ω_6^0 (C_1−C_2−C_3 bend) (cm^{-1})	393.3		471.1
ε_6	0.1355		⋯
ω_7^0 (Si−C_1−C_2 bend) (cm^{-1})	157.1		197.4
ε_7	−0.1123		⋯

energy changes associated with the bond lengthening and shortening. Because the symmetry of the molecule is not changed by the displacements, it is possible to use C_{2v} symmetry in the gradient calculations. In MOLPRO, C_{2v} is the highest point group which can be used for molecules belonging to $C_{\infty v}$ point group. The stretching potential function exhibits anharmonicity, that is, the bond lengthening and shortening give two different gradients. Therefore, we averaged the two different gradients obtained by the bond lengthening and shortening. The four quadratic force constants were derived by displacing r_1, r_2, r_3, and r_4, respectively, by ± 0.01 Bohr. The cross terms were obtained by displacing the corresponding two coordinates together in the same direction by ± 0.01 Bohr. The force constant calculations required a total of 20 points of calculations. Using Eq (5.4), the **G** matrix was constructed from the **B** and **M** matrices. The **M** matrix is the same as that given by Eq (5.5). The $\mathbf{B}$ matrix is

$$\mathbf{B} = \begin{array}{c} \\ \Delta r_1 \\ \Delta r_2 \\ \Delta r_3 \\ \Delta r_4 \end{array} \begin{array}{c} \begin{array}{ccccc} \Delta x_{\mathrm{Si}} & \Delta x_{\mathrm{C}_1} & \Delta x_{\mathrm{C}_2} & \Delta x_{\mathrm{C}_3} & \Delta x_{\mathrm{H}} \end{array} \\ \begin{pmatrix} 1 & -1 & 0 & 0 & 0 \\ 0 & 1 & -1 & 0 & 0 \\ 0 & 0 & 1 & -1 & 0 \\ 0 & 0 & 0 & 1 & -1 \end{pmatrix} \end{array}. \quad (5.15)$$

The $\mathbf{G}$ matrix was derived as

$$\mathbf{G} = \begin{pmatrix} \frac{1}{m_{\mathrm{Si}}} + \frac{1}{m_{\mathrm{C}}} & -\frac{1}{m_{\mathrm{C}}} & 0 & 0 \\ -\frac{1}{m_{\mathrm{C}}} & \frac{2}{m_{\mathrm{C}}} & -\frac{1}{m_{\mathrm{C}}} & 0 \\ 0 & -\frac{1}{m_{\mathrm{C}}} & \frac{2}{m_{\mathrm{C}}} & -\frac{1}{m_{\mathrm{C}}} \\ 0 & 0 & -\frac{1}{m_{\mathrm{C}}} & \frac{1}{m_{\mathrm{C}}} + \frac{1}{m_{\mathrm{H}}} \end{pmatrix}. \quad (5.16)$$

Diagonalization of the four-dimensional $\mathbf{GF}$ matrix provided the vibrational frequencies for the four stretching modes. Table 5.3 lists the calculated force constants f^{str} and stretching vibrational frequencies of SiC_3H in both the electronic states.

5.3 Experiment

Since the experimental setup has been described in Chapter 2, only a brief explanation is given here. The SiC_3H radical was produced in a supersonic jet by a pulsed electric discharge of a sample gas mixture, 0.1% $(CH_3)_3SiCCH$ and 0.2% C_2H_2 diluted in Ar. The gas mixture was expanded into a vacuum chamber with a backing pressure of 3 atm. A gas pressure inside the chamber was kept at 1.5×10^{-4} Torr. Synchronized to the gas expansion, a pulsed high voltage of 1400 V with a 10 μs duration was applied between stainless steel electrodes attached to the PDN.

LIF spectroscopy

A dye laser (Lambda Physics Scanmate 2E) pumped by the 2nd harmonic of a Q-switched pulsed Nd:YAG laser (Spectra Physics Lab-170-10) was used as a probe light source. The output beam of the dye laser was irradiated to the supersonic jet at 30 mm

Table 5.3. Calculated force constants and stretching vibrational frequencies of SiC_3H in the $\tilde{X}$ and $\tilde{A}$ states.

Parameters	$\tilde{X}\,^2\Pi_i$	$\tilde{A}\,^2\Sigma^+$
f_{11}^{str} (mdyne Å^{-1})	5.03672	6.76986
f_{22}^{str} (mdyne Å^{-1})	7.43256	7.02610
f_{33}^{str} (mdyne Å^{-1})	13.21719	14.64586
f_{44}^{str} (mdyne Å^{-1})	6.46171	6.47308
f_{12}^{str} (mdyne Å^{-1})	0.15184	0.50475
f_{13}^{str} (mdyne Å^{-1})	−0.12296	−0.33237
f_{14}^{str} (mdyne Å^{-1})	0.00508	0.00175
f_{23}^{str} (mdyne Å^{-1})	1.55506	1.05639
f_{24}^{str} (mdyne Å^{-1})	−0.01060	−0.00073
f_{34}^{str} (mdyne Å^{-1})	−0.11849	−0.11599
ω_1 (C_3–H stretch) (cm^{-1})	3470.3	3478.8
ω_2 (C_2–C_3 stretch) (cm^{-1})	1946.6	2057.4
ω_3 (C_1–C_2 stretch) (cm^{-1})	1412.4	1456.4
ω_4 (Si–C_1 stretch) (cm^{-1})	615.4	671.7

downstream from the PDN. The output energy of the probe laser was kept as low as possible, typically ~0.4 mJ/pulse, to suppress a spectral saturation. Laser induced fluorescence was detected by a photomultiplier tube (PMT) (Hamamatsu R3896) through an appropriate low-pass glass filter. The detected LIF signals were calibrated against the probe laser power at each scan step. Low-resolution LIF spectra were obtained by averaging LIF signals of 10 shots at each scan step with the step interval of 0.005 nm. Rotationally-resolved spectra were obtained by averaging LIF signals of 80 shots at each scan step with the step interval of 0.0005 nm. Dispersed fluorescence (DF) spectrum was measured using a 0.5 m monochromator (Jobin Yvon SPEX 500M). The entrance and exit slits widths were 0.25 mm, and the scan step was 0.1 nm. The PMT was operated in the photon counting mode for the observation of the DF spectrum, where the vertical axis in the observed DF spectrum is proportional to the number of detected photons. The resolution of the DF spectrum was about 10 cm^{-1} (FWHM).

FD spectroscopy

The $\tilde{A}-\tilde{X}$ band system was also observed by fluorescence depletion (FD) spectroscopy to avoid perturbations by emission bands arising from other discharge products such as C_2. Figure 5.2 shows an experimental scheme of FD spectroscopy. In the present study, the origin band of the $\tilde{A}-\tilde{X}$ transition was used as a monitor transition, where the laser frequency for monitoring LIF signals was tuned to the Q_1 stack of the origin band at 676.8 nm. The scan step of the probe laser was 0.005 nm. The output energy of the probe laser was typically ~4 mJ/pulse. In comparison to the LIF spectral measurements, the beam diameters of both the monitor and probe lasers were not expanded by the telescope systems. The probe laser was irradiated 600 ns before the fluorescence monitor laser pulse. The LIF emitted from SiC_3H in the zero-vibrational level of the $\tilde{A}$ state was detected through an interference filter with the center wavelength at 700 nm (FWHM ~10 nm). The interference filter cut off the scattered laser light and emissions of metastable Ar atoms, thus suppressing the fluctuations of the monitored signal.

5.4 Results and Discussion

LIF and FD spectra

Figure 5.3(a) shows low-resolution LIF excitation spectrum of discharge products in the region from 14700−16300 cm^{-1}. As seen in the figure, many vibronic bands originating from products other than SiC_3H, such as C_2, were observed in the LIF spectrum. Figure 5.3(b) shows the FD spectrum of the $\tilde{A}-\tilde{X}$ system of SiC_3H in the same energy region, where the $\tilde{A}-\tilde{X}$ 0_0^0 transition (band [A]) was used as the monitor transition. From this

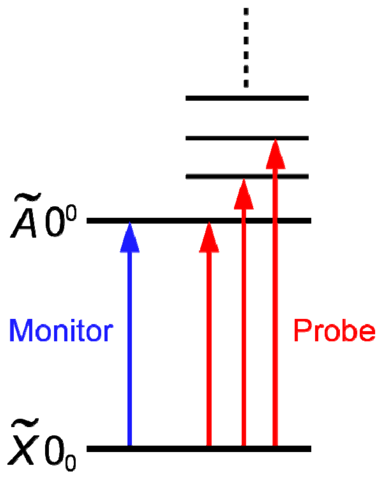

Figure 5.2. Experimental scheme of FD spectroscopy in the present study.

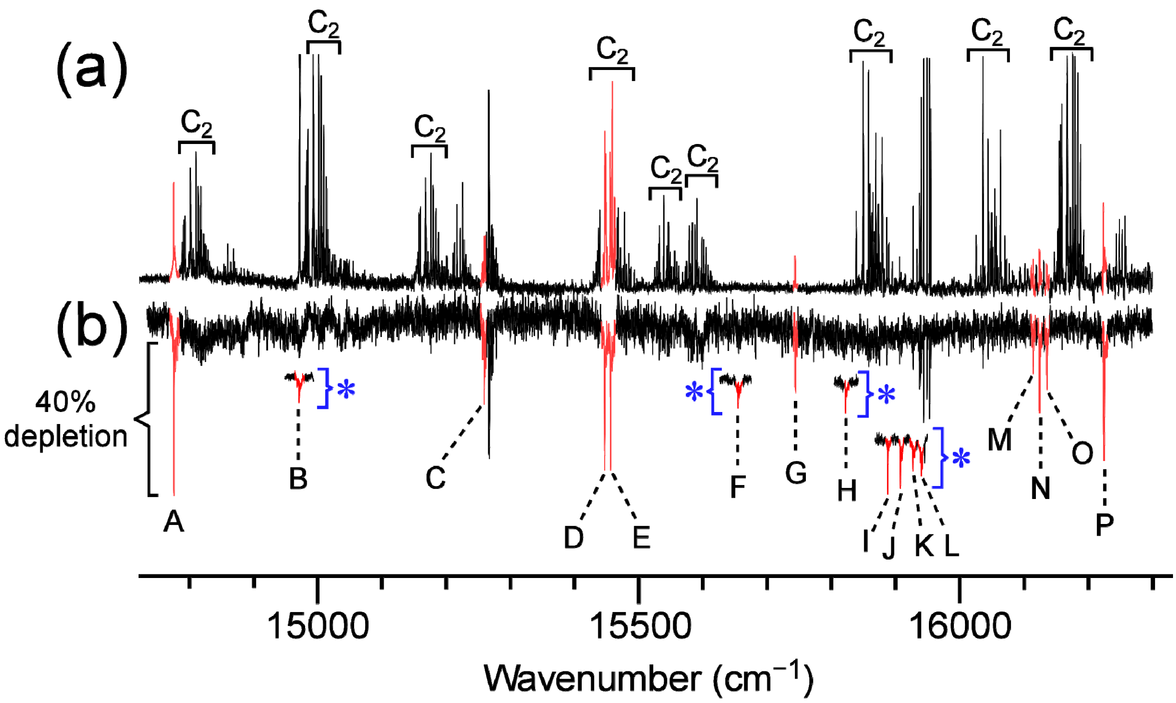

Figure 5.3. (a) Low resolution LIF spectrum obtained by the pulsed discharge of $(CH_3)_3SiCCH$ / C_2H_2 / Ar premix. (b) FD spectrum of the $\tilde{A}-\tilde{X}$ system of SiC_3H in the same energy region. Bands labeled [A] − [P] were assigned to the SiC_3H $\tilde{A}-\tilde{X}$ band system. The spectrum marked with an asterisk was obtained by averaging 15 to 20 observed spectra.

double resonance experiment, it was established that all the observed bands, [A] − [P], are originating from the identical species, SiC_3H, in which bands [H] and [J] had been assigned to transitions of another isomer of SiC_3H.[3] Several bands previously observed by R2PI[3] were not observed in both the spectra possibly because these missing bands have quite low transition intensities. In the R2PI study, the output energy of a probe laser was ~10 mJ/pulse, while in the present study, it was at most ~4 mJ/pulse. Vibrational assignments were made on the basis of the *ab initio* vibrational frequencies presented in Tables 5.2 and 5.3. The assignments are summarized in Table 5.4, along with the observed fluorescence lifetimes and band types determined from the rotationally-resolved LIF study. As shown in Table 5.4, there was no discrepancy between our assignment and that previously reported.[3] The large spectral intensities of the ν_4 progression bands indicate that the ν_4 mode is Franck-Condon active as expected by the predicted molecular geometries for the $\tilde{X}$ and $\tilde{A}$ states presented in Table 5.1. The two vibronic bands observed around 0_0^0 + ~675 cm^{-1} were assigned to the 4_0^1 and $6_0^1 7_0^1$ transitions. The fact that the $6_0^1 7_0^1$ band appears with the similar intensity to that of the Franck-Condon active 4_0^1 band is explained by an intensity borrowing through the Fermi resonance between the two vibronic levels $4^1\ {}^2\Sigma^+$ and $6^1 7^1\ {}^2\Sigma^+$. Fermi resonance is an interaction between accidentally degenerate vibrational levels with the same symmetry. The interaction is due to a cubic anharmonic term, $k_{ijk}\, Q_i Q_j Q_k$, and selection rules for the interaction are $\Delta\upsilon_i = \pm 1$, $\Delta\upsilon_j = \pm 1$, and $\Delta\upsilon_k = \pm 1$. Furthermore, the anharmonic term is totally symmetric, and thus the perturbation occurs only between levels with the same symmetry. The $6^1 7^1$ level with Δ vibronic symmetry is not coupled with the $4^1\ {}^2\Sigma^+$ level, responsible for the missing of $6^1 7^1\ {}^2\Delta$. Three vibrational levels assigned to the mixed states of 4^2, $4^1 6^1 7^1$ and $6^2 7^2$ were also observed at twice the frequency, 0_0^0 + ~1350 cm^{-1}. Table 5.5 lists vibrational frequencies of SiC_3H in the $\tilde{A}$ state estimated from the band positions relative to the 0_0^0 band. The vibrational frequencies estimated from the observed band positions are in excellent agreement with the theoretical harmonic frequencies, indicating the validity of the assignments listed in Table 5.4. The experimental frequency for the ν_5 mode determined by Kokkin *et al.*,[3] however, shows a relatively large difference from our theoretical value,

Table 5.4 Observed vibronic bands of the SiC_3H $\tilde{A}-\tilde{X}$ band system.

	Band position	Relative energy		Assignment		τ
	(cm^{-1})	(cm^{-1})	Band type	This work	Kokkin *et al.* [a]	(ns)
A	14775.98	0	$^2\Sigma^+ - {}^2\Pi$	0_0^0	0_0^0	44
B	14971.29	195	⋯	7_0^1	7_0^1	⋯
	⋯	(415[b])	⋯	⋯	⋯	⋯
	⋯	(462[b])	⋯	⋯	⋯	⋯
C	15259.16	483	⋯	6_0^1	6_0^1	33
	⋯	(563[b])	⋯	5_0^1	⋯	⋯
D	15446.94	671	$^2\Sigma^+ - {}^2\Pi$	4_0^1 [c]	4_0^1	37
E	15456.25	680	$^2\Sigma^+ - {}^2\Pi$	$6_0^1 7_0^1$ [c]	$6_0^1 7_0^1$	34
	⋯	(723[b])	⋯	⋯	5_0^1	⋯
	⋯	(869[b])	⋯	⋯	$4_0^1 7_0^1$	⋯
F	15653.43	877	⋯	$6_0^1 7_0^2$	$6_0^1 7_0^2$	⋯
G	15743.87	968	⋯	6_0^2	6_0^2	33
H	15820.87	1045	⋯	$5_0^1 6_0^1$	c-SiC_3H	⋯
I	15886.77	1111	⋯	⋯	$5_0^1 7_0^2$	⋯
J	15906.52	1130	⋯	5_0^2	c-SiC_3H	⋯
K	15926.12	1150	⋯	$4_0^1 6_0^1$	$4_0^1 6_0^1$	⋯
L	15938.67	1163	⋯	$6_0^2 7_0^1$	$6_0^2 7_0^1$	⋯
	⋯	(1201[b])	⋯	⋯	⋯	⋯
M	16114.94	1339	⋯	4_0^2 [c]	4_0^2	⋯
N	16124.37	1348	⋯	$4_0^1 6_0^1 7_0^1$ [c]	$4_0^1 6_0^1 7_0^1$	15
O	16135.73	1360	⋯	$6_0^2 7_0^2$ [c]	$6_0^2 7_0^2$	⋯
	⋯	(1383[b])	⋯	⋯	c-SiC_3H	⋯
P	16224.15	1448	⋯	3_0^1	$3_0^1 + 6_0^3$	12
	⋯	(1492[b])	⋯	⋯	$5_0^1 7_0^4$	⋯
	⋯	(1634[b])	⋯	⋯	⋯	⋯

(*Continued.*)

Band position (cm^{-1})	Relative energy (cm^{-1})	Band type	Assignment: This work	Assignment: Kokkin *et al.* [a]	τ (ns)
⋯	(1641[b])	⋯	⋯	$6^3_0 7^1_0$	⋯
⋯	(1645[b])	⋯	⋯	$6^3_0 7^1_0$	⋯

[a]Reference 3.

[b]Experimental value cited from Ref. 3.

[c]The upper states were mixed by Fermi interaction.

Table 5.5. Observed vibrational frequencies of SiC_3H in the $\tilde{A}$ state.

Mode	Type of mode	Obs. (cm^{-1})	Calc. (cm^{-1})
$\nu_1(\sigma)$	C_3–H stretch	⋯	3479
$\nu_2(\sigma)$	C_2–C_3 stretch	⋯	2057
$\nu_3(\sigma)$	C_1–C_2 stretch	1448	1456
$\nu_4(\sigma)$	Si–C_1 stretch	675	672
$\nu_5(\pi)$	C_2–C_3–H bend	563 (723[a])	561
$\nu_6(\pi)$	C_1–C_2–C_3 bend	483	471
$\nu_7(\pi)$	Si–C_1–C_2 bend	195	197

[a]Experimental value cited from Ref. 3.

561 cm^{-1}. Thus, it is necessary to re-examine the validity of the assignment of the ν_5 band at 0^0_0 + 723 cm^{-1}.

For relatively intense bands, fluorescence lifetimes were measured by fitting the fluorescence decay profiles to single exponential decay functions. All the observed lifetimes were much shorter than the estimated value for the natural radiative lifetime of the

$\tilde{A} \rightarrow \tilde{X}$ transition, τ_{sp} = 3.7 μs. The natural lifetime was estimated using the following expression,

$$\tau_{sp} = \frac{1}{A} = \frac{3\varepsilon_0 h}{16\pi^3 |\mu_{\tilde{A}-\tilde{X}}|^2 (\tilde{\nu}_{\tilde{A}-\tilde{X}})^3}, \tag{5.17}$$

where values for $\mu_{\tilde{A}-\tilde{X}}$ and $\tilde{\nu}_{\tilde{A}-\tilde{X}}$ were obtained by the *ab initio* transition moment presented in Table 5.1 and the experimental energy difference of 14776 cm^{-1}, respectively. The observed short lifetimes imply the existence of non-radiative relaxation processes such as a relaxation through an internal conversion (IC) to highly vibrationally excited levels in the $\tilde{X}$ state. As seen in Table 5.4, the fluorescence lifetimes become shorter for higher vibrational levels. For example, the lifetimes of the two vibrational levels at 0_0^0 + 1348 and 0_0^0 + 1448 cm^{-1} were shorter than one half of that of the zero-vibrational level in the $\tilde{A}$ state, indicating that the contributions of the non-radiative relaxation processes become larger in the higher energy region.

We observed rotationally-resolved LIF excitation spectra of the three intense bands, [A], [D], and [E]. Observed line positions are summarized in Appendix V. Figure 5.4 shows the observed high-resolution LIF spectrum of band [A] along with a simulation spectrum obtained using PGOPHER.[16] Although the origin band was not perturbed by other species, bands [D] and [E] were masked by C_2 Swan 5−8 and $d\,^3\Pi_g - c\,^3\Sigma_u^+$ 4−1 bands, which made it difficult to analyze the rotational structures of them. There is a significant difference in fluorescence lifetime between the bands [D]/[E] and the C_2 bands, τ ~35 and ~135 ns, respectively. Hence, in measuring the rotationally-resolved LIF spectra of bands [D] and [E], we set two different integration periods of the time profile in order to selectively obtain the LIF signals of SiC_3H. Fig. 5.5 presents the settings for the integration periods in the measurements. The integration periods were set to 0−50 (gate 1) and 50−100 (gate 2) ns after the laser pulse, respectively. Since the LIF signals integrated in gate 2 are almost only from C_2, it is possible to obtain the LIF spectrum in which the C_2 emissions are largely removed by subtracting the LIF signals integrated in gate 2 from those in gate 1. In this way, the rotationally-resolved LIF excitation spectra of bands [D] and [E] were obtained as shown in Figs. 5.6 and 5.7, respectively. Rotational structures of bands [A], [D], and [E] were

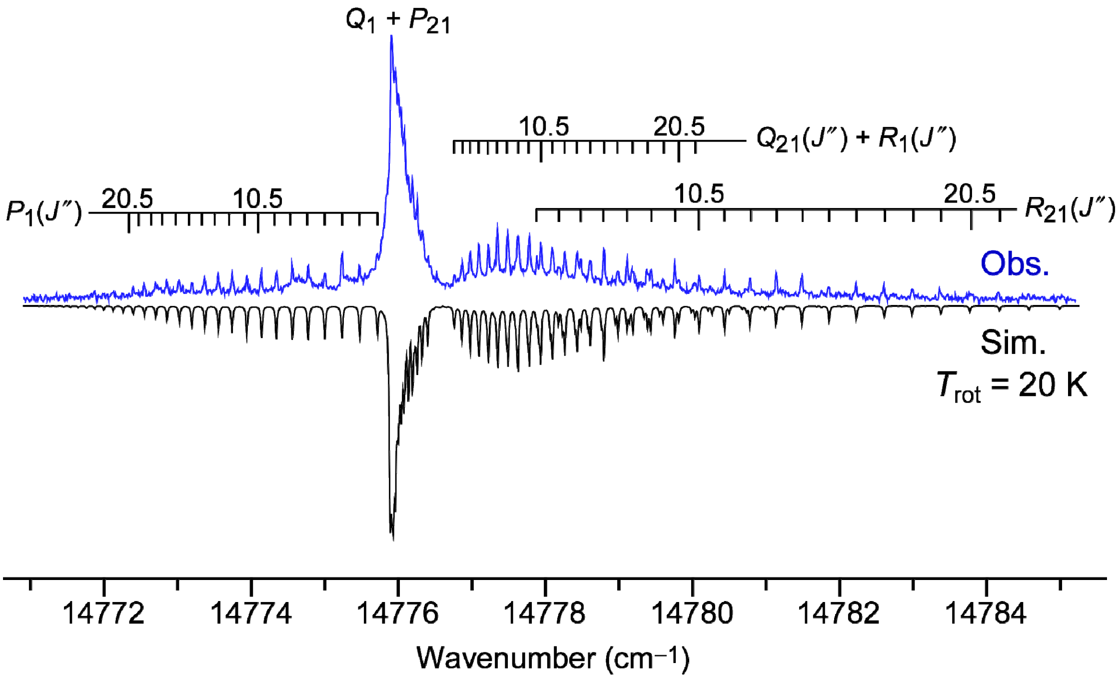

Figure 5.4. High resolution LIF spectrum of the $\tilde{A}-\tilde{X}$ 0_0^0 transition of SiC_3H. The $^2\Sigma^+ - {}^2\Pi$ type spectrum simulated by PGOPHER is shown in lower trace, where the rotational temperature and the line width were set to 20 K and 0.025 cm^{-1}, respectively.

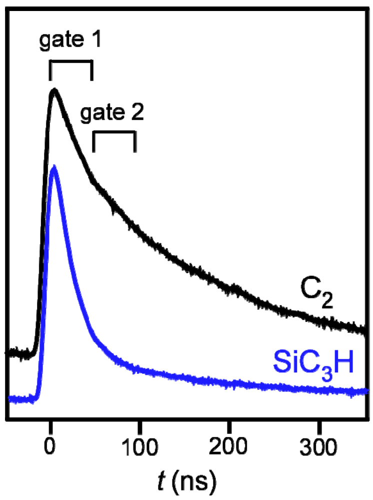

Figure 5.5. Settings for the integration periods in high-resolution spectroscopic studies for bands [D] and [E]. The fluorescence decay profile of SiC_3H was obtained by excitation of the Q_1 stack of band [E], while that of C_2 was obtained by excitation of the $R_1(2)$ branch of C_2 Swan 5−8 band at 15455.5 cm^{-1}.

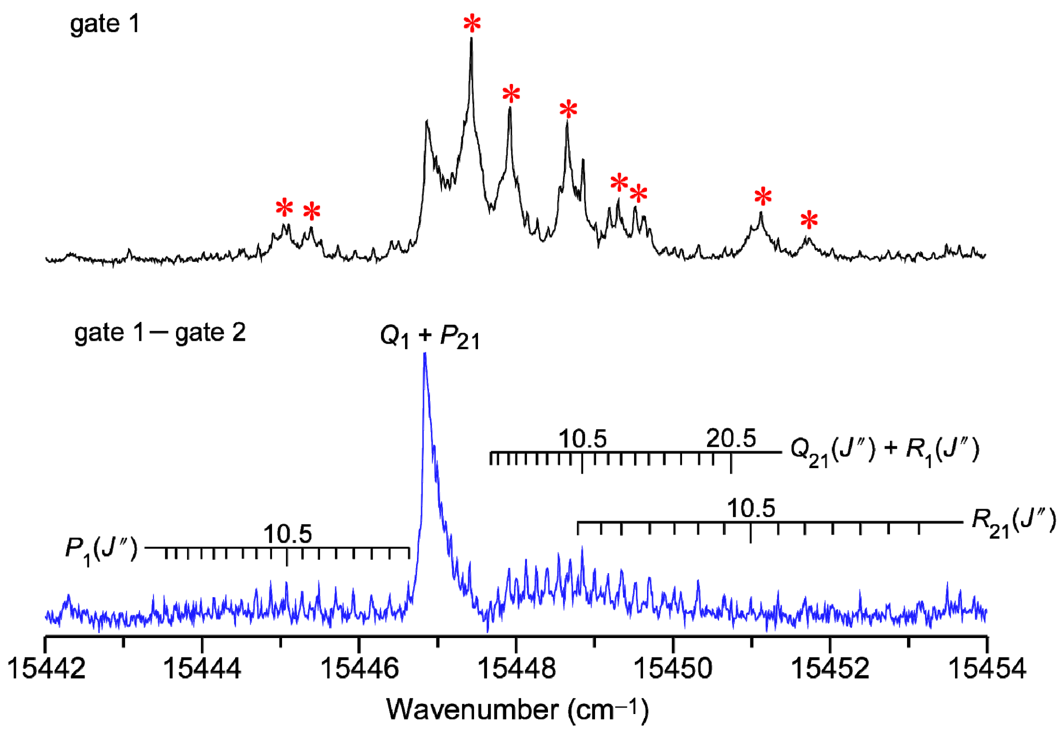

Figure 5.6. High resolution LIF spectrum of band [D]. Peaks with asterisks are originating from C_2.

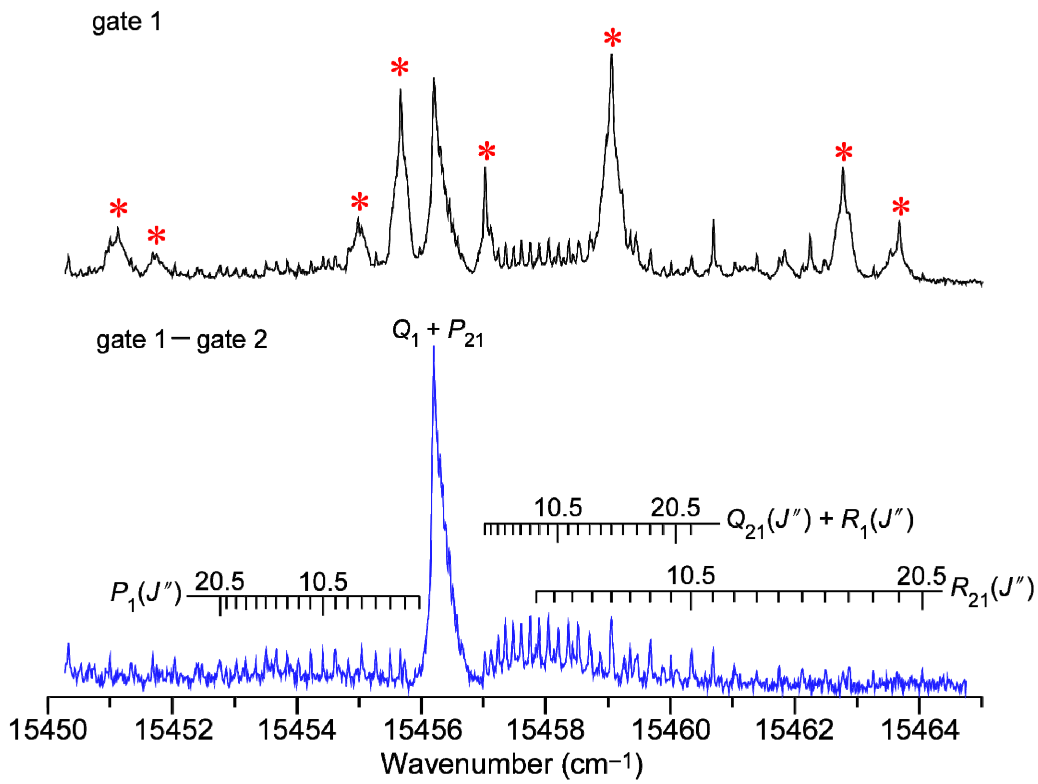

Figure 5.7. High resolution LIF spectrum of band [E]. Peaks with asterisks are originating from C_2.

analyzed using PGOPHER, where molecular constants of the ground vibrational level of the $\tilde{X}\,^2\Pi_{3/2}$ state were fixed to those previously reported by microwave spectroscopy.[3] For lower and upper levels, the following effective Hamiltonians for linear molecules,

$$\mathbf{H} = B\mathbf{R}^2 - D\mathbf{R}^4 + A_{\mathrm{SO}}L_zS_z + \tfrac{1}{2}q\left(N_+^2e^{-2i\phi} + N_-^2e^{-2i\phi}\right) \tag{5.18}$$

and

$$\mathbf{H} = B\mathbf{N}^2 + \gamma\mathbf{N}\cdot\mathbf{S}\,, \tag{5.19}$$

were used, respectively. Matrix elements were calculated using Hund's case (a) basis functions for both levels. Table 5.6 shows experimentally determined molecular constants of SiC_3H in the upper states. The standard deviations of the least-square analyses are comparable to the experimental accuracy of the measurement, 0.005 cm^{-1}. The determined rotational constants agree with the theoretical value, 0.0886 cm^{-1}, by about 1% errors. This agreement indicates that SiC_3H is linear in the $\tilde{A}$ state as expected by the *ab initio* calculation. For bands [D] and [E], the rotational constants B' are larger than that of the origin band by about 0.1%. In general, a rotational constant of a molecule becomes smaller with excitation of a stretching mode. On the other hand, it becomes larger with excitation of a bending mode. As mentioned above, the upper states of bands [D] and [E] were considered to be mixed states of 4^1 and 6^17^1 due to the Fermi interaction. The excitation

Table 5.6. Experimentally determined molecular constants of SiC_3H in the $\tilde{A}$ state (in cm^{-1}).[a,b]

Constants	0_0^0	band [D]	band [E]
T_0	14743.5929(14)	15414.5065(18)	15423.8449(13)
B'	0.0898013(59)	0.089871(10)	0.0899368(59)
γ'	−0.00229(13)	0.00144(18)	0.00116(12)
σ_{fit}	0.005	0.006	0.005

[a]Values in parentheses denote 1σ errors and these are applied to the last digits.

[b]Molecular constants of the ground vibronic level were fixed to experimental values presented in Ref. 3.

of the stretching mode ν_4 contributes to the decrease of the B value, while the excitations of the bending modes ν_6 and ν_7 may contribute oppositely. The fact that the B' values of bands [D] and [E] are larger than that of the 0^0 level means that the latter influence may be slightly larger.

DF spectrum

Figure 5.8 shows the observed DF spectrum from the 0^0 level. The observed vibrational levels were assigned on the basis of the theoretical vibrational frequencies presented in Tables 5.2 and 5.3. The assignments are summarized in Table 5.7. It was readily understood that the observed DF spectrum consists mainly of progression bands associated with the two stretching modes ν_3 and ν_4, where the ν_3 band was newly observed in the present study. This assignment is consistent with the strong ν_3 and ν_4 bands observed in the LIF excitation spectrum. These progression bands show spin-orbit splittings of ~65 cm^{-1}. Two weak bending vibrational bands, 6^0_1 and 7^0_1, were also observed. The assignment of the observed two bending vibrational levels to the

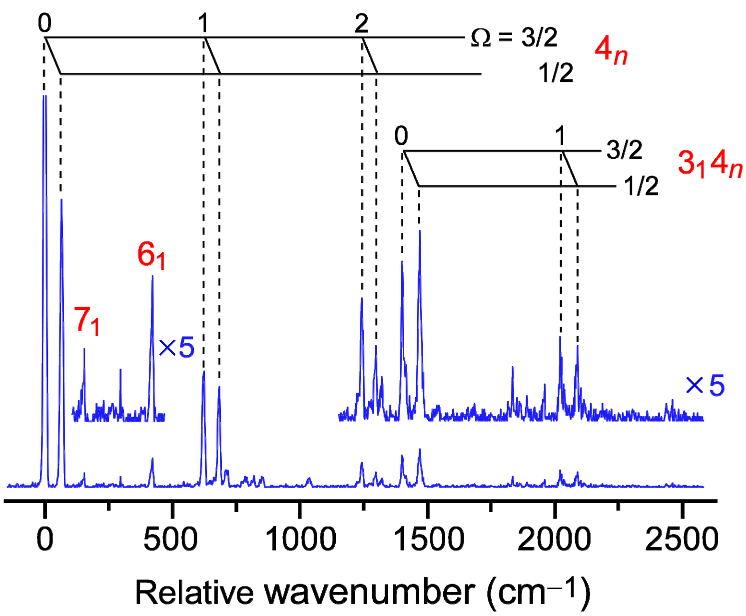

Figure 5.8. DF spectrum from the zero-vibrational level in the $\tilde{A}$ state.

Renner-Teller components of 6_1 and 7_1 were based on the term energies of the Renner-Teller components calculated using the *ab initio* bending vibrational frequencies listed in Table 5.2. The term energies of the unique ($^2\Delta_{3/2}$ and $^2\Delta_{5/2}$) and non-unique ($\mu\,^2\Sigma_{1/2}$ and $\kappa\,^2\Sigma_{1/2}$) levels in $\upsilon = 1$ are explicitly expressed by[13−15]

$$E\left(^2\Delta_{5/2}\right) = 2\omega - \tfrac{3}{4}\varepsilon^2\omega + \tfrac{1}{2}A_{true}(1 - \tfrac{3}{4}\varepsilon^2\omega)\,, \tag{5.20}$$

$$E\left(^2\Delta_{3/2}\right) = 2\omega - \tfrac{3}{4}\varepsilon^2\omega - \tfrac{1}{2}A_{true}(1 - \tfrac{3}{4}\varepsilon^2\omega)\,, \tag{5.21}$$

$$E\left(\mu\,^2\Sigma_{1/2}\right) = 2\omega(1 - \tfrac{1}{8}\varepsilon^2) - \tfrac{1}{2}\sqrt{A_{true}^{\ 2} + 4\varepsilon^2\omega^2}\,, \tag{5.22}$$

$$E\left(\kappa\,^2\Sigma_{1/2}\right) = 2\omega(1 - \tfrac{1}{8}\varepsilon^2) + \tfrac{1}{2}\sqrt{A_{true}^{\ 2} + 4\varepsilon^2\omega^2}\,. \tag{5.23}$$

The observed spin-orbit splittings of −65.6 cm^{-1} was used for A_{true} in Eqs. (5.20) to (5.23). As seen in Table 5.7, it is evident that the observed 7_1 level at 152 cm^{-1} is the $\mu\,^2\Sigma_{1/2}$ component. On the other hand, it was difficult to assign the observed 6_1 levels at 420 cm^{-1} to one of the four possible Renner-Teller components. We tentatively assigned it to the $\mu\,^2\Sigma_{1/2}$ component of the 6_1 level following the assignment by Kokkin *et al*.[3] In addition to the $\mu\,^2\Sigma_{1/2}$ component, they have observed the vibrational level, which can be assigned to the upper component $\kappa\,^2\Sigma_{1/2}$, at 552 cm^{-1} in the DF spectrum from the 6^1 level. The energy separation between $\mu\,^2\Sigma_{1/2}$ and $\kappa\,^2\Sigma_{1/2}$ of the 6_1 level, $\sqrt{A_{true}^{\ 2} + 4\varepsilon_6^{\ 2}\omega_6^{\ 2}}$, is calculated to be 125 cm^{-1}, and this value is consistent with the observation by Kokkin *et al*. For the stretching vibrational levels, the observed band positions are in excellent agreement with those calculated, showing the validity of the assignments.

Table 5.7. Vibrational levels of SiC_3H in the $\tilde{X}$ state observed in the DF spectrum from the 0^0 level.

Obs. (cm^{-1})	Calc. (cm^{-1})	Assignment
0.0	0 ($0_0\ ^2\Pi_{3/2}$)	$0_0\ ^2\Pi_{3/2}$
65.6	66 ($0_0\ ^2\Pi_{1/2}$)	$0_0\ ^2\Pi_{1/2}$
152.4	153 ($7_1\ \mu^2\Sigma_{1/2}$)[a]	$7_1\ \mu^2\Sigma_{1/2}$
⋯	156 ($7_1\ ^2\Delta_{5/2}$)[a]	⋯
⋯	221 ($7_1\ ^2\Delta_{3/2}$)[a]	⋯
⋯	227 ($7_1\ \kappa^2\Sigma_{1/2}$)[a]	⋯
420.1	363 ($6_1\ \mu^2\Sigma_{1/2}$)[a]	$6_1\ \mu^2\Sigma_{1/2}$
⋯	390 ($6_1\ ^2\Delta_{5/2}$)[a]	⋯
⋯	455 ($6_1\ ^2\Delta_{3/2}$)[a]	⋯
⋯	488 ($6_1\ \kappa^2\Sigma_{1/2}$)[a]	⋯
622.0	615 ($4_1\ ^2\Pi_{3/2}$)	$4_1\ ^2\Pi_{3/2}$
682.2	681 ($4_1\ ^2\Pi_{1/2}$)	$4_1\ ^2\Pi_{1/2}$
1242.6	1230 ($4_1\ ^2\Pi_{3/2}$)	$4_2\ ^2\Pi_{3/2}$
1295.5	1296 ($4_2\ ^2\Pi_{1/2}$)	$4_2\ ^2\Pi_{1/2}$
1401.0	1411 ($3_1\ ^2\Pi_{3/2}$)	$3_1\ ^2\Pi_{3/2}$
1469.0	1477 ($3_1\ ^2\Pi_{1/2}$)	$3_1\ ^2\Pi_{1/2}$
2021.7	2027 ($3_14_1\ ^2\Pi_{3/2}$)	$3_14_1\ ^2\Pi_{3/2}$
2085.1	2093 ($3_14_1\ ^2\Pi_{1/2}$)	$3_14_1\ ^2\Pi_{1/2}$

[a]Calculated using Eqs. (5.20) to (5.23).

References

[1]A. J. Apponi, M. C. McCarthy, C. A. Gottlieb, and P. Thaddeus, Astrophys. J. **536**, L55 (2000).

[2]M. C. McCarthy, A. J. Apponi, C. A. Gottlieb, and P. Thaddeus, J. Chem. Phys. **115**, 870 (2001).

[3]D. L. Kokkin, N. J. Reilly, R. C. Fortenberry, T. D. Crawford, and M. C. McCarthy, J. Chem. Phys. **141**, 044310 (2014).

[4]K. Hoshina, H. Kohguchi, Y. Ohshima, and Y. Endo, J. Chem. Phys. **108**, 3465 (1998).

[5]K. Hoshina and Y. Endo, J. Chem. Phys. **127**, 184304 (2007).

[6]R. Cireasa, D. Cossart, and M. Vervloet, Eur. Phys. J. D **2**, 199 (1998).

[7]T. C. Smith, H. Li, and D. J. Clouthier, J. Am. Chem. Soc. **121**, 6068 (1999).

[8]T. C. Smith, H. Li, D. J. Clouthier, C. T. Kingston, and A. J. Merer, J. Chem. Phys. **112**, 3662 (2000).

[9]T. C. Smith, H. Li, D. A. Hostutler, D. J. Clouthier, and A. J. Merer, J. Chem. Phys. **114**, 725 (2001).

[10]T. C. Smith, D. J. Clouthier, and T. C. Steimle, J. Chem. Phys. **115**, 817 (2001).

[11]W. -B. Yan and T. Amano, J. Chem. Phys. **99**, 4312 (1993).

[12]H.-J. Werner, P. J. Knowles, F. R. Manby, M. Schütz *et al.*, MOLPRO, version 2012.1, a package of *ab initio* programs, 2012, see http://www.molpro.net.

[13]J. A. Pople, Mol. Phys. **3**, 16 (1960).

[14]J. T. Hougen, J. Chem. Phys. **36**, 519 (1962).

[15]J. F. M. Aarts, Mol. Phys. **35**, 1785 (1978).

[16]C. M. Western, PGOPHER, a program for simulating rotational, vibrational and electronic structure of spectra, University of Bristol, 2010, see http://pgopher.chm.bris.ac.uk.

Appendix I

Observed Transition Frequencies of CH_2CCHO (in MHz)

N'	K_a'	K_c'	J'	F_1' [a]	F'	N''	K_a''	K_c''	J''	F_1'' [a]	F''	I_1	Obs.	Obs. − Calc.
1	0	1	1.5	2.5	3.0	0	0	0	0.5	1.5	2.0	1	8828.335	0.007
1	0	1	1.5	2.5	2.0	0	0	0	0.5	1.5	1.0	1	8828.631	0.009
1	0	1	1.5	2.5	2.0	0	0	0	0.5	1.5	2.0	1	8829.319	0.009
1	0	1	1.5	1.5	2.0	0	0	0	0.5	0.5	1.0	1	8841.654	0.003
1	0	1	1.5	1.5	1.0	0	0	0	0.5	0.5	0.0	1	8841.815	0.007
1	0	1	1.5	1.5	1.0	0	0	0	0.5	0.5	1.0	1	8841.489	0.023
1	0	1	1.5	0.5	1.0	0	0	0	0.5	0.5	0.0	1	8832.309	0.008
1	0	1	1.5	0.5	0.0	0	0	0	0.5	0.5	1.0	1	8832.771	0.010
1	0	1	1.5		2.0	0	0	0	0.5		1.0	0	8828.908	0.009
1	0	1	1.5		1.0	0	0	0	0.5		0.0	0	8828.970	0.011
1	0	1	1.5		1.0	0	0	0	0.5		1.0	0	8829.999	0.009
2	0	2	2.5	3.5	4.0	1	0	1	1.5	2.5	3.0	1	17667.199	−0.001
2	0	2	2.5	3.5	3.0	1	0	1	1.5	2.5	2.0	1	17667.311	0.006
2	0	2	2.5	2.5	3.0	1	0	1	1.5	1.5	2.0	1	17679.037	0.005
2	0	2	2.5	2.5	2.0	1	0	1	1.5	1.5	1.0	1	17679.158	0.004
2	0	2	2.5	1.5	2.0	1	0	1	1.5	0.5	1.0	1	17673.046	0.003
2	0	2	2.5	1.5	1.0	1	0	1	1.5	0.5	0.0	1	17672.927	−0.004
2	0	2	2.5		3.0	1	0	1	1.5		2.0	0	17667.445	0.000
2	0	2	2.5		2.0	1	0	1	1.5		1.0	0	17667.497	0.002
2	0	2	1.5	2.5	3.0	1	0	1	0.5	1.5	2.0	1	17676.256	0.005
2	0	2	1.5	2.5	2.0	1	0	1	0.5	1.5	1.0	1	17676.602	0.017
2	0	2	1.5	1.5	2.0	1	0	1	0.5	0.5	1.0	1	17685.797	0.017
2	0	2	1.5	1.5	1.0	1	0	1	0.5	0.5	0.0	1	17684.160	0.015
2	0	2	1.5	0.5	1.0	1	0	1	0.5	0.5	1.0	1	17691.797	0.012
2	0	2	1.5	0.5	1.0	1	0	1	0.5	0.5	0.0	1	17691.046	0.011

(*Continued*.)

N'	K_a'	K_c'	J'	F_1' [a]	F'	N''	K_a''	K_c''	J''	F_1'' [a]	F''	I_1	Obs.	Obs. − Calc.
2	0	2	1.5	0.5	0.0	1	0	1	0.5	0.5	1.0	1	17690.377	0.007
2	0	2	1.5	1.5	2.0	1	0	1	0.5	1.5	2.0	1	17689.760	0.000
2	0	2	1.5	1.5	1.0	1	0	1	0.5	1.5	1.0	1	17689.625	0.013
2	0	2	1.5		2.0	1	0	1	0.5		1.0	0	17688.146	0.007
2	0	2	1.5		1.0	1	0	1	0.5		0.0	0	17688.870	−0.002
2	0	2	1.5		1.0	1	0	1	0.5		1.0	0	17686.516	0.010
2	1	1	2.5	2.5	3.0	1	1	0	1.5	1.5	2.0	1	17959.729	−0.026
2	1	1	2.5	2.5	2.0	1	1	0	1.5	1.5	1.0	1	17960.039	−0.029
2	1	1	2.5	1.5	2.0	1	1	0	1.5	0.5	1.0	1	17963.548	−0.031
2	1	1	1.5	2.5	3.0	1	1	0	0.5	1.5	2.0	1	17822.750	−0.001
2	1	1	1.5	2.5	2.0	1	1	0	0.5	1.5	1.0	1	17821.105	−0.012
2	1	1	1.5	1.5	2.0	1	1	0	0.5	0.5	1.0	1	17814.664	−0.010
2	1	1	1.5	1.5	2.0	1	1	0	0.5	1.5	2.0	1	17870.735	−0.002
2	1	1	1.5		2.0	1	1	0	0.5		1.0	0	17826.961	0.000
2	1	2	2.5	3.5	4.0	1	1	1	1.5	2.5	3.0	1	17464.315	−0.008
2	1	2	2.5	3.5	3.0	1	1	1	1.5	2.5	2.0	1	17464.827	−0.050
2	1	2	2.5	2.5	3.0	1	1	1	1.5	1.5	2.0	1	17467.070	−0.005
2	1	2	2.5	2.5	2.0	1	1	1	1.5	1.5	1.0	1	17467.452	−0.002
2	1	2	2.5		3.0	1	1	1	1.5		2.0	0	17464.997	−0.009
2	1	2	2.5		2.0	1	1	1	1.5		1.0	0	17465.537	−0.003
2	1	2	1.5	2.5	3.0	1	1	1	0.5	1.5	2.0	1	17318.538	−0.011
2	1	2	1.5	2.5	2.0	1	1	1	0.5	1.5	1.0	1	17317.683	−0.014
3	0	3	3.5	4.5	5.0	2	0	2	2.5	3.5	4.0	1	26503.748	−0.014
3	0	3	3.5	4.5	4.0	2	0	2	2.5	3.5	3.0	1	26503.807	−0.011
3	0	3	3.5	3.5	4.0	2	0	2	2.5	2.5	3.0	1	26514.324	−0.009
3	0	3	3.5	3.5	3.0	2	0	2	2.5	2.5	2.0	1	26514.448	−0.005
3	0	3	3.5	2.5	3.0	2	0	2	2.5	1.5	2.0	1	26508.745	−0.011

(*Continued.*)

N'	K_a'	K_c'	J'	F_1' [a]	F'	N''	K_a''	K_c''	J''	F_1'' [a]	F''	I_1	Obs.	Obs. − Calc.
3	0	3	3.5	2.5	2.0	2	0	2	2.5	1.5	1.0	1	26508.798	−0.003
3	0	3	3.5		4.0	2	0	2	2.5		3.0	0	26503.881	−0.017
3	0	3	3.5		3.0	2	0	2	2.5		2.0	0	26503.926	−0.005
3	0	3	2.5	3.5	4.0	2	0	2	1.5	2.5	3.0	1	26513.701	−0.014
3	0	3	2.5	3.5	3.0	2	0	2	1.5	2.5	2.0	1	26513.731	−0.002
3	0	3	2.5	2.5	3.0	2	0	2	1.5	1.5	2.0	1	26520.069	−0.005
3	0	3	2.5	2.5	2.0	2	0	2	1.5	1.5	1.0	1	26520.015	0.000
3	0	3	2.5	1.5	2.0	2	0	2	1.5	0.5	1.0	1	26525.011	−0.001
3	0	3	2.5	1.5	1.0	2	0	2	1.5	0.5	0.0	1	26525.011	−0.006
3	0	3	2.5	1.5	2.0	2	0	2	1.5	1.5	2.0	1	26531.013	−0.004
3	0	3	2.5	1.5	1.0	2	0	2	1.5	1.5	1.0	1	26530.491	−0.002
3	0	3	2.5	2.5	3.0	2	0	2	1.5	2.5	3.0	1	26533.578	−0.005
3	0	3	2.5	2.5	2.0	2	0	2	1.5	2.5	2.0	1	26533.040	−0.001
3	0	3	2.5		3.0	2	0	2	1.5		2.0	0	26524.302	−0.007
3	0	3	2.5		2.0	2	0	2	1.5		1.0	0	26524.447	0.002
3	1	2	3.5	4.5	5.0	2	1	1	2.5	3.5	4.0	1	26896.600	0.018
3	1	2	3.5	4.5	4.0	2	1	1	2.5	3.5	3.0	1	26896.670	−0.001
3	1	2	3.5	3.5	4.0	2	1	1	2.5	2.5	3.0	1	26899.793	0.019
3	1	2	3.5	3.5	3.0	2	1	1	2.5	2.5	2.0	1	26899.879	0.003
3	1	2	3.5	2.5	3.0	2	1	1	2.5	1.5	2.0	1	26900.742	0.015
3	1	2	3.5	2.5	2.0	2	1	1	2.5	1.5	1.0	1	26900.854	0.002
3	1	2	3.5		4.0	2	1	1	2.5		3.0	0	26896.919	0.016
3	1	2	3.5		3.0	2	1	1	2.5		2.0	0	26896.982	−0.006
3	1	2	2.5	3.5	4.0	2	1	1	1.5	2.5	3.0	1	26864.336	0.000
3	1	2	2.5	3.5	3.0	2	1	1	1.5	2.5	2.0	1	26863.956	−0.002
3	1	2	2.5	2.5	3.0	2	1	1	1.5	1.5	2.0	1	26863.408	0.002
3	1	2	2.5	2.5	2.0	2	1	1	1.5	1.5	1.0	1	26863.061	0.000

(*Continued.*)

N'	K_a'	K_c'	J'	F_1' [a]	F'	N''	K_a''	K_c''	J''	F_1'' [a]	F''	I_1	Obs.	Obs. − Calc.
3	1	2	2.5	1.5	2.0	2	1	1	1.5	0.5	1.0	1	26866.489	0.005
3	1	2	2.5		3.0	2	1	1	1.5		2.0	0	26866.805	0.003
3	1	2	2.5		2.0	2	1	1	1.5		1.0	0	26866.395	0.000
3	1	3	3.5	4.5	5.0	2	1	2	2.5	3.5	4.0	1	26159.181	0.007
3	1	3	3.5	4.5	4.0	2	1	2	2.5	3.5	3.0	1	26159.417	0.007
3	1	3	3.5	3.5	4.0	2	1	2	2.5	2.5	3.0	1	26157.006	0.006
3	1	3	3.5	3.5	3.0	2	1	2	2.5	2.5	2.0	1	26157.006	0.007
3	1	3	3.5	2.5	3.0	2	1	2	2.5	1.5	2.0	1	26161.119	0.006
3	1	3	3.5	2.5	2.0	2	1	2	2.5	1.5	1.0	1	26161.269	0.013
3	1	3	3.5		4.0	2	1	2	2.5		3.0	0	26159.481	0.008
3	1	3	3.5		3.0	2	1	2	2.5		2.0	0	26159.696	0.007
3	1	3	2.5	3.5	4.0	2	1	2	1.5	2.5	3.0	1	26112.428	0.003
3	1	3	2.5	3.5	3.0	2	1	2	1.5	2.5	2.0	1	26112.562	0.006
3	1	3	2.5	2.5	3.0	2	1	2	1.5	1.5	2.0	1	26108.365	−0.001
3	1	3	2.5	2.5	2.0	2	1	2	1.5	1.5	1.0	1	26108.119	−0.001
3	1	3	2.5	1.5	2.0	2	1	2	1.5	0.5	1.0	1	26109.408	0.000
3	1	3	2.5		3.0	2	1	2	1.5		2.0	0	26109.546	0.002
2	1	2	2.5	3.5	4.0	1	0	1	1.5	2.5	3.0	1	64085.930	−0.005
2	1	2	2.5	3.5	3.0	1	0	1	1.5	2.5	2.0	1	64086.291	−0.007
2	1	2	2.5	3.5	3.0	1	0	1	1.5	2.5	3.0	1	64087.274	−0.006
2	1	2	2.5	2.5	3.0	1	0	1	1.5	2.5	3.0	1	63950.771	0.003
2	1	2	2.5	2.5	2.0	1	0	1	1.5	2.5	2.0	1	63950.615	0.005
2	1	2	2.5	2.5	3.0	1	0	1	1.5	1.5	2.0	1	64141.425	0.009
2	1	2	2.5	2.5	2.0	1	0	1	1.5	1.5	1.0	1	64142.437	0.011
2	1	2	2.5	2.5	2.0	1	0	1	1.5	1.5	2.0	1	64142.248	0.008
2	1	2	2.5	1.5	2.0	1	0	1	1.5	0.5	1.0	1	64105.605	−0.002
2	1	2	2.5	1.5	1.0	1	0	1	1.5	0.5	1.0	1	64106.805	0.001

(*Continued*.)

N'	K_a'	K_c'	J'	F_1' [a]	F'	N''	K_a''	K_c''	J''	F_1'' [a]	F''	I_1	Obs.	Obs. − Calc.
2	1	2	2.5	1.5	2.0	1	0	1	1.5	1.5	2.0	1	64095.917	0.003
2	1	2	2.5	1.5	2.0	1	0	1	1.5	1.5	1.0	1	64096.102	0.003
2	1	2	2.5	1.5	1.0	1	0	1	1.5	1.5	2.0	1	64097.110	−0.001
2	1	2	2.5	1.5	1.0	1	0	1	1.5	1.5	1.0	1	64097.299	0.003
2	1	2	2.5		3.0	1	0	1	1.5		2.0	0	64085.697	−0.003
2	1	2	2.5		2.0	1	0	1	1.5		1.0	0	64086.014	−0.007
2	1	2	2.5		2.0	1	0	1	1.5		2.0	0	64087.108	−0.004
2	1	2	1.5	2.5	3.0	1	0	1	1.5	2.5	3.0	1	64250.761	−0.002
2	1	2	1.5	2.5	3.0	1	0	1	1.5	2.5	2.0	1	64249.776	−0.005
2	1	2	1.5	2.5	2.0	1	0	1	1.5	2.5	3.0	1	64249.098	0.001
2	1	2	1.5	2.5	2.0	1	0	1	1.5	2.5	2.0	1	64248.112	−0.003
2	1	2	1.5	2.5	3.0	1	0	1	1.5	1.5	2.0	1	64441.411	0.000
2	1	2	1.5	2.5	2.0	1	0	1	1.5	1.5	2.0	1	64439.744	−0.001
2	1	2	1.5	2.5	2.0	1	0	1	1.5	1.5	1.0	1	64439.930	0.000
2	1	2	1.5	1.5	2.0	1	0	1	1.5	2.5	3.0	1	64295.240	0.011
2	1	2	1.5	1.5	1.0	1	0	1	1.5	2.5	2.0	1	64292.631	0.000
2	1	2	1.5	1.5	2.0	1	0	1	1.5	0.5	1.0	1	64495.567	−0.002
2	1	2	1.5	1.5	1.0	1	0	1	1.5	0.5	1.0	1	64493.959	0.005
2	1	2	1.5		2.0	1	0	1	1.5		2.0	0	64318.093	−0.002
2	1	2	1.5		2.0	1	0	1	1.5		1.0	0	64317.000	−0.005
2	1	2	1.5		1.0	1	0	1	1.5		2.0	0	64315.777	0.000
2	1	2	1.5		1.0	1	0	1	1.5		1.0	0	64314.680	−0.006
3	1	3	3.5	4.5	5.0	2	0	2	2.5	3.5	4.0	1	72577.913	0.001
3	1	3	3.5	4.5	4.0	2	0	2	2.5	3.5	3.0	1	72578.409	0.001
3	1	3	3.5	3.5	4.0	2	0	2	2.5	2.5	3.0	1	72619.397	0.010
3	1	3	3.5	3.5	3.0	2	0	2	2.5	2.5	2.0	1	72620.280	0.006
3	1	3	3.5	2.5	3.0	2	0	2	2.5	1.5	2.0	1	72593.677	−0.002

(*Continued.*)

N'	K_a'	K_c'	J'	F_1' [a]	F'	N''	K_a''	K_c''	J''	F_1'' [a]	F''	I_1	Obs.	Obs. − Calc.
3	1	3	3.5	2.5	2.0	2	0	2	2.5	1.5	1.0	1	72594.331	0.001
3	1	3	3.5		4.0	2	0	2	2.5		3.0	0	72577.737	0.005
3	1	3	3.5		3.0	2	0	2	2.5		2.0	0	72578.216	−0.003
3	1	3	2.5	3.5	4.0	2	0	2	1.5	2.5	3.0	1	72664.902	−0.004
3	1	3	2.5	3.5	3.0	2	0	2	1.5	2.5	2.0	1	72663.768	−0.006
3	1	3	2.5	2.5	3.0	2	0	2	1.5	1.5	2.0	1	72691.809	0.004
3	1	3	2.5	2.5	2.0	2	0	2	1.5	1.5	1.0	1	72690.829	0.001
3	1	3	2.5	1.5	2.0	2	0	2	1.5	0.5	1.0	1	72708.749	−0.001
3	1	3	2.5		3.0	2	0	2	1.5		2.0	0	72707.347	0.005
3	1	3	2.5		2.0	2	0	2	1.5		1.0	0	72706.625	−0.004

[a]Transitions without F_1' and F_1'' values are those for $I_1 = 0$, and others for $I_1 = 1$.

Appendix II
Hamiltonian for Doublet Asymmetric Top Molecules

An effective Hamiltonian for doublet asymmetric top molecules including fine- and hyperfine- interactions is given by

$$\mathbf{H} = \mathbf{H}_{rot} + \mathbf{H}_{cd} + \mathbf{H}_{sr} + \mathbf{H}_{srcd} + \mathbf{H}_{hfs} \,. \tag{A-II.1}$$

The first term is a rotational energy term explicitly expressed by

$$\mathbf{H}_{rot} = AN_a{}^2 + BN_b{}^2 + CN_c{}^2 \,. \tag{A-II.2}$$

The second term is the centrifugal distortion term and is written in terms of Watson's A-reduced form as

$$\begin{aligned}\mathbf{H}_{cd} = &-\mathit{\Delta}_N \mathbf{N}^4 - \mathit{\Delta}_{NK} \mathbf{N}^2 N_a{}^2 - \mathit{\Delta}_K N_a{}^4 - 2\delta_N \mathbf{N}^2 \left(N_+{}^2 - N_-{}^2\right) \\ &-\delta_K \left[N_+{}^2 + N_-{}^2,\ N_a{}^2\right]_+ ,\end{aligned} \tag{A-II.3}$$

where $[\mathrm{A},\ \mathrm{B}]_+ = \mathrm{A\,B} + \mathrm{B\,A}$. The third term is the spin-rotation interaction term,

$$\mathbf{H}_{sr} = \varepsilon_{aa} N_a S_a + \varepsilon_{bb} N_b S_b + \varepsilon_{cc} N_c S_c + (\varepsilon_{ab} + \varepsilon_{ba})(N_a S_b + N_b S_a)/2 \,, \tag{A-II.4}$$

where $\varepsilon_{ac} = \varepsilon_{ca} = 0$. The fourth term is the centrifugal distortion term of the spin-rotation interaction,

$$\begin{aligned}\mathbf{H}_{srcd} = &\mathit{\Delta}_N^S \mathbf{N}^2 (\mathbf{N}\cdot\mathbf{S}) + \frac{1}{2}\mathit{\Delta}_{NK}^S \left(\mathbf{N}^2 N_a S_a + N_a S_a \mathbf{N}^2\right) + \mathit{\Delta}_{KN}^S N_a \mathbf{N}\cdot\mathbf{S} + \mathit{\Delta}_K^S N_a{}^3 S_a \\ &+\delta_N^S \left(N_+{}^2 + N_-{}^2\right)\mathbf{N}\cdot\mathbf{S} + \frac{1}{2}\delta_K^S \left\{\left(N_+{}^2 + N_-{}^2\right) N_a S_a + N_a S_a \left(N_+{}^2 + N_-{}^2\right)\right\} .\end{aligned} \tag{A-II.5}$$

All the matrix elements of the spin-rotation interaction for a C_s molecule are

$$\begin{aligned}\langle NKSJ|\mathbf{H}_{sr} + \mathbf{H}_{srcd}|NKSJ\rangle = &-[\mathit{\Gamma}(NSJ)/2N(N+1)]\{\varepsilon_{aa}K^2 + (\varepsilon_{bb} + \varepsilon_{cc}) \\ &\times\left[N(N+1) - K^2\right]/2 + \mathit{\Delta}_K^S K^4 + \left(\mathit{\Delta}_{NK}^S + \mathit{\Delta}_{KN}^S\right) K^2 N(N+1) + \mathit{\Delta}_N^S N^2 (N+1)^2\right\} ,\end{aligned} \tag{A-II.6}$$

$$\begin{aligned}\langle NK\pm1, SJ|\mathbf{H}_{sr} + \mathbf{H}_{srcd}|NKSJ\rangle = &-[\mathit{\Gamma}(NSJ)(2K\pm1)/4N(N+1)] \\ &\times[N(N+1) - K(K\pm1)]^{1/2}(\varepsilon_{ab} + \varepsilon_{ba})/2 ,\end{aligned} \tag{A-II.7}$$

$$\begin{aligned}\langle NK\pm2, SJ|\mathbf{H}_{sr} + \mathbf{H}_{srcd}|NKSJ\rangle = &-[\mathit{\Gamma}(NSJ)/4N(N+1)]\{[N(N+1) - K(K\pm1)] \\ &\times[N(N+1) - (K\pm1)(K\pm2)]^{1/2}\{(\varepsilon_{bb} - \varepsilon_{cc})/2 + 2\delta_N^S N(N+1) \\ &+\delta_K^S\left[K^2 + (K\pm2)^2\right]\right\} ,\end{aligned} \tag{A-II.8}$$

$$\langle N-1, KSJ|\mathbf{H}_{sr} + \mathbf{H}_{srcd}|NKSJ\rangle = -\phi(NSJ)(K/2N)\left(N^2 - K^2\right)^{1/2}$$

$$\times\left\{\varepsilon_{aa}-\left(\varepsilon_{bb}+\varepsilon_{cc}\right)/2+\Delta_K^S K^2+\Delta_{NK}^S N^2\right\}, \tag{A-II.9}$$

$$\left\langle N-1,K\pm 1,SJ\left|\mathbf{H}_{sr}+\mathbf{H}_{srcd}\right|NKSJ\right\rangle=-\phi(NSJ)\left[N\pm 2K+1/4N\right]$$

$$\times\left[(N\mp K)(N\mp K-1)\right]^{1/2}\left(\varepsilon_{ab}+\varepsilon_{ba}\right)/2, \tag{A-II.10}$$

$$\left\langle N-1,K\pm 2,SJ\left|\mathbf{H}_{sr}+\mathbf{H}_{srcd}\right|NKSJ\right\rangle=-\left[\phi(NSJ)/4N\right]\left[(N\mp K)(N\mp K-1)\right.$$

$$\left.\times(N\mp K-2)\right]^{1/2}\left\{\pm\left(\varepsilon_{bb}-\varepsilon_{cc}\right)/2+\delta_K^S\left[K(N\pm K)+(K\pm 2)(N\pm K+2)\right]\right\}, \tag{A-II.11}$$

where

$$\Gamma(NSJ)=N(N+1)+S(S+1)-J(J+1) \tag{A-II.12}$$

and

$$\phi(NSJ)=\left[(N-J+S)(N+J+S+1)(S+J-N+1)\right.$$

$$\left.\times(N+J-S)/(2N+1)(2N-1)\right]. \tag{A-II.13}$$

The term $\mathbf{H}_{hfs}$ is the hyperfine interaction term and is composed of the Fermi contact interaction, the magnetic dipole-dipole interaction, and the electric quadrupole interaction terms,

$$\mathbf{H}_{hfs}=a_F\mathbf{T}^1(\mathbf{S})\mathbf{T}^1(\mathbf{I})-\sqrt{10}\,g_S g_N\mu_B\mu_N\mathbf{T}^1(\mathbf{I})\mathbf{T}^1\left(\mathbf{S},C^2\right)+\mathbf{T}^2(\mathbf{Q})\cdot\mathbf{T}^2(\nabla\mathbf{E}), \tag{A-II.14}$$

where a_F is the Fermi contact constant given by

$$a_F=\frac{8\pi}{3}g_S g_N\mu_B\mu_N\left|\psi_{1s}(0)\right|^2, \tag{A-II.15}$$

and

$$\mathbf{T}^1(\mathbf{I})\mathbf{T}^1\left(\mathbf{S},C^2\right)=-\sum_{p,q}\sqrt{3}\begin{pmatrix}1 & 1 & 2\\ p & q-p & -q\end{pmatrix}T_p^{\,1}(\mathbf{I})T_{q-p}^{\,1}(\mathbf{S})C_{-q}^2(\theta,\phi)r^{-3}, \tag{A-II.16}$$

$$\mathbf{T}^2(\mathbf{Q})=\sum_n e_n r_n^2 C^2(\theta_n,\phi_n), \tag{A-II.17}$$

$$\mathbf{T}^2(\nabla\mathbf{E})=-\sum_i e_i C^2(\theta_n,\phi_n)r_i^{-3}. \tag{A-II.18}$$

The function $C_q^2(\theta,\phi)$ is related to the second-rank spherical harmonics as

$$C_q^2(\theta,\phi)=\sqrt{\tfrac{4\pi}{5}}Y_{2q}(\theta,\phi). \tag{A-II.19}$$

Using Hund's case (b)$_\beta$ basis sets, all the matrix elements of the hyperfine interaction are

$$\left\langle N'K'S'J'I'F'M_F'\left|\mathbf{H}_{hfs}\right|NKSJIFM_F\right\rangle=\delta_{M_F M_F'}\delta_{FF'}\delta_{NN'}\delta_{KK'}(-1)^{N+S+J'}(-1)^{J+I+F+1}$$

$$\times\left[(2J'+1)(2J+1)S(S+1)(2S+1)I(I+1)(2I+1)\right]^{1/2}$$

$$\times\begin{Bmatrix} I & J' & F \\ J & I & 1 \end{Bmatrix}\begin{Bmatrix} S & J' & N \\ J & S & 1 \end{Bmatrix} b_\eta$$

$$-\delta_{M_F M_F'}\delta_{FF'}\sqrt{30}g_S g_N \mu_B \mu_N (-1)^{J+I+F}$$

$$\times[(2J'+1)(2J+1)(2N'+1)(2N+1)]^{1/2}$$

$$\times\begin{Bmatrix} I & J' & F \\ J & I & 1 \end{Bmatrix}\begin{Bmatrix} N' & N & 2 \\ S & S & 1 \\ J' & J & 1 \end{Bmatrix}\sum_q (-1)^{N'-K'}\begin{pmatrix} N' & 2 & N \\ -K' & q & K \end{pmatrix} T_q^{\,2}(C)$$

$$+\delta_{M_F M_F'}\delta_{FF'}(eQ/2)(-1)^{J+I+F}(-1)^{N'+S+J}$$

$$\times\{(I+1)(2I+1)(2I+3)/[I(I+1)]\}^{1/2}$$

$$\times[(2J'+1)(2J+1)(2N'+1)(2N+1)]^{1/2}$$

$$\times\begin{Bmatrix} I & J' & F \\ J & I & 2 \end{Bmatrix}\begin{Bmatrix} N' & J' & S \\ J & N & 2 \end{Bmatrix}$$

$$\times\sum_q (-1)^{N'-K'}\begin{pmatrix} N' & 2 & N \\ -K' & q & K \end{pmatrix} T_q^{\,2}(\nabla E), \tag{A-II.20}$$

where $T_q^{\,2}(C)$ is defined as

$$T_q^{\,2}(C) = \langle n | C_q^2(\theta, \phi) r^{-3} | n \rangle, \tag{A-II.21}$$

and, its five components are related to those in the Cartesian coordinate system as

$$g_S g_N \mu_B \mu_N T_0^{\,2}(C) = \frac{T_{zz}}{2} = -\frac{(T_{xx}+T_{yy})}{2}, \tag{A-II.22}$$

$$g_S g_N \mu_B \mu_N T_{\pm1}^{\,2}(C) = \mp\frac{(T_{xz} \pm iT_{yz})}{\sqrt{6}}, \tag{A-II.23}$$

$$g_S g_N \mu_B \mu_N T_{\pm2}^{\,2}(C) = \frac{(T_{xx} - T_{yy} \pm 2iT_{xy})}{\sqrt{24}}. \tag{A-II.24}$$

Similarly, for the quadrupole coupling tensor,

$$eQT_0^{\,2}(\nabla E) = \frac{\chi_{zz}}{2}, \tag{A-II.25}$$

$$eQT_{\pm1}^{\,2}(\nabla E) = \mp\frac{(\chi_{xz} \pm i\chi_{yz})}{\sqrt{6}}, \tag{A-II.26}$$

$$eQT_{\pm 2}^{2}(\nabla E)=\frac{\left(\chi_{xx}-\chi_{yy}\pm 2i\chi_{xy}\right)}{\sqrt{24}}. \qquad \text{(A-II.27)}$$

In GAUSSIAN, the magnetic dipole-dipole interaction and the quadrupole coupling tensors are calculated in the Cartesian tensor forms.

Appendix III
Hamiltonian for Linear Molecules in $^2\Pi$ Electronic States

An effective Hamiltonian for poly-atomic linear molecules in $^2\Pi$ electronic states including fine interactions is given by

$$\mathbf{H} = \mathbf{H}_{rot} + \mathbf{H}_{so} + \mathbf{H}_{socd} + \mathbf{H}_{sr} + \mathbf{H}_{\Lambda} . \tag{A-III.1}$$

The first term is a rotational energy term explicitly expressed by

$$\mathbf{H}_{rot} = B\left(\mathbf{J}^2 - J_z^{\ 2} + \mathbf{S}^2 - S_z^{\ 2}\right) - B\left(J_+ S_- + J_- S_+\right) - D\left(\mathbf{J} - \mathbf{L} - \mathbf{S}\right)^4 . \tag{A-III.2}$$

The second term is the spin-orbit interaction term,

$$\mathbf{H}_{so} = A_{so} L_z S_z . \tag{A-III.3}$$

The third term is the centrifugal distortion term of the spin-rotation interaction,

$$\mathbf{H}_{socd} = \frac{1}{2} A_D \left\{ \left(\mathbf{J} - \mathbf{L} - \mathbf{S}\right)^2 L_z S_z + L_z S_z \left(\mathbf{J} - \mathbf{L} - \mathbf{S}\right)^2 \right\} . \tag{A-III.4}$$

The fourth term is the spin-rotation interaction term,

$$\mathbf{H}_{sr} = \gamma \left(\mathbf{J} - \mathbf{S}\right) \cdot \mathbf{S} . \tag{A-III.5}$$

The last term $\mathbf{H}_{\Lambda}$ indicates the Λ-type doubling. The Λ-type doubling is due to a mixing of electronic states between a $^2\Pi$ state considered and a low-lying $^2\Sigma$ state through the spin-orbit and rotational electronic Coriolis interactions, and its term is explicitly written by

$$\mathbf{H}_{\Lambda} = -\frac{1}{2} q \left(J_+^{\ 2} e^{-2i\phi} + J_-^{\ 2} e^{2i\phi}\right) + \frac{1}{2}\left(p + 2q\right)\left(J_+ S_+ e^{-2i\phi} + J_- S_- e^{2i\phi}\right) , \tag{A-III.6}$$

where p and q are Λ-doubling constants. Matrix elements of the effective Hamiltonian $\mathbf{H}$ for a $^2\Pi$ electronic state are given by

$$\begin{aligned}\left\langle {}^2\Pi_{1/2}, J, \pm \middle| \mathbf{H} \middle| {}^2\Pi_{1/2}, J, \pm \right\rangle = &-\frac{A_{so}}{2} + D + \left(B - A_D/2 - D\right)\left(J + 1/2\right)^2 \\ &- D\left(J + 1/2\right)^4 \mp \left(-1\right)^{J-1/2}\left(q + p/2\right)\left(J + 1/2\right) , \end{aligned} \tag{A-III.7}$$

$$\begin{aligned}\left\langle {}^2\Pi_{3/2}, J, \pm \middle| \mathbf{H} \middle| {}^2\Pi_{3/2}, J, \pm \right\rangle = &\frac{A_{so}}{2} - 3D + \left(B + A_D/2 + 3D\right)\left\{\left(J + 1/2\right)^2 - 2\right\} \\ &- D\left(J + 1/2\right)^4 , \end{aligned} \tag{A-III.8}$$

$$\left\langle {}^2\Pi_{3/2}, J, \pm \middle| \mathbf{H} \middle| {}^2\Pi_{1/2}, J, \pm \right\rangle = -\left[B - \gamma/2 - 2D\left\{\left(J + 1/2\right)^2 - 1\right\}\right.$$

$$\mp(-1)^{J-1/2}(q/2)(J+1/2)\big]\left\{(J+1/2)^2-1\right\}^{1/2}. \tag{A-III.9}$$

Eq. (A-III.8) shows that the diagonal value of the Λ-doubling terms is zero in the Ω = 3/2 spin sub-levels, meaning that the Λ-type splittings in the Ω = 3/2 sub-levels are much smaller than those in the Ω = 1/2 sub-levels.

Hyperfine interactions are represented by the following Hamiltonian,

$$\mathbf{H}_{hfs}=b_F\mathbf{T}^1(\mathbf{S})\mathbf{T}^1(\mathbf{I})-\sqrt{10}\,g_S g_N\mu_B\mu_N\mathbf{T}^1(\mathbf{I})\mathbf{T}^1\left(\mathbf{S},C^2\right)+\mathbf{T}^2(\mathbf{Q})\cdot\mathbf{T}^2(\nabla\mathbf{E}), \tag{A-III.10}$$

where the first term is the Fermi contact interaction term, the second term is the magnetic dipole-dipole interaction term, and the third term is the electric quadrupole interaction term. In Eq. (A-III.10), b_F is the Fermi contact constant defined as

$$b_F=\frac{8\pi}{3}g_S g_N\mu_B\mu_N\left|\psi_{1s}(0)\right|^2, \tag{A-III.11}$$

and

$$\mathbf{T}^1(\mathbf{I})\mathbf{T}^1\left(\mathbf{S},C^2\right)=-\sum_{p,q}\sqrt{3}\begin{pmatrix}1 & 1 & 2\\ p & q-p & -q\end{pmatrix}T_p^{\ 1}(\mathbf{I})T_{q-p}^{\ 1}(\mathbf{S})C_{-q}^2(\theta,\phi)r^{-3}, \tag{A-III.12}$$

$$\mathbf{T}^2(\mathbf{Q})=\sum_n e_n r_n^2 C^2(\theta_n,\phi_n), \tag{A-III.13}$$

$$\mathbf{T}^2(\nabla\mathbf{E})=-\sum_i e_i C^2(\theta_n,\phi_n)r_i^{-3}. \tag{A-III.14}$$

The function $C_q^2(\theta,\phi)$ is related to the second-rank spherical harmonics as

$$C_q^2(\theta,\phi)=\sqrt{\tfrac{4\pi}{5}}Y_{2q}(\theta,\phi). \tag{A-III.15}$$

Matrix elements of $\mathbf{H}_{hfs}$ for a $^2\Pi$ electronic state are given by

$$\left\langle {}^2\Pi_\Omega;I\,J'\,F;\pm\left|\mathbf{H}_{hfs}\right|{}^2\Pi_\Omega;I\,J\,F;\pm\right\rangle=G(J'JIF)(-1)^{J'-\Omega}\begin{pmatrix}J' & 1 & J\\ -\Omega & 0 & \Omega\end{pmatrix}\{a\Lambda+(b+c)\Sigma\}$$

$$+Q(J'JIF)(-1)^{J'-\Omega}\begin{pmatrix}J' & 2 & J\\ -\Omega & 0 & \Omega\end{pmatrix}eQq_0/4, \tag{A-III.16}$$

$$\left\langle {}^2\Pi_{3/2};I\,J'\,F;\pm\left|\mathbf{H}_{hfs}\right|{}^2\Pi_{1/2};I\,J\,F;\pm\right\rangle=-G(J'JIF)(-1)^{J'-3/2}\begin{pmatrix}J' & 1 & J\\ -3/2 & 1 & 1/2\end{pmatrix}$$

$$\times b/\sqrt{2}, \tag{A-III.17}$$

$$\left\langle {}^2\Pi_{1/2}; I\,J'\,F;\,\pm \left| \mathbf{H}_{hfs} \right| {}^2\Pi_{1/2}; I\,J\,F;\,\pm \right\rangle = \pm G(J'\,J\,I\,F) \begin{pmatrix} J' & 1 & J \\ 1/2 & -1 & 1/2 \end{pmatrix} d/\sqrt{2}\,, \qquad \text{(A-III.18)}$$

$$\left\langle {}^2\Pi_{3/2}; I\,J'\,F;\,\pm \left| \mathbf{H}_{hfs} \right| {}^2\Pi_{1/2}; I\,J\,F;\,\pm \right\rangle = \mp Q(J'\,J\,I\,F) \begin{pmatrix} J' & 2 & J \\ 3/2 & -2 & 1/2 \end{pmatrix} eQq_2/4\sqrt{6}\,. \qquad \text{(A-III.19)}$$

In Eqs. (A-III.16) to (A-III.19), $G(J'\,J\,I\,F)$ and $Q(J'\,J\,I\,F)$ are

$$G(J'\,J\,I\,F) = \{I(I+1)(2I+1)(2J'+1)(2J+1)\}^{1/2} (-1)^{J'+I+F} \begin{Bmatrix} I & J' & F \\ J & I & 1 \end{Bmatrix}, \qquad \text{(A-III.20)}$$

and

$$Q(J'\,J\,I\,F) = \{(I+1)(2I+1)(2I+3)(2J'+1)(2J+1)/(2I-1)\}^{1/2}$$

$$\times (-1)^{J'+I+F} \begin{Bmatrix} I & J' & F \\ J & I & 2 \end{Bmatrix}. \qquad \text{(A-III.21)}$$

The matrix elements given by Eqs. (A-III.18) and (A-III.19) describe the parity-dependences of the magnetic hyperfine interaction and the electric quadrupole interaction, respectively. The constants *a*, *b*, *c*, and *d* are the magnetic hyperfine constants, which are first introduced by Frosch and Foley, defined as

$$a = 2g_N \mu_B \mu_N \left\langle \Lambda = 1 \left| r^{-3} \right| \Lambda = 1 \right\rangle, \qquad \text{(A-III.22)}$$

$$b = b_F - c/3\,, \qquad \text{(A-III.23)}$$

$$c = (3/2)\, g_S g_N \mu_B \mu_N \left\langle \frac{3\cos^2\theta - 1}{r^3} \right\rangle$$

$$= 3 g_S g_N \mu_B \mu_N \left\langle \Lambda = 1 \left| C_0^2(\theta, \phi) r^{-3} \right| \Lambda = 1 \right\rangle, \qquad \text{(A-III.24)}$$

$$d = (3/2)\, g_S g_N \mu_B \mu_N \left\langle \frac{\sin^2\theta}{r^3} \right\rangle$$

$$= -\sqrt{6} g_S g_N \mu_B \mu_N \left\langle \Lambda = 1 \left| C_2^2(\theta, \phi) r^{-3} \right| \Lambda = 1 \right\rangle. \qquad \text{(A-III.25)}$$

The Frosch and Foley hyperfine constants are related to the dipole-dipole interaction constants as

$$b = b_F - (1/2) T_{aa}\,, \qquad \text{(A-III.26)}$$

$$c = (1/2) T_{aa}\,, \qquad \text{(A-III.27)}$$

$$d = T_{bb} - T_{cc}\,. \qquad \text{(A-III.28)}$$

To derive Eqs. (A-III.26) to (A-III.28), the following relations were used:

$$g_S g_N \mu_B \mu_N \left\langle \Lambda = 1 \middle| C_0^2(\theta, \phi) r^{-3} \middle| \Lambda = 1 \right\rangle = T_{aa}/2 \,. \tag{A-III.29}$$

$$g_S g_N \mu_B \mu_N \left\langle \Lambda = 1 \middle| C_2^2(\theta, \phi) r^{-3} \middle| \Lambda = 1 \right\rangle = \left(1/\sqrt{6}\right)(T_{bb} - T_{cc}) \,. \tag{A-III.30}$$

The constants eQq_0 and eQq_2 are the quadrupole coupling constants, and these two constants are written in the Cartesian coordinate system as,

$$eQq_0 = \frac{\chi_{zz}}{2} \tag{A-III.31}$$

$$eQq_2 = \frac{\left(\chi_{xx} - \chi_{yy} \pm 2i\chi_{xy}\right)}{\sqrt{24}} \,. \tag{A-III.32}$$

In GAUSSIAN, the magnetic dipole-dipole interaction and the quadrupole coupling tensors are calculated in the Cartesian tensor forms.

Appendix IV
Predicted Transition Frequencies of SiC_2N and SiC_3N in the mm-Wave Region

Table A-IV.1. Predicted transition frequencies of SiC_2N ($\tilde{X}\ ^2\Pi_{3/2}$).[a]

J'	J''	(MHz)	J'	J''	(MHz)
13.5	12.5	71176.61	28.5	27.5	150245.71
14.5	13.5	76448.61	29.5	28.5	155515.94
15.5	14.5	81720.53	30.5	29.5	160786.01
16.5	15.5	86992.36	31.5	30.5	166055.92
17.5	16.5	92264.10	42.5	41.5	224012.36
18.5	17.5	97535.74	43.5	42.5	229279.85
19.5	18.5	102807.29	44.5	43.5	234547.10
20.5	19.5	108078.72	45.5	44.5	239814.11
21.5	20.5	113350.04	46.5	45.5	245080.87
22.5	21.5	118621.25	47.5	46.5	250347.38
23.5	22.5	123892.33	48.5	47.5	255613.63
24.5	23.5	129163.28	49.5	48.5	260879.62
25.5	24.5	134434.10	50.5	49.5	266145.34
26.5	25.5	139704.78			
27.5	26.5	144975.32			

[a]Λ-doublings were unresolved.

Table A-IV.2. Predicted transition frequencies of SiC_3N ($\tilde{X}\ ^2\Pi_{1/2}$).[a]

J'	J''	Parity	(MHz)	J'	J''	Parity	(MHz)
25.5	24.5	*e*	72114.88	38.5	37.5	*e*	108874.12
		f	72123.20			*f*	108882.22
26.5	25.5	*e*	74942.77	39.5	38.5	*e*	111701.41
		f	74951.07			*f*	111709.49
27.5	26.5	*e*	77770.62	40.5	39.5	*e*	114528.66
		f	77778.90			*f*	114536.72
28.5	27.5	*e*	80598.43	41.5	40.5	*e*	117355.84
		f	80606.70			*f*	117363.88
29.5	28.5	*e*	83426.20	42.5	41.5	*e*	120182.97
		f	83434.45			*f*	120190.99
30.5	29.5	*e*	86253.92	43.5	42.5	*e*	123010.04
		f	86262.17			*f*	123018.04
31.5	30.5	*e*	89081.61	44.5	43.5	*e*	125837.05
		f	89089.83			*f*	125845.03
32.5	31.5	*e*	91909.25	45.5	44.5	*e*	128664.00
		f	91917.46			*f*	128671.95
33.5	32.5	*e*	94736.85	46.5	45.5	*e*	131490.88
		f	94745.04			*f*	131498.81
34.5	33.5	*e*	97564.40	47.5	46.5	*e*	134317.70
		f	97572.58			*f*	134325.61
35.5	34.5	*e*	100391.91	48.5	47.5	*e*	137144.46
		f	100400.06			*f*	137152.34
36.5	35.5	*e*	103219.36	49.5	48.5	*e*	139971.14
		f	103227.50			*f*	139979.00
37.5	36.5	*e*	106046.76	50.5	49.5	*e*	142797.76
		f	106054.88			*f*	142805.59

(*Continued.*)

J'	J''	Parity	(MHz)	J'	J''	Parity	(MHz)
51.5	50.5	*e*	145624.31	83.5	82.5	*e*	236028.41
		f	145632.12			*f*	236035.14
52.5	51.5	*e*	148450.78	84.5	83.5	*e*	238851.86
		f	148458.57			*f*	238858.55
53.5	52.5	*e*	151277.19	85.5	84.5	*e*	241675.19
		f	151284.94			*f*	241681.84
54.5	53.5	*e*	154103.52	86.5	85.5	*e*	244498.40
		f	154111.24			*f*	244505.01
55.5	54.5	*e*	156929.77	87.5	86.5	*e*	247321.49
		f	156937.47			*f*	247328.05
56.5	55.5	*e*	159755.94	88.5	87.5	*e*	250144.46
		f	159763.62			*f*	250150.98
57.5	56.5	*e*	162582.04	89.5	88.5	*e*	252967.30
		f	162589.69			*f*	252973.78
58.5	57.5	*e*	165408.06	90.5	89.5	*e*	255790.02
		f	165415.67			*f*	255796.46
59.5	58.5	*e*	168233.99	91.5	90.5	*e*	258612.62
		f	168241.58			*f*	258619.01
79.5	78.5	*e*	224733.47	92.5	91.5	*e*	261435.09
		f	224740.36			*f*	261441.43
80.5	79.5	*e*	227557.37	93.5	92.5	*e*	264257.43
		f	227564.23			*f*	264263.72
81.5	80.5	*e*	230381.16	94.5	93.5	*e*	267079.63
		f	230387.98			*f*	267085.89
82.5	81.5	*e*	233204.84	83.5	82.5	*e*	236028.41
		f	233211.62			*f*	236035.14

[a]Hyperfine structure has not been included since the splittings are less than 10 kHz.

Appendix V
Observed Line Positions of Bands [A], [D], and [E] of the SiC_3H $\tilde{A}^2\Sigma^+ - \tilde{X}^2\Pi_i$ Band System

Table A-V.1. Observed line positions of band [A] (in cm^{-1}).

J''	Obs.	Obs. − Calc.	J''	Obs.	Obs. − Calc.
$P_1(J'')$			$R_{21}(J'')$		
3.5	14775.715	0.001	3.5	14777.883	0.004
4.5	14775.470	−0.001	4.5	14778.178	0.001
5.5	14775.232	−0.002	5.5	14778.478	−0.003
6.5	14775.001	−0.002	6.5	14778.793	0.003
7.5	14774.774	−0.004	7.5	14779.108	0.002
8.5	14774.557	−0.002	8.5	14779.435	0.006
9.5	14774.343	−0.002	9.5	14779.757	0.001
10.5	14774.133	−0.005	10.5	14780.089	−0.001
11.5	14773.940	0.003	11.5	14780.433	0.003
12.5	14773.740	−0.002	12.5	14780.779	0.003
13.5	14773.548	−0.005	13.5	14781.136	0.007
14.5	14773.363	−0.008	14.5	14781.484	−0.003
15.5	14773.193	0.000	15.5	14781.847	−0.004
16.5	14773.018	−0.004	16.5	14782.217	−0.004
17.5	14772.850	−0.008	17.5	14782.595	−0.003
18.5	14772.706	0.006	18.5	14782.983	0.003
19.5	14772.545	−0.002	19.5	14783.361	−0.008
20.5	14772.396	−0.005	20.5	14783.780	0.016
21.5	⋯	⋯	21.5	14784.153	−0.011
$Q_{21}(J'')$[a]			$R_1(J'')$[a]		

(*Continued.*)

J''	Obs.	Obs. − Calc.	J''	Obs.	Obs. − Calc.
1.5	14776.764	0.002	1.5	14776.764	0.008
2.5	14776.866	−0.002	2.5	14776.866	0.006
3.5	14776.975	−0.005	3.5	14776.975	0.005
4.5	14777.094	−0.004	4.5	14777.094	0.009
5.5	14777.223	0.001	5.5	14777.223	0.016
6.5	14777.347	−0.006	6.5	14777.347	0.011
7.5	14777.486	−0.002	7.5	14777.486	0.017
8.5	14777.626	−0.005	8.5	14777.626	0.016
9.5	14777.779	0.000	9.5	14777.779	0.024
10.5	14777.936	0.002	10.5	14777.936	0.028
11.5	14778.093	−0.002	11.5	14778.093	0.027
12.5	14778.261	0.000	12.5	14778.261	0.031
13.5	14778.429	−0.004	13.5	14778.429	0.029
14.5	14778.605	−0.007	14.5	14778.605	0.029
15.5	14778.793	−0.003	15.5	14778.793	0.035
16.5	14778.982	−0.006	16.5	14778.982	0.034
17.5	14779.179	−0.006	17.5	14779.179	0.037
18.5	14779.386	−0.002	18.5	14779.386	0.043
19.5	14779.595	−0.001	19.5	14779.595	0.046
20.5	14779.805	−0.007	20.5	14779.805	0.043
21.5	14780.023	−0.009	21.5	14780.023	0.042

[a]Splittings between Q_{21} and R_1 branches were not resolved. Weights of 0.25 were given for all the unresolved lines of the two branches in the least-square fitting.

Table A-V.2. Observed line positions of band [D] (in cm^{-1}).

J''	Obs.	Obs. − Calc.	J''	Obs.	Obs. − Calc.
$P_1(J'')$			$R_{21}(J'')$		
3.5	15446.632	0.000	3.5	15448.789	0.006
4.5	15446.391	0.000	4.5	15449.080	−0.001
5.5	15446.162	0.005	5.5	15449.345	−0.038
6.5	15445.927	0.000	6.5	15449.703	0.011
7.5	15445.706	0.001	7.5	15450.015	0.007
8.5	15445.494	0.005	8.5	15450.322	−0.007
9.5	15445.275	−0.004	9.5	15450.655	−0.001
10.5	15445.079	0.005	10.5	15450.991	0.001
11.5	15444.879	0.002	11.5	15451.338	0.008
12.5	15444.689	0.004	12.5	15451.679	0.002
13.5	15444.504	0.004	13.5	15452.028	−0.001
14.5	15444.307	−0.013	14.5	15452.386	−0.001
15.5	15444.157	0.009	15.5	15452.743	−0.010
16.5	15443.986	0.005	16.5	15453.127	0.003
17.5	15443.819	−0.001	17.5	⋯	⋯
18.5	15443.663	−0.004	18.5	⋯	⋯
19.5	15443.518	0.000	19.5	⋯	⋯
$Q_{21}(J'')$[a]			$R_1(J'')$[a]		
1.5	15447.676	0.006	1.5	15447.676	0.003
2.5	15447.775	0.001	2.5	15447.775	−0.004
3.5	15447.904	0.019	3.5	15447.904	0.012
4.5	15448.003	0.000	4.5	15448.003	−0.008
5.5	15448.130	0.004	5.5	15448.130	−0.005
6.5	15448.262	0.007	6.5	15448.262	−0.004

(*Continued.*)

J''	Obs.	Obs. − Calc.	J''	Obs.	Obs. − Calc.
7.5	15448.397	0.007	7.5	15448.397	−0.005
8.5	15448.551	0.019	8.5	15448.551	0.005
9.5	15448.693	0.013	9.5	15448.693	−0.002
10.5	15448.844	0.010	10.5	15448.844	−0.006
11.5	15449.002	0.007	11.5	15449.002	−0.011
12.5	15449.174	0.013	12.5	15449.174	−0.007
13.5	15449.345	0.012	13.5	15449.345	−0.009
14.5	15449.515	0.002	14.5	15449.515	−0.020
15.5	15449.703	0.005	15.5	15449.703	−0.019
16.5	15449.889	0.001	16.5	15449.889	−0.025
17.5	15450.101	0.014	17.5	15450.101	−0.012
18.5	15450.322	0.032	18.5	15450.322	0.004
19.5	15450.511	0.011	19.5	15450.511	−0.019
20.5	15450.741	0.025	20.5	15450.741	−0.006

[a]Splittings between Q_{21} and R_1 branches were not resolved. Weights of 0.25 were given for all the unresolved lines of the two branches in the least-square fitting.

Table A-V.3. Observed line positions of band [E] (in cm^{-1}).

J''	Obs.	Obs. − Calc.	J''	Obs.	Obs. − Calc.
$P_1(J'')$			$R_{21}(J'')$		
2.5	⋯	⋯	2.5	15457.842	0.009
3.5	15455.969	−0.002	3.5	15458.125	0.000
4.5	15455.723	−0.007	4.5	15458.428	0.006
5.5	15455.506	0.010	5.5	15458.732	0.005
6.5	15455.267	0.000	6.5	15459.049	0.012
7.5	15455.041	−0.005	7.5	15459.349	−0.005
8.5	15454.829	−0.001	8.5	15459.673	−0.004
9.5	15454.613	−0.008	9.5	15460.005	0.000
10.5	15454.415	−0.002	10.5	15460.333	−0.008
11.5	15454.224	0.002	11.5	15460.681	−0.002
12.5	15454.028	−0.004	12.5	15461.033	0.002
13.5	15453.846	−0.001	13.5	15461.380	−0.005
14.5	15453.666	−0.004	14.5	15461.742	−0.004
15.5	15453.501	0.003	15.5	15462.114	0.001
16.5	15453.335	0.002	16.5	15462.482	−0.006
17.5	15453.177	0.003	17.5	15462.861	−0.006
18.5	15453.027	0.005	18.5	15463.253	−0.001
19.5	15452.864	−0.012	19.5	15463.659	0.014
20.5	15452.756	0.019	20.5	15464.040	−0.005
$Q_{21}(J'')$[a]			$R_1(J'')$[a]		
1.5	15457.020	0.011	1.5	15457.020	0.008
2.5	15457.113	−0.002	2.5	15457.113	−0.006
3.5	15457.231	0.005	3.5	15457.231	−0.001
4.5	15457.347	0.004	4.5	15457.347	−0.003

(*Continued.*)

J''	Obs.	Obs. − Calc.	J''	Obs.	Obs. − Calc.
5.5	15457.473	0.005	5.5	15457.473	−0.003
6.5	15457.601	0.003	6.5	15457.601	−0.006
7.5	15457.742	0.007	7.5	15457.742	−0.002
8.5	15457.886	0.008	8.5	15457.886	−0.003
9.5	15458.035	0.008	9.5	15458.035	−0.004
10.5	15458.194	0.011	10.5	15458.194	−0.002
11.5	15458.358	0.013	11.5	15458.358	−0.002
12.5	15458.519	0.006	12.5	15458.519	−0.010
13.5	15458.698	0.010	13.5	15458.698	−0.007
14.5	15458.882	0.013	14.5	15458.882	−0.005
15.5	15459.049	−0.008	15.5	15459.049	−0.027
16.5	15459.232	−0.018	16.5	15459.232	−0.038
17.5	15459.447	−0.003	17.5	15459.447	−0.024
18.5	15459.673	0.017	18.5	15459.673	−0.006
19.5	15459.881	0.012	19.5	15459.881	−0.012
20.5	15460.096	0.008	20.5	15460.096	−0.017
21.5	15460.333	0.020	21.5	15460.333	−0.006

[a]Splittings between Q_{21} and R_1 branches were not resolved. Weights of 0.25 were given for all the unresolved lines of the two branches in the least-square fitting.